

超级神冈-IV中超新星遗迹 中微子的实验研究

(申请清华大学理学博士学位论文)

培 养 单 位 : 工 程 物 理 系

学 科 : 物 理 学

研 究 生 : 张 洋

指 导 教 师 : 陈 少 敏 教 授

二〇一五年四月

**Experimental Studies of Supernova
Relic Neutrinos at
Super-Kamiokande-IV**

Dissertation Submitted to
Tsinghua University
in partial fulfillment of the requirement
for the degree of
Doctor of Philosophy
in
Physics

by
ZHANG Yang

Dissertation Supervisor : Professor Chen Shaomin

April, 2015

关于学位论文使用授权的说明

本人完全了解清华大学有关保留、使用学位论文的规定，即：

清华大学拥有在著作权法规定范围内学位论文的使用权，其中包括：（1）已获学位的研究生必须按学校规定提交学位论文，学校可以采用影印、缩印或其他复制手段保存研究生上交的学位论文；

（2）为教学和科研目的，学校可以将公开的学位论文作为资料在图书馆、资料室等场所供校内师生阅读，或在校园网上供校内师生浏览部分内容；（3）根据《中华人民共和国学位条例暂行实施办法》，向国家图书馆报送可以公开的学位论文。

本人保证遵守上述规定。

（保密的论文在解密后应遵守此规定）

作者签名： _____

导师签名： _____

日 期： _____

日 期： _____

摘要

超新星遗迹中微子是指在宇宙演化历史中, 过往核坍缩型超新星爆发过程中产生并遗留下来的各种类型中微子。但是, 至今为止超新星遗迹中微子尚未在实验中观测到。基于宇宙中的超新星爆发率、超新星爆发发射的中微子能谱以及红移效应, 有许多理论模型预言了这些超新星遗迹中微子的流强。因此, 寻找超新星遗迹中微子并测量其流强大小, 对研究宇宙的演化、星球的形成、超新星的爆发机制以及相关中微子物理等研究具有重要的科学意义。

本论文在日本超级神冈中微子实验中, 利用5万吨大型水质契伦科夫探测器开展了超新星遗迹中微子的实验研究, 主要工作如下:

1) 研究了超新星遗迹中微子中的反电子中微子和水发生反贝塔衰变所产生的瞬时正电子与延时中子的信号特征。根据优化信噪比(s/\sqrt{b})的原理, 改进了宇宙线散裂本底的事例选择条件, 使其适用于电子能量在8 MeV左右的低能区。并且对信号事例产生的关联中子的氢俘获标记技术进行了改进, 利用多变量分析方法将信噪比提高了两倍, 使得信号的寻找范围覆盖了整个超新星遗迹中微子“黄金能量窗口”。

2) 研究了影响超新星遗迹中微子探测的主要本底来源-宇宙线散裂本底, 并根据寿命测量了放射性同位素硼-12、氮-12、锂-9、氦-8/碳-9、锂-8/硼-8、氮-16、铍-11以及碳-15的产额。进一步地, 利用中子标记技术选择 βn 事例, 将锂-9事例的产额改进为 $(0.56 \pm 0.07 \pm 0.13) \mu^{-1}g^{-1}cm^2$ 。这些测量结果与理论模型预言的比较可以更好地理解高能宇宙线与水的相互作用机制, 并且对在未来大型水质契伦科夫探测器中开展超新星遗迹中微子寻找的预先研究具有重要的价值。

3) 利用2008年到2014年的数据, 首次在9.3 - 31.3 MeV的中微子黄金能量窗口寻找超新星遗迹中微子, 观测到了18个事例。该数目与预言的 (18.0 ± 3.0) 个本底事例数目相符, 没有发现超新星遗迹中微子信号。因此, 计算了超新星遗迹中微子的微分流强上限。同时, 给出了90%置信水平下的积分流强上限的区间为 $25-31 cm^{-2}s^{-1}$ 。该上限接近常数超新星爆发率模型的预言。

关键词: 超新星遗迹中微子; 水质契伦科夫探测器; 中子标记; 宇宙线散裂本底; 流强上限

Abstract

Supernova relic neutrinos are six types of neutrinos from all past core-collapse supernovae since the beginning of the universe. However, supernova relic neutrinos have never been observed yet. Based on supernova rates in the universe, neutrino emission from supernova bursts and the red shift effect, many models have predicted both the spectrum and flux of supernova relic neutrinos. Therefore, the detection of supernova relic neutrinos is of crucial importance for studying the evolution of the universe, the formation of stars, the mechanism of supernova bursts and the related neutrino physics.

This thesis provides experimental studies of supernova relic neutrinos using 50 ktons of pure water in the Super-Kamiokande-IV detector. The studies are as follows:

1) We study the signature of both a prompt positron and a delayed neutron event produced by the inverse-beta-decay reaction ($\bar{\nu}_e + p \rightarrow e^+ + n$). The reduction of spallation background is better tuned with the optimization of signal-to-noise ratio (s/\sqrt{b}) and can be applied to the energy region down to about 8 MeV. By using the Multivariate Analysis method, the neutron tagging technique is improved with an enhancement of the signal-to-noise ratio by a factor of about 2, which provides a sensitivity over the whole golden energy window for the search of supernova relic neutrinos.

2) We study the cosmic-ray muon spallation induced radioactive isotopes, which is the dominant background for search of the supernova relic neutrinos. The yields of the major radioactive isotopes, ^{12}B , ^{12}N , ^9Li , $^8\text{He}/^9\text{C}$, $^8\text{Li}/^8\text{B}$, ^{16}N , ^{11}Be and ^{15}C , are first measured from the distribution of time after a muon. We further improve the measurement on the ^9Li yield to be $(0.56 \pm 0.07 \pm 0.13) \mu^{-1} \text{g}^{-1} \text{cm}^2$ by using a 500 μs forced trigger data. The measurement can help to understand the mechanism of the interaction between energetic cosmic-ray muons and water, which will be important in designing water Cherenkov detectors for search of supernova relic neutrinos in future.

3) We search supernova relic neutrinos within the golden energy window between 9.3 and 31.3 MeV with the data collected from 2008 to 2014. The number of 18 observed candidates is consistent with that of (18.0 ± 3.0) expected background events. No signal is found. Therefore, upper limits on the differential flux are calculated, together with those on the integral flux, which are 25-31 $\text{cm}^{-2} \text{s}^{-1}$ at 90% C.L.. These limits are approaching

to the flux predicted by the constant supernova rate model.

Key words: Supernova Relic Neutrinos; Water Cherenkov Detector; Neutron Tagging;
Cosmic Ray Induced Spallation Background; Upper Limit of Flux

Contents

Chapter 1 Introduction	1
1.1 Neutrinos	1
1.2 Supernova Burst Neutrinos	1
1.3 Supernova Relic Neutrinos	3
1.4 Background Sources for SRN Search at SK	5
1.5 The Present SRN Search Status	7
1.5.1 Search at KamLAND	8
1.5.2 Search at SK-I/II/III	9
1.5.3 Search at SK-IV	10
Chapter 2 The Super-Kamiokande Detector	12
2.1 Detector Overview	12
2.2 Detection Principle	13
2.3 Photomultiplier Tubes	14
2.4 Water Systems	15
2.5 Radon Free Air Systems	16
2.6 Front-end Electronics and Data Acquisition System	17
Chapter 3 Detector Calibration	19
3.1 Energy Calibration	19
3.1.1 LINAC Calibration	19
3.1.2 DT Calibration	19
3.1.3 Decay Electrons	21
3.2 PMT Calibration	22
3.2.1 PMT Gain	22
3.2.2 Time Walk Effect	23
3.3 Water Transparency Measurement	24
3.3.1 Laser Measurement	24
3.3.2 Decay Electrons	24
Chapter 4 Event Reconstruction	27
4.1 Vertex Reconstruction	27
4.2 Energy Reconstruction	27
4.3 Direction Reconstruction	28
4.4 Muon Reconstruction	29

Contents

4.4.1	Muboy Fitter	29
4.4.2	Brute Force Fitter	30
4.4.3	Energy Loss	30
4.5	Cherenkov Angle Reconstruction	30
Chapter 5	Event Simulation	31
5.1	Simulation Package	31
5.2	Spallation Products	31
5.2.1	^{12}B Decay	31
5.2.2	^{12}N Decay	33
5.2.3	^{16}N Decay	33
5.2.4	^{11}Be Decay	33
5.2.5	^9Li Decay	35
5.2.6	^8He Decay	35
5.2.7	^9C Decay	38
5.2.8	^8Li Decay	40
5.2.9	^{15}C Decay	40
5.3	SRN	42
5.4	Atmospheric Neutrino Background	42
Chapter 6	Neutron Tagging	44
6.1	Discriminating Variables for 2.2 MeV γ Events	44
6.1.1	N_{10}	45
6.1.2	$N_{cluster}$	46
6.1.3	N_{back}	46
6.1.4	N_{low}	46
6.1.5	N_{300}	48
6.1.6	T_{rms}	49
6.1.7	ϕ_{rms}	49
6.1.8	$\theta_{mean}, \theta_{rms}$	49
6.1.9	$N_{LowTheta}$	51
6.1.10	Q_{mean}, Q_{rms}	52
6.1.11	N_{highQ}	52
6.2	TMVA Output	52
6.3	Determination of Efficiency	54
6.3.1	Efficiency for the SRN Search $E_{\bar{\nu}_e} < 14.3$ MeV	54
6.3.2	Efficiency for the SRN Search $E_{\bar{\nu}_e} > 14.3$ MeV	56
6.3.3	Comparison with the Previous Neutron Tagging	58

Contents

6.4	Study of Systematic Uncertainty on Neutron Tagging Efficiency	60
6.4.1	Experimental Setup	60
6.4.2	Test on the neutron tagging cut for $E_{\bar{\nu}_e} < 14.3$ MeV	61
6.4.3	Test on the neutron tagging cut for $E_{\bar{\nu}_e} > 14.3$ MeV	64
6.5	Application of the Neutron Tagging into Atmospheric Neutrino Data	67
6.6	Application of the Neutron Tagging to Solar Neutrino Events	68
6.7	Discussions of the Neutron Tagging Method	68
Chapter 7	Analysis of the Spallation Background	71
7.1	Measurement on Time Distribution	71
7.1.1	First Reduction	71
7.1.2	Transverse Distance Cut	74
7.1.3	Life Time Analysis	75
7.2	Further Study on ${}^9\text{Li}$ Yield with the Neutron Tagging Method	77
Chapter 8	Data Reduction for SRN Search	86
8.1	First Reduction	86
8.2	Spallation Cuts	86
8.2.1	Determination of Spallation background	87
8.3	Incoming Events Cut	90
8.4	Solar Events Cut	90
8.5	Cherenkov Angle Cut	91
8.6	Pre/post Activity Cut	91
8.7	Pion Cut	94
8.8	Multi-ring Cut	94
8.9	μ/π Cut	95
8.10	Neutron Tagging	95
8.11	Summary of Reduction Efficiency	96
Chapter 9	SRN Analysis and Results	97
9.1	The SRN Candidates	97
9.2	Background Estimation	97
9.2.1	Atmospheric $\bar{\nu}_\mu/\nu'_\mu$ s	97
9.2.2	Atmospheric $\bar{\nu}_e$'s	101
9.2.3	Neutral Current (NC) Events	101
9.2.4	Reactor Neutrinos	102
9.2.5	${}^9\text{Li}$ Events	102
9.2.6	Accidental Background	103
9.3	Systematics on Both the Efficiencies and the Background Estimations	105

Contents

9.4	Limit Extraction	106
9.4.1	The Upper Limit of the Differential Flux.....	106
9.4.2	The Upper Limit for the Integral Flux	110
Chapter 10	Summary and Outlook	115
10.1	Summary.....	115
10.2	Outlook	116
Reference	117
Acknowledgement	121
声 明	122
Resume and Publications	123

Chapter 1 Introduction

This chapter will review the general properties of neutrinos, the physics of supernova relic neutrinos (SRN), the background sources for SRN search at Super-Kamiokande (SK) and the present SRN search status.

1.1 Neutrinos

The neutrino was first proposed by Pauli for the requirement of energy and momentum conservation in β decays in 1930^[1]. It was not until 1956, 26 years after the idea proposed, $\bar{\nu}_e$'s from the reactor were first observed by Cowan and Reines through the inverse-beta-decay (IBD) reaction ($\bar{\nu}_e + p \rightarrow e^+ + p$)^[2]. The observation of neutrinos has motivated great interests in neutrino community since then.

In the standard model (SM) of particle physics, the neutrinos are fundamental particles with three flavors, ν_e , ν_μ and ν_τ , corresponding to their charged partners (e , μ , τ). The neutrinos cannot interact electro-magnetically since they are electrically neutral. Also, the neutrinos cannot undergo the strong force. Although the neutrinos could have tiny mass, which is beyond the SM, however, the gravitational force can be negligible compared with the weak force on matter. The only weak force involved in the neutrino interactions makes the detection of neutrinos very difficult since neutrinos can pass through matter as they don't exist.

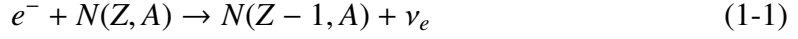
The known neutrino sources to date are from solar neutrinos, atmospheric neutrinos, man-made reactor/accelerator neutrinos, geo-neutrinos from the earth and neutrinos from SN1987A.

1.2 Supernova Burst Neutrinos

Core collapse supernovae are the massive stars with $M \gtrsim 8M_\odot$, ending their lives in explosion by emitting copious of all kinds of neutrinos. In the released $\sim 10^{53}$ ergs energy during the core collapse explosion, about 99% of which is carried by neutrino emission with the remain 1% released kinetically. Detailed information about the supernova burst and neutrino emission can be found in Ref.^[3-6]. The emission of neutrinos from a core

collapse supernova is outlined as follows:

1) At the beginning of collapse, the inner iron core is photodisintegrated. Electrons are captured on nuclei in the meantime.



The mean free path of emitted ν_e is longer than the radius of the core. Thus, these neutrinos can escape promptly from the core. The reduced degeneration pressure of electrons accelerates the gravitational collapse.

2) During the collapse, the core density increases, leading to a shorter mean free path of neutrinos. When the density of the inner core reaches $10^{11} - 10^{12} \text{ g/cm}^3$, neutrinos begin trapped by the coherent scattering off nuclei:



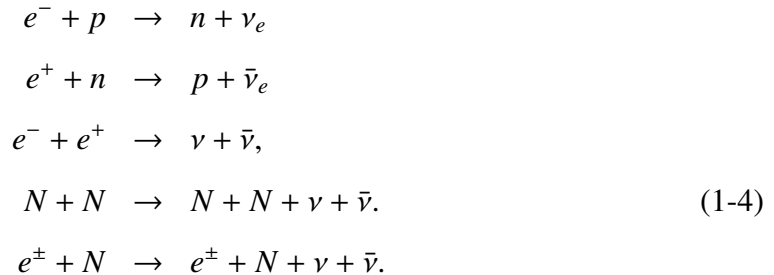
Only neutrinos from the outer sphere can escape freely. The sphere containing the trapped neutrinos is referred to as the neutrinosphere.

3) The inner core finishes the collapse when reaching the nuclear density $\sim 10^{14} \text{ g/cm}^3$. The neutron degeneration pressure encounters a gravitational pressure, inducing a rebound shock wave. The shock wave propagates through the matter of the outer core, dissociating the nuclei into free protons and neutrons with an energy loss of $\sim 8 \text{ MeV}$ per nucleus. The neutronization process occurs with a duration of $\sim 10 \text{ ms}$:



The ν_e 's generated through the neutronization process are released promptly with the release of the previously trapped ν_e 's. The peak luminosity is greater than 10^{53} erg/s . Due to the short duration of $\sim 10 \text{ ms}$, the released energy is only 10^{51} erg .

4) All flavours neutrinos are produced in the post-bounce region through the following reactions:



$$\begin{aligned}\gamma^* &\rightarrow \nu + \bar{\nu}. \\ \gamma^* + e^\pm &\rightarrow e^\pm + \nu + \bar{\nu}.\end{aligned}$$

where ν represents the neutrinos for all the flavors and $\bar{\nu}$ represents the counter anti-neutrinos, γ^* represents the plasmon.

5) The rebound shock wave loses energy through the nuclei dissociation and the neutrino emission, and thus comes to a stall. The shock wave could be recovered by a neutrino heating mechanism which deposits the energy of neutrinos. The explosion is delayed by a timescale of ~ 1 s. The duration of neutrino emission can last with an order of ~ 10 s. Eventually, the neutron star or black hole is left behind after the supernova explosion.

All flavours of neutrinos are believed to be emitted with approximately equal energy through the pair production. The neutrinos emitted closer to the core have larger energy. The ν_x only interact via the neutral current (NC) process. Therefore, the radius of ν_x neutrinosphere is smaller, resulting in a larger energy. The ν_e is easier to be trapped than the $\bar{\nu}_e$ since the protoneutron star is enriched in neutrons. The ranking of the average energy of neutrinos is as below:

$$\langle E_{\nu_e} \rangle < \langle E_{\bar{\nu}_e} \rangle < \langle E_{\nu_x} \rangle \quad (1-5)$$

The average energy for each flavour estimated in Ref.^[7,8] is:

$$\begin{aligned}\langle E_{\nu_e} \rangle &\simeq 13 \text{ MeV} \\ \langle E_{\bar{\nu}_e} \rangle &\simeq 16 \text{ MeV} \\ \langle E_{\nu_x} \rangle &\simeq 23 \text{ MeV}\end{aligned} \quad (1-6)$$

1.3 Supernova Relic Neutrinos

The SN1987A is the only core-collapse supernova explosion from which the neutrino events were recorded^[9,10]. The SN1987A occurred in the Large Magellanic Cloud, which is about 50 kpc away from the earth. Physical implications have been widely extracted from the observed 11 events in Kamiokande II^[9] and 8 events in IMB^[10]. Solid conclusions need more supernova neutrino events. However, a supernova explosion is quite rare in galaxy, $\lesssim 3$ per century^[11,12]. At the mean time of waiting for the next supernova explosion in galaxy, we can still study supernova physics by detecting

SRN. The cumulative neutrino fluxes from all past core-collapse supernova can form an observable signal in large water Cherenkov detectors^[13–17]. Observation of SRN could provide precious information on the evolution of the universe, the formation of stars, the mechanism of supernova bursts and the related neutrino physics.

SRN are six types of neutrinos from all past core-collapse supernovae since the beginning of the universe. SRN are also known as diffuse supernova neutrino background (DSNB)^[18]. The differential spectrum of SRN flux ($\frac{d\phi}{dE_\nu}(E_\nu)$) is calculated with the following formula^[18,19]:

$$\frac{d\phi}{dE_\nu}(E_\nu) = c \int_0^\infty R_{\text{SN}}(z)(1+z) \frac{d\phi[E_\nu(1+z)]}{dE_\nu} \left| \frac{dt}{dz} \right| dz, \quad (1-7)$$

where c is the speed of light, $R_{\text{SN}}(z)$ is the supernova rate, z is the red shift, $\frac{d\phi[E_\nu(1+z)]}{dE_\nu}$ is the neutrino emission from a supernova and $\frac{dz}{dt}$ is given below:

$$\frac{dz}{dt} = -H_0(1+z) \sqrt{(\Omega_m(1+z)^3 + \Omega_\Lambda)} \quad (1-8)$$

where H_0 , Ω_m and Ω_Λ are cosmological parameters. The predicted flux and the spectrum of SRN can be found in Ref.^[20–30]. Fig. 1.1 shows the effective cross section of neutrino interaction with water, in which the $\bar{\nu}_e$'s are detected via the IBD reaction within the energy region of interest and the event rate is two orders of magnitude larger than that of other channels^[21]. Therefore, we only focus on the study of $\bar{\nu}_e$'s. Fig. 1.2 shows the predicted $\bar{\nu}_e$ fluxes as a function of the neutrino energy for various models:

- Large mixing angle (LMA) model^[26] by Ando *et al.*, in which the neutrino oscillation with LMA solution inside the supernova was taken into account to calculate the spectrum of supernova neutrino emission.
- Constant SN rate model^[21] by Totani *et al.*'s, in which the supernova rate was assumed as a constant in the whole universe.
- Cosmic gas infall model^[23] by Malaney *et al.*, in which the supernova rate obtained from the density of cosmic gas as a function of red shift was used.
- Chemical evolution model^[24] by Hartmann *et al.*, in which the history of the cosmic star formation (the star formation rate is proportional to the supernova rate) obtained from the chemical evolution was used.
- Heavy metal model^[20,25] by Kaplinghat *et al.*, in which the abundance of the heavy elements are used to model the spectrum of supernova neutrino emission with a Fermi-Dirac distribution.

- Population synthesis model^[22] by Totani *et al.*, in which the realistic supernova rate obtained from the galaxy evolution using the population synthesis method was used.
- HBD 6 MeV neutrino temperature model^[27] by Horiuchi *et al.*, in which the neutrino spectrum with the effective temperature of 6 MeV was used.
- Star formation rate constraint model^[28] by Kawasaki *et al.*, in which the constraint on star formation rate based on SK's SRN search result^[31] was discussed.
- Failed SN model^[29] by Lunardini, in which hotter neutrino spectrum was used by taking into account of the direct formation of black hole during a supernova explosion.

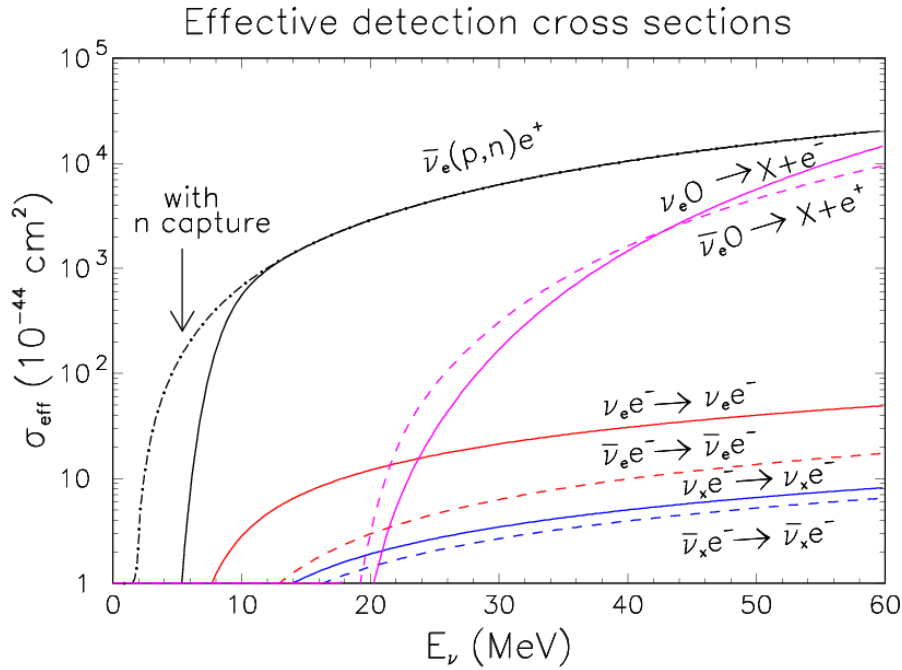


Figure 1.1 The cross sections of neutrino interactions with water at SK^[32].

1.4 Background Sources for SRN Search at SK

All the neutrino sources at SK site^[19] are shown in Fig. 1.3. At SK, perhaps the most favored energy window to search for the SRN is from 10 to 30 MeV^[33], which is also called as the golden energy window. The energy region below will suffer potential background from reactors and the energy region above will suffer background from atmospheric neutrinos. Above 10 MeV, the ⁸B solar neutrinos are ν_e 's only, and thus can be removed by both the solar angle cut and the identification of IBD events.

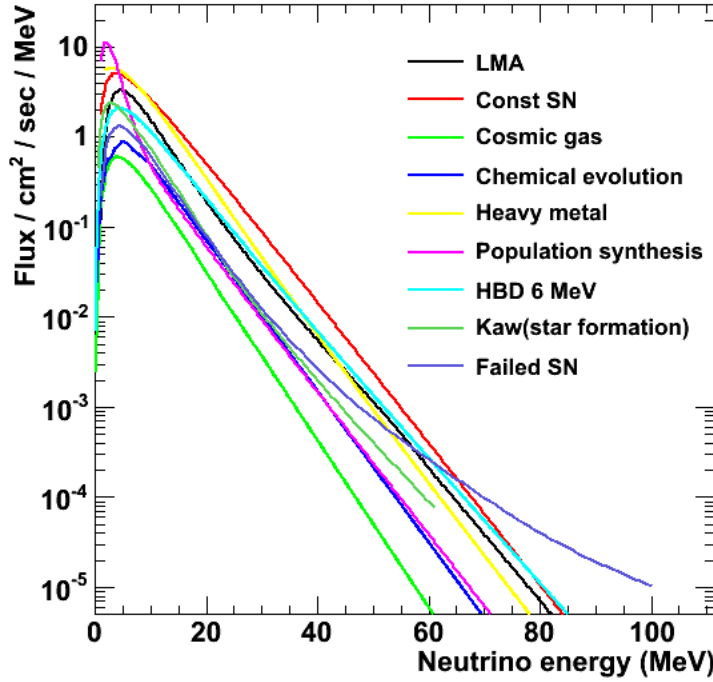


Figure 1.2 The predicted $\bar{\nu}_e$ fluxes as a function of the neutrino energy.

In the energy region of 10-30 MeV, the search for SRN is greatly affected by the cosmic-ray muon spallation induced radioactive isotopes since the muon rate is ~ 2 Hz. Fig. 1.4 shows the energy spectrum of the spallation background at SK, together with the predicted spectrum of SRN from LMA model. In the golden energy window of 10-30 MeV, the number of spallation background is $\sim 7 \times 10^4$ /year/22.5 kton, while the expected number of SRN events is ~ 5 events/year/22.5 kton from LMA model. Even though most of the spallation backgrounds can be removed by the spallation cuts at SK, the long-live radioactive isotopes could still survive. Most of the survival spallation background have no associated neutrons. For those with the βn decay mode, only ${}^9\text{Li}$ can have a significant contribution to the golden energy window through the beta energy tail. The branch ratio (BR) of βn modes from ${}^9\text{Li}$ decay is 50.8% and the mean life time of ${}^9\text{Li}$ is ~ 0.26 s. Recently, a theoretical calculation^[34] predicts the yield of ${}^9\text{Li}$ to be $1.9 \times 10^{-7} \mu^{-1} \text{g}^{-1} \text{cm}^2$. An experimental measurement of ${}^9\text{Li}$ yield can help to understand the the interaction between the energetic cosmic-ray muons and water, and is also of crucial importance for the purpose of SRN search in SK, the future GADZOOKS!^[33] and Hyper-K^[14] projects.

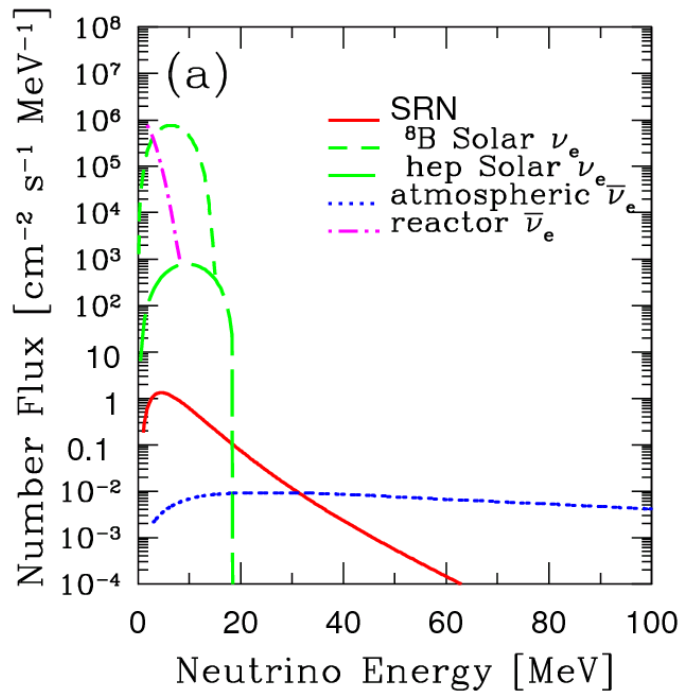


Figure 1.3 The expected neutrino sources at SK site^[19].

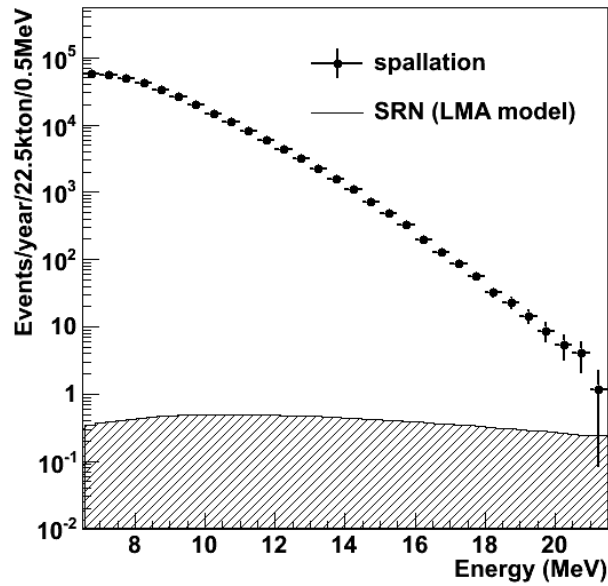


Figure 1.4 The number of spallation background as a function of electron energy. The expected SRN spectrum from LMA model is plotted in shadow.

1.5 The Present SRN Search Status

Even though there were many experimental efforts, SRN have never been observed yet. Fig. 1.5 shows the $\bar{\nu}_e$ flux upper limit at 90% C.L. from KamLAND^[35], SK-I/II/III^[36]

and SK-IV results^[13], respectively. The flux of SRN using the constant SN rate model is also plotted for a purpose of comparison, since it gives the largest flux among all the SRN models. The present experimental results cannot exclude any SRN models.

1.5.1 Search at KamLAND

KamLAND is an 1-kton liquid scintillator detector, served as a $\bar{\nu}_e$ detector. The high efficiency in detecting neutrons makes the detector more efficient to the IBD events. Fig. 1.6 shows the positron energy spectrum of the final $\bar{\nu}_e$ sample in KamLAND, which can be found in Ref.^[35]. The NC atmospheric neutrino background dominated the whole energy spectrum from 8.3 to 31.3 MeV, letting the observation of SRN signals very difficult. The search didn't find any obvious SRN signal, and thus set an upper limit of flux. It is noted that KamLAND gives the best upper limit of flux below 17.3 MeV due to both the large exposure and the efficient $\bar{\nu}_e$ detection.

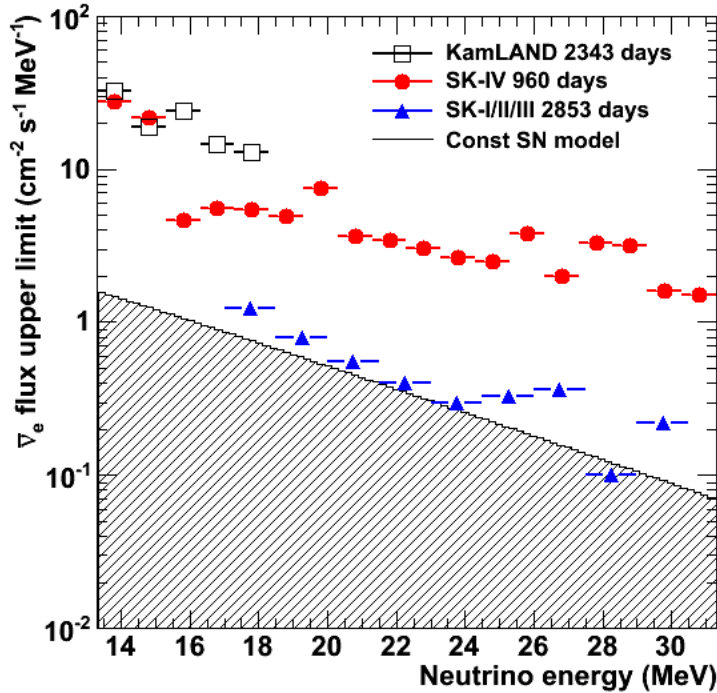


Figure 1.5 The $\bar{\nu}_e$ flux upper limit from KamLAND^[35], SK-I/II/III^[36] and SK-IV results^[13]. The flux of SRN using the constant SN rate model is plotted in shadow.

However, the flux upper limits depended on the estimation of background. For ${}^9\text{Li}$ and reactor neutrino background, the estimations are rather robust since they can

be directly obtained from data. However, the dominant NC background was given from the spectrum fit in Fig. 1.6 since there was no reliable estimate.

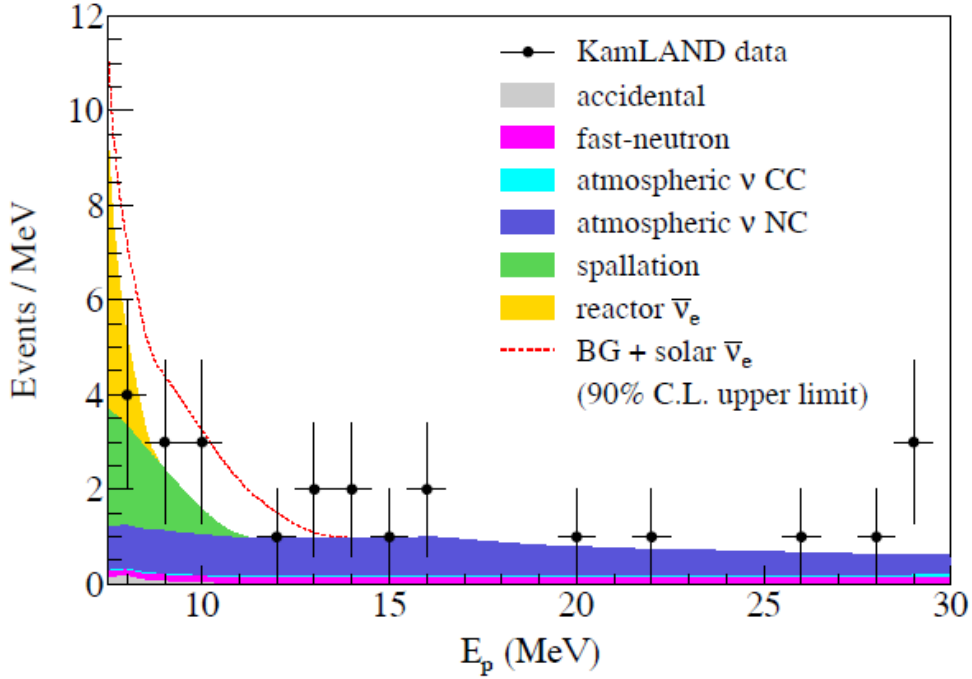


Figure 1.6 The distribution of prompt positron energy for the final $\bar{\nu}_e$ sample at KamLAND^[35].

1.5.2 Search at SK-I/II/III

The SRN search result at SK-I/II/III can be found in Ref.^[36]. Fig. 1.7 shows the positron energy spectrum of the final $\bar{\nu}_e$ sample in SK-III as an example. SK-I and SK-II are done in a similar fashion. The search analyzed the electron/positron spectrum without detecting the delayed neutron. The $\bar{\nu}_e$ energy threshold could only get down to 17.3 MeV because of the spallation background. In this search, the major backgrounds were found to be ν_μ CC, ν_e CC, μ/π and NC events. Among all these backgrounds, the decay electrons/positrons from the invisible muons produced by the ν_μ CC are dominant. The final spectrum of the data set were fitted with 5 components, and no significant SRN signal was found. Due to the large exposure and high efficiency in electron/positrons detection, SK-I/II/III put the best upper limits above 17.3 MeV.

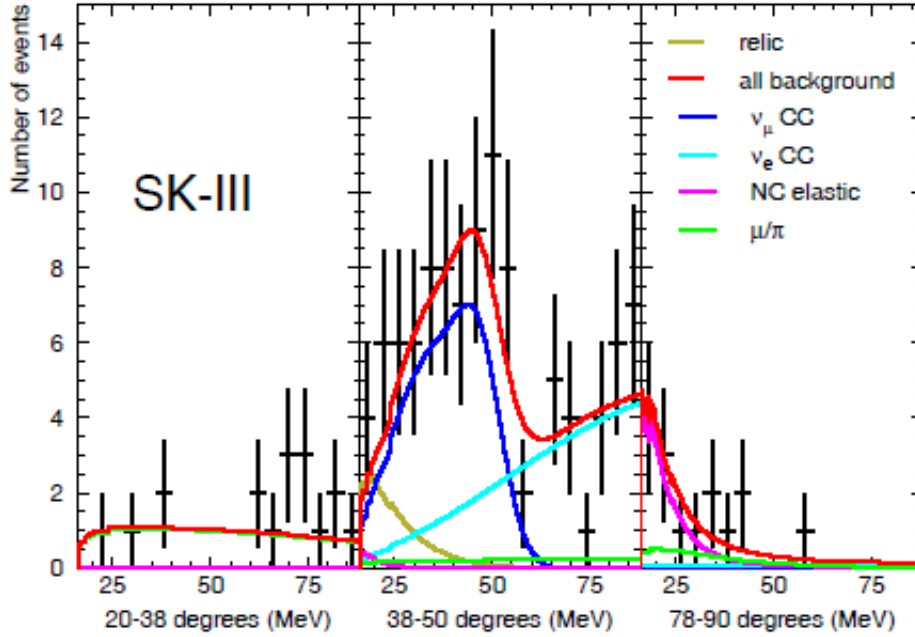


Figure 1.7 The distribution of positron energy for the final $\bar{\nu}_e$ sample at SK-III^[36].

1.5.3 Search at SK-IV

The SRN search result in SK-IV can be found in Ref.^[13]. Fig. 1.8 shows the positron energy spectrum of the final $\bar{\nu}_e$ sample at SK-IV. This was the first time that SK could use the delayed coincidence to identify the IBD events. The energy threshold was lowered down to 13.3 MeV from 17.3 MeV because of the application of neutron tagging. The SRN search was conducted in 13.3 MeV - 31.3 MeV and no SRN signal was found. The major background was the spallation background, solar neutrinos, invisible muon events and atmospheric $\bar{\nu}_e$ events, among which the spallation background were dominant. Model independent upper limits of flux were extracted for each MeV bin, giving competitive values in the world below 17.3 MeV although the neutron tagging efficiency is only $\sim 20\%$ at 1% accidental background level. The search could not go down below 13.3 MeV due to the huge spallation background. Therefore, the neutron tagging with a better signal-to-noise ratio is expected in order to cover the whole golden energy window.

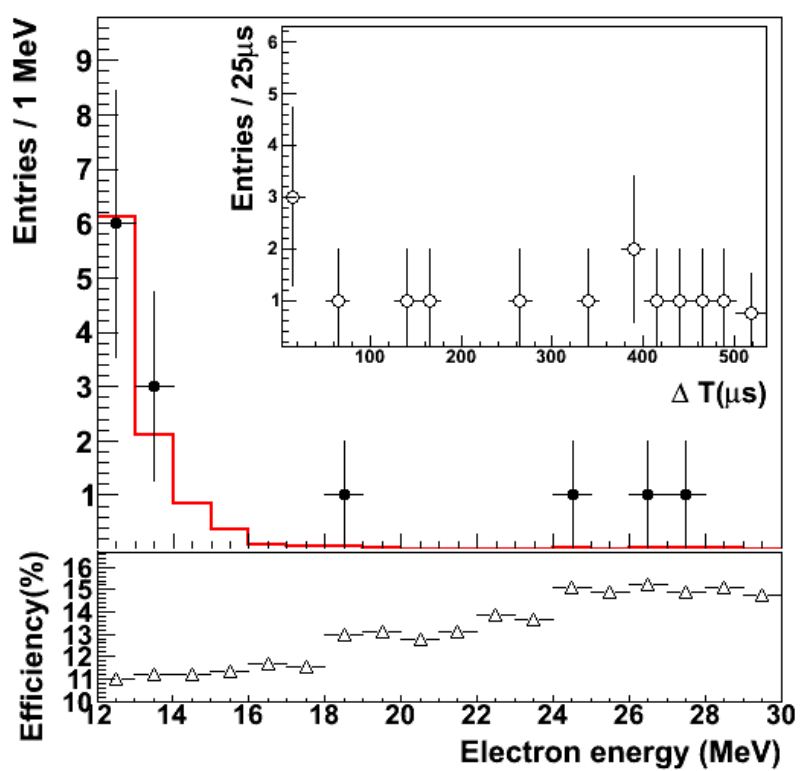


Figure 1.8 The distribution of positron energy for the final $\bar{\nu}_e$ sample at SK-IV^[13].

Chapter 2 The Super-Kamiokande Detector

2.1 Detector Overview

Super-Kamiokande is a cylindrical water Cherenkov detector, which contains 50-kton pure water^[37]. The 1,000 m overburden of rock (2,700 m.w.e.) reduces the cosmic ray muons by about 5 orders of magnitude. The detector can be optically separated into two parts: an inner detector (ID) and an outer detector (OD). The ID is viewed by 11,129 20-inch inward-pointing Photon Multiplier Tubes (PMTs), while the OD is viewed by 1,885 8-inch outward-pointing PMTs to veto the cosmic ray muons. Fig. 2.1 shows the schematic view of the detector.

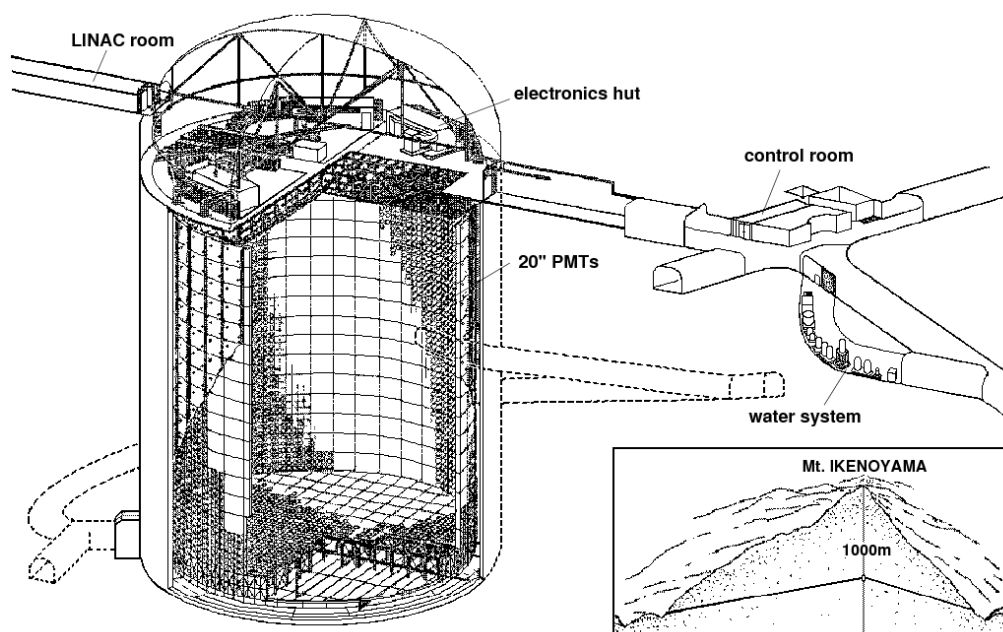


Figure 2.1 Schematic view of the SK detector.

The detector has a diameter of 39.3 m and a height of 41.4 m. The coordinate the SK detector uses is a Cartesian coordinate system in which the origin is at the center of the ID; the $+z$ axis is to the top, $+x$ is to the column with the first PMT and $+y$ follows the right-hand rule. Due to the large number of low energy background, events within 2 m to the wall of ID are not used for physics analysis. The remaining volume in the ID is referred to as the fiducial volume (FV) with 22.5 kton. Between the ID and the OD is the

support structure with a thickness of ~ 55 cm. For each frame of the support structure, the number of OD PMTs and the number of ID PMTs are installed with a ratio of 1:6. The outside wall of the support structure is surrounded by a Tyvek sheet to improve the light sensitivity of the OD. The inside wall of the support structure is surrounded by a black sheet of the polyethylene terephthalate to reduce the reflection of the light. On the top of the detector is the research dome, which houses four electronics huts and one central control room.

SK has four phases from SK-I to SK-IV. The detector began operation in April, 1996 with a photon coverage of $\sim 40\%$. In July, 2001, the detector was stopped for regular maintenance. However, a PMT exploded when $\sim 75\%$ of the detector was refilled with water after the maintenance. The shock wave produced by the PMT explosion destroyed almost half of the PMTs. The period from April, 1996 to July, 2001 is referred to as SK-I. After the accident, the PMTs were re-distributed with a photon coverage of $\sim 19\%$. Each PMT was protected with an acrylic cover and a fiberglass reinforced plastic (FRP) case to prevent the similar accident in SK-I. The period from October, 2002 to October, 2005 is referred to as SK-II. During SK-II operation period, new PMTs were manufactured. The resumption of PMTs almost took one year. The detector resumed operation with a coverage of $\sim 40\%$ after the full reconstruction. The period from June, 2006 to August, 2008 is referred to as SK-III. In August, 2008, both the electronics and the data acquisition (DAQ) system were upgraded, data hereafter is referred to as SK-IV.

2.2 Detection Principle

When a charged particle travels faster than the speed of light in medium, it will radiate Cherenkov light with a cone pattern along its path. The Cherenkov angle θ_c is defined as the angle between the direction of charged particle and the direction of the Cherenkov light and can be calculated by:

$$\cos \theta_c = \frac{1}{\beta n(\lambda)} \quad (2-1)$$

where β is the relative speed of the charged particle over the speed of light in vacuum, and $n(\lambda)$ is the refractive index with a dependence on wavelength. In pure water, the refractive index is about 1.33 at 589 nm. For ultra relativistic particles, the Cherenkov angle θ_c is 42° . Usually the electrons/positrons are the case, while heavier particles (μ , π) have lower Cherenkov angles in the energy range of interest. The energy threshold for

charged particles to emit Cherenkov light can be determined by:

$$E_{\text{thre}} = \frac{m}{\sqrt{1 - (1/n)^2}}. \quad (2-2)$$

where m is the rest mass of the charged particle. The number of the Cherenkov photons per unit length per unit wavelength can be expressed by the following equation:

$$\frac{d^2N}{d\lambda dx} = \frac{2\pi z^2 \alpha}{\lambda^2} \left(1 - \frac{1}{\beta^2 n^2(\lambda)}\right) = \frac{2\pi z^2 \alpha}{\lambda^2} \sin^2 \theta_c \quad (2-3)$$

where z is the particle charge in unit of e , α is the fine structure constant.

2.3 Photomultiplier Tubes

Fig. 2.2 shows an overview of 20-inch PMT (R3600)^[38], which was developed by Hamamatsu Photonics. The photo-cathode is made of baillkali (Sb-K-Cs) and is sensitive to photons with wavelength in 300 ~ 600 nm. The maximum quantum efficiency is ~ 20% as shown in Fig. 2.3. The number of photo-electrons (p.e.) produced via the photoelectric effect can be amplified with a gain ~ 10^7 by the 11 chain dynodes. The dark noise in SK-I was ~ 3.5 kHz with a threshold of 0.25 p.e. and now increases due to additional radioactivity from the acrylic cover and the FRP case.

There are 26 Helmholtz coils deployed surrounding the wall of the detector to reduce the earth magnetic field from 450 mG to 50 mG.

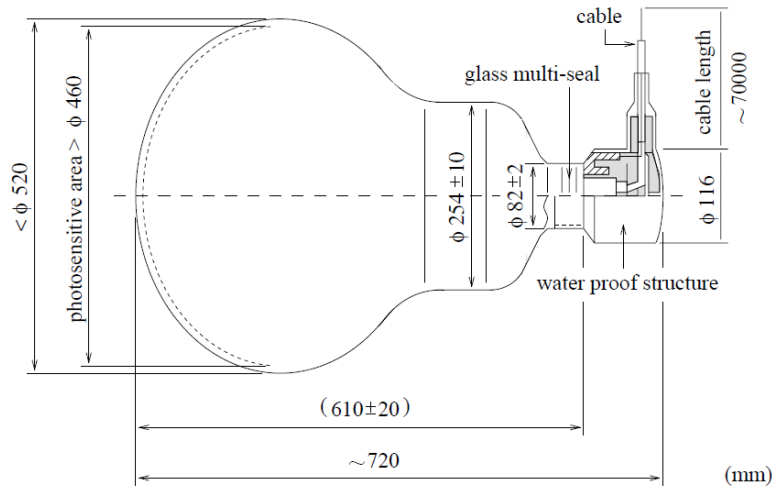


Figure 2.2 An overview of the Hamamatsu R3600 PMT.

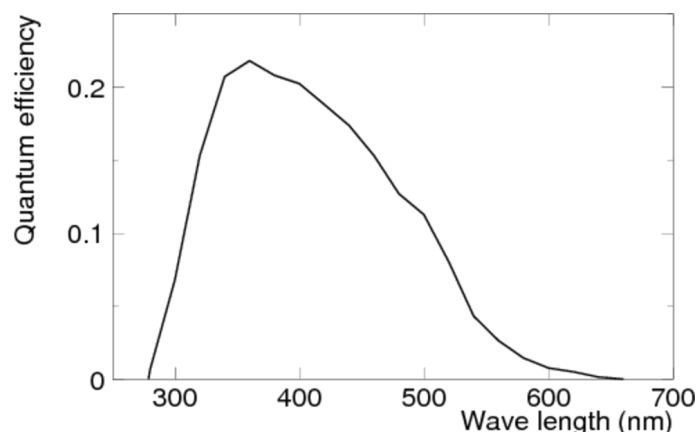


Figure 2.3 The quantum efficiency of the Hamamatsu R3600 PMT as a function of wavelength.

2.4 Water Systems

The water transparency of the detector should be as high as possible so that the Cherenkov light will not be attenuated before arriving at the PMTs. The radioactivity in water should also be as low as possible, especially for low energy analysis. To achieve the goals described above, a water purification system was developed as shown in Fig. 2.4.

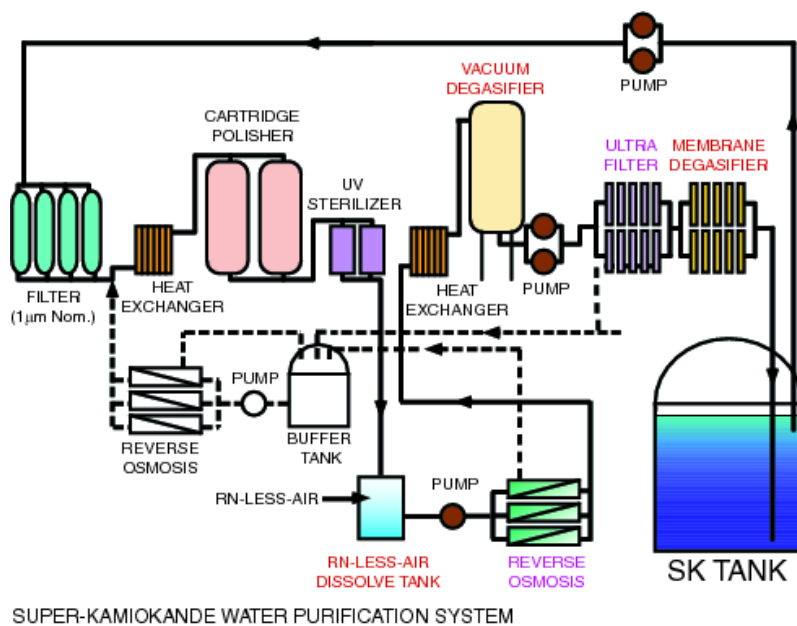


Figure 2.4 A schematic view of the water purification system at SK.

The water is filled from the bottom of the detector and drained from the top of the detector. The $1\ \mu\text{m}$ filter is to filter large particles. The heat exchanger keeps the water temperature at a constant ($\sim 13^\circ$) to reduce the convection, the grow of the bacteria and PMT dark noise. The cartridge polisher is to remove heavy ions. The ultra-violet (UV)

sterilizer kills the bacteria in the water. The reverse osmosis removes large particles with more than 100 molecules in weight. The vacuum de-gasifier removes dissolved oxygen and radon from the water. The ultra filter removes small particles with a size above 10 nm in diameter. The membrane de-gasifier further removes the dissolved radon and other gases.

The water is circulated with a flow of about 60-ton per hour during the normal operation of the detector. A schematic view of the recirculation system is shown in Fig.2.5. The water temperature is monitored for both the ID and OD. Because of the flow of water circulation, the water temperature is uniform below -11 m of z position and it slowly goes up by only about 0.2°C from the bottom half to the top half of the tank as shown in in Fig.2.6.

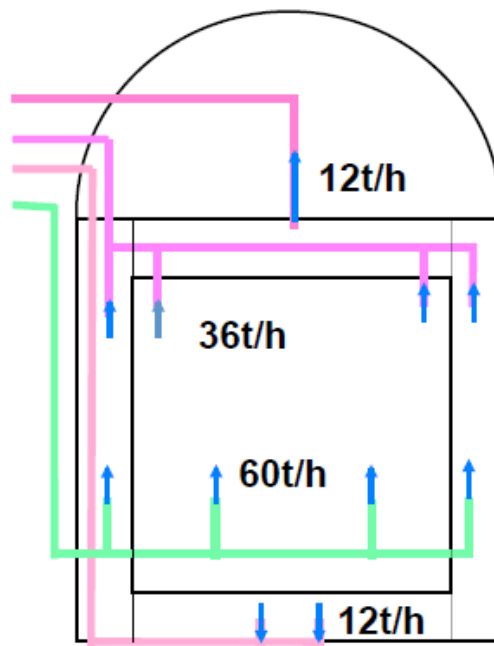


Figure 2.5 A schematic view of the water circulation system at SK.

2.5 Radon Free Air Systems

The air flow in the mine is contaminated by the radon leakage from the surrounding rock. The radon concentration can produce low energy background. High radon level

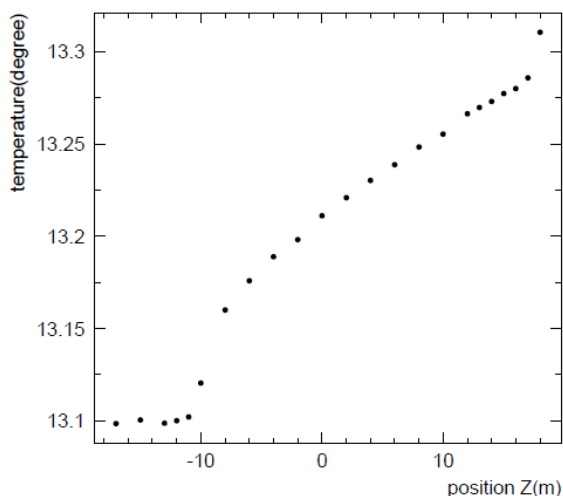


Figure 2.6 The z -dependence of the water temperature.

could also be harmful to the workers in the mine. The radon level is high in summer, usually $\sim 2000 \text{ Bq/m}^3$. While in winter, the radon level gets down to $\sim 200 \text{ Bq/m}^3$. Fig. 2.7 shows a schematic view of the air purification system. After the filtration, the radon level is kept at $\sim 40 \text{ Bq/m}^3$ in the experimental area throughout the year.

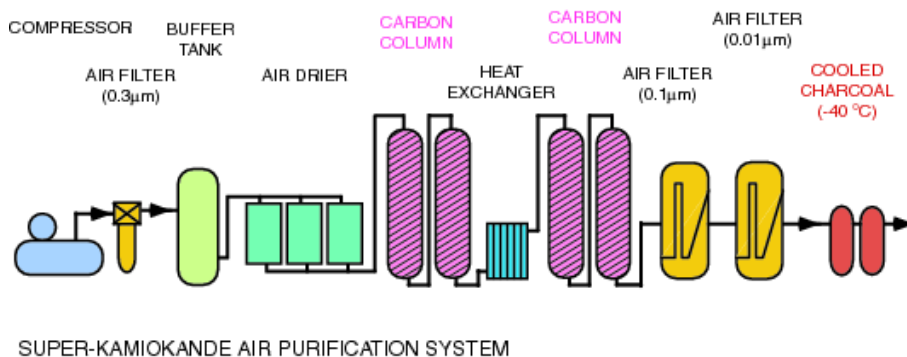


Figure 2.7 A schematic of the air purification system at SK.

2.6 Front-end Electronics and Data Acquisition System

The front-end electronics and DAQ system were both upgraded in August, 2008 for the purpose of stable data-taking in next decades and larger data throughout. Each PMT hit can be recorded without loss so that a software trigger can be conducted. Several triggers are implemented. The time windows for the low energy (LE) trigger, the high energy (HE) trigger and the super high energy (SHE) trigger are all $40 \mu\text{s}$, ranging from

$-5 \mu\text{s}$ to $35 \mu\text{s}$. The first $5 \mu\text{s}$ data ($-5 \mu\text{s} \sim 0 \mu\text{s}$) can be used for the pre-activity gamma study, while the later $35 \mu\text{s}$ data can be used for the post-activity (mainly decay-e) study. When a SHE trigger is fired with no OD trigger, an after trigger (AFT) is issued for $500 \mu\text{s}$ data without threshold. The SHE + AFT scheme is primarily used to detect the coincident prompt positron and delayed neutron from the IBD reaction. Implementation of this trigger scheme has motivated many physics studies at SK. The threshold for the LE, HE trigger is 47, 50 hits in 200 ns, respectively. The threshold for the SHE trigger was 70 hits at the beginning of SK-IV, and was lowered down to 58 hits in the summer of 2011.

Fig. 2.8 shows a block diagram of the DAQ system at SK-IV. Signals from the PMTs are fed into newly developed front-end electronics: QTC (charge-to-time converter) Based Electronics with Ethernet, which is called as QBEE. Each QBEE has 24 analog input channels with a dynamic range of change from 0.2 to 2500 pC, which is about 5 times longer than the previous one^[39]. There are 8 QTC chips in one QBEE to integrate the input charge and output a pulse with a width proportional to the amount of the change. This pulse is then fed to a Time-to-Digital converter (TDC) to measure its width by determining the leading and trailing edges of time. The digitalized width and timing information from TDC is sent to a Field Programmable Gate Array (FPGA) for further processing^[40].

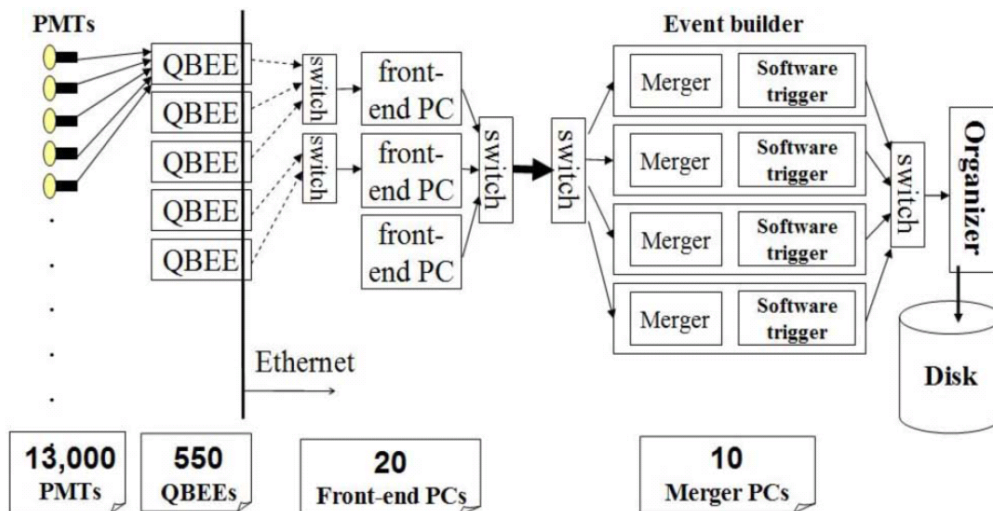


Figure 2.8 A block diagram of the DAQ system at SK-IV^[41].

Chapter 3 Detector Calibration

Detector calibration is to ensure high quality measurements. This chapter will describe the energy calibration, water transparency measurement and PMT calibration. Details about the detector calibration at SK can be found in Ref^[37,42].

3.1 Energy Calibration

The accuracy of energy measurement is very critical for the analysis of low-energy events. In this section, the energy calibration is described.

3.1.1 LINAC Calibration

A small linear accelerator (LINAC) obtained from a hospital is used to give a fine calibration of the energy. Fig.3.1 shows a schematic view of the LINAC system. The positions marked from 1 to 6 are used to measure the energy with position dependence. The energy of electrons from the LINAC is tunable, ranging from 5 to 18 MeV. Fig.3.2 shows the energy difference between the LINAC data and the MC simulation sample for 6 positions and 6 energy points (36 points in total). The energy scale variation is determined to be less than 1%.

The energy resolution, vertex resolution and angular resolution can also be obtained from the LINAC data. Details can be found in Ref^[43].

The major drawback of the LINAC is that the electrons produced by the LINAC are only for downward going, so the angular dependence of energy cannot be calibrated. This will be solved by the DT calibration described in the next subsection.

3.1.2 DT Calibration

As a cross check of the absolute energy scale, a deuterium-tritium (DT) neutron generator is used^[44]. The reaction ${}^2\text{H} + {}^3\text{H} \rightarrow {}^4\text{He} + n$ can produce isotropical neutrons with an energy of 14.2 MeV. These neutrons can interact with ${}^{16}\text{O}$ to produce ${}^{16}\text{N}$, which can decay to $\beta\gamma$ modes or β modes with a branch ratio (BR) of 66% or 28%, respectively.

The DT calibration process is less time consuming and is performed every few months. Unlike the LINAC, the DT produces electrons and γ 's isotropically so that the

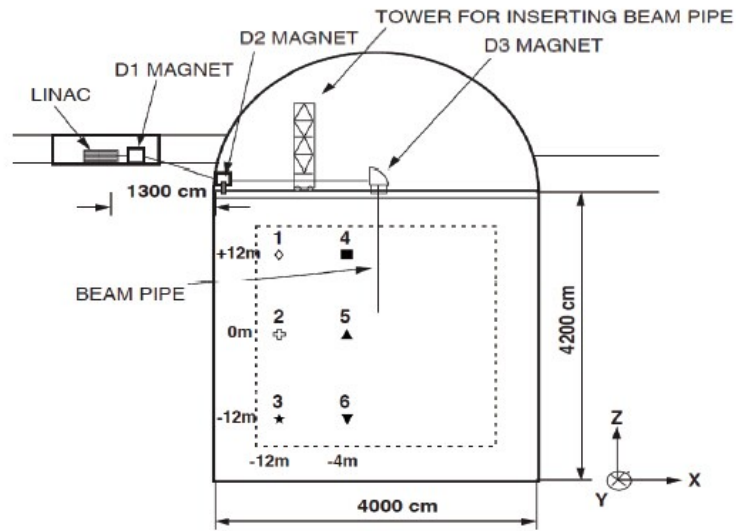


Figure 3.1 A schematic view of the LINAC calibration system.

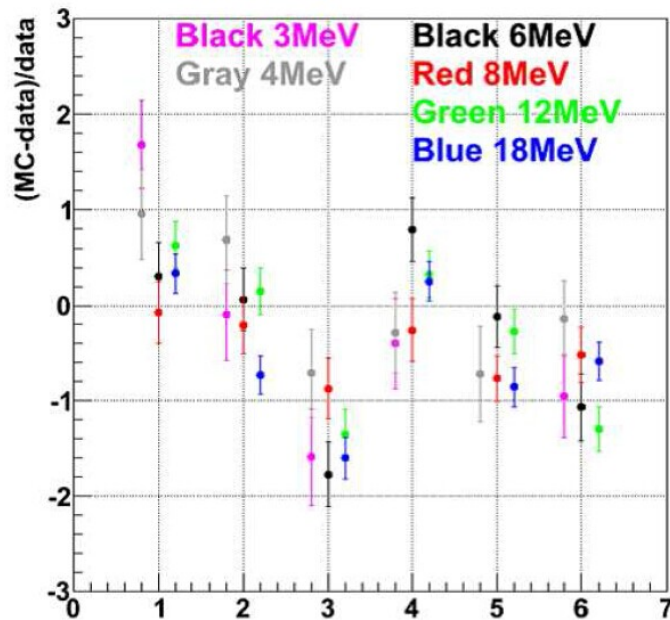


Figure 3.2 The energy difference between the LINAC data and the MC simulation sample for 6 different positions and 6 different energy points (36 points in total). The energy scale variation is determined to be less than 1%.

direction dependence can also be studied. The energy scale obtained from the DT agrees with that from the LINAC within 1%.

3.1.3 Decay Electrons

To check the time variation of the absolute energy scale, data from decay-e's are used. To select the decay-e events from stopping muons, several selection criteria are applied as follows:

- the time difference (ΔT) between a decay-e and a stopping muon is required to be $3.0 < \Delta T < 8.0 \mu\text{s}$ (to keep the same selection criteria as SK-III);
- the distance between the decay-e and the stopping muon should be less than 250 cm;
- the number of PMT hits within a 50-ns time window should be greater than 50 ;
- the FV cut is also applied.

After these cuts, about 700 μ -e decay events can be selected every day.

The effective PMT hits in the 50-ns time window are calculated from the μ -e decay sample. Fig.3.3 shows the time variation of the effective hits with a water transparency correction. The variation of effective hits is within $\pm 0.5\%$.

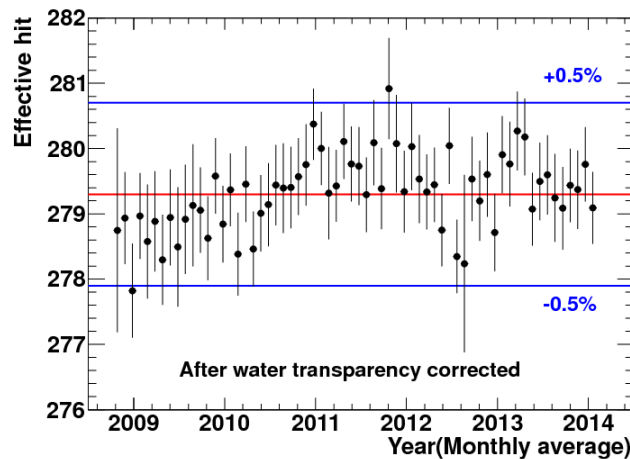


Figure 3.3 The time variation of the effective hits with a water transparency correction from the decay-e data during SK-IV.

3.2 PMT Calibration

SK uses PMTs to measure both charge and time. The total charge deposit by a particle is used to measure the energy, while the arrival time of the Cherenkov photon is used to reconstruct the vertex and the flight direction of the particle. This section will introduce PMT calibration.

3.2.1 PMT Gain

The conversion factor of absolute gain is determined by a Ni-Cf source. Neutrons from Cf can be captured by Ni and then emit γ 's with energy ranging from 6 to 9 MeV. Low energy γ 's usually ($\sim 99\%$) cause each hit PMT with only one p.e.. The charge distribution for single photo-electron is used to determine the conversion factor from its peak position. This factor is then used to translate charge into p.e. for a given PMT. In SK-IV, the mean of absolute gains is ~ 2.658 pC/p.e.

In addition to the absolute gain, the relative gains for all the PMTs are also calibrated to make sure the uniform response of the detector. Two measurements are conducted using a light source with a constant intensity. The first one uses a high intensity flasher. The charge detected by the i -th PMT ($Q_{\text{obs}}(i)$) is described below:

$$Q_{\text{obs}}(i) \propto I_{\text{high}} \times A(i) \times \text{QE}(i) \times G(i), \quad (3-1)$$

where $I_{\text{high}}(i)$ is an average of the high intensity, $A(i)$ is the acceptance of the i -th PMT, $\text{QE}(i)$ is the quantum efficiency of the i -th PMT and $G(i)$ is the relative gain. The second one uses a low intensity flasher to ensure most of PMTs with a single photon hit. The number of hits on the i -th PMT is described as follows:

$$N_{\text{hit}}(i) \propto I_{\text{low}}(i) \times A(i) \times \text{QE}(i). \quad (3-2)$$

where $N_{\text{hit}}(i)$ is the number of hits on the i -th PMT, while $I_{\text{low}}(i)$ is an average of the low intensity. From Eqn. (3-1) and Eqn. (3-2), the relative gain for each PMT is obtained ignoring the common and constant factor:

$$G(i) \propto \frac{Q_{\text{obs}}(i)}{N_{\text{hit}}(i)} \quad (3-3)$$

Fig. 3.4 shows the distribution of relative gain scaled by the average value of all PMTs. The $1-\sigma$ spread is about 6%.

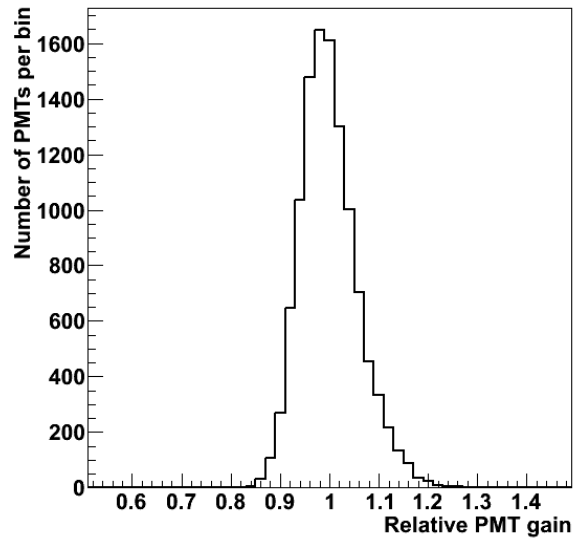


Figure 3.4 The distribution of relative PMT gain. The $1\text{-}\sigma$ spread is about 6%.

3.2.2 Time Walk Effect

Due to the 'time walk' effect, the response of PMT could be different even for that the true arrival times are exactly the same. A scatter plot of the PMT timing vs the charge (known as "T-Q map") is shown in Fig. 3.5^[42]. Larger timing values mean earlier hits. At SK, the time walk effect is corrected for the time measurement according to the charge value by applying the time offset from the T-Q map.

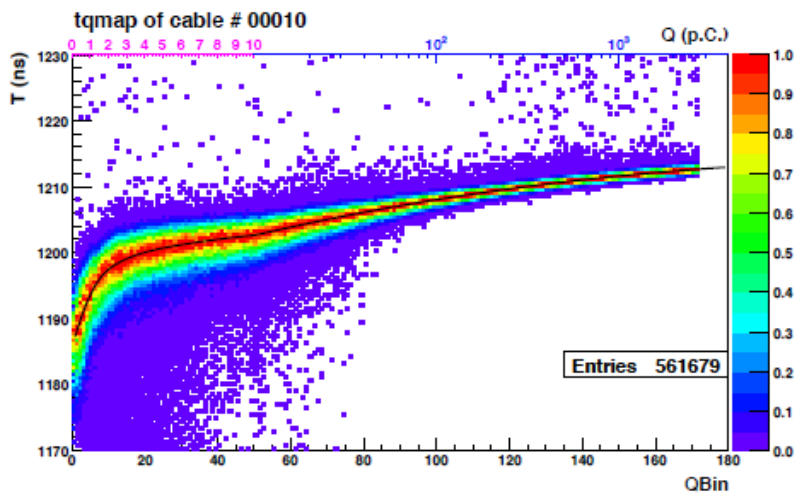


Figure 3.5 A scatter plot of the PMT timing and charge, known as "TQ-map". The horizontal axis shows the PMT charge (Qbin) and the vertical axis shows the PMT timing^[42].

3.3 Water Transparency Measurement

Two methods are developed in order to measure the water transparency. One is from the N_2 laser measurement, and the other one is from the decay-e measurement.

3.3.1 Laser Measurement

Light attenuation follows the exponential law and is a function of wavelength λ :

$$I(\lambda) = I_0(\lambda) \exp(-l/L_{\text{atten}}(\lambda)) \quad (3-4)$$

where l is the travel distance of light, $I(\lambda)$ is the intensity at distance l , $I_0(\lambda)$ is the initial intensity, $L_{\text{atten}}(\lambda)$ is the attenuation length caused by both the absorption and scattering in water and is referred to as the water transparency. For SRN analysis, the water transparency obtained from the laser measurement is only used as a cross check of the water transparency measurement from the decay-e data.

$L_{\text{atten}}(\lambda)$ is defined in terms of the absorption (α_{abs}) and scattering (α_{scat}) parameters in MC model with the following formula:

$$L_{\text{atten}}(\lambda) = \frac{1}{\alpha_{\text{abs}}(\lambda) + \alpha_{\text{sym}}(\lambda) + \alpha_{\text{asym}}(\lambda)}, \quad (3-5)$$

where $\alpha_{\text{abs}}(\lambda)$ is the absorption co-efficiency, $\alpha_{\text{sym}}(\lambda)$ is the scattering co-efficiency from Rayleigh scattering together with the symmetric part of Mie scattering, while $\alpha_{\text{asym}}(\lambda)$ is the scattering co-efficiency from the asymmetric part of Mie scattering.

A series of wavelength 337 nm, 375 nm, 405 nm, 445 nm, 473 nm from the N_2 laser are used to measure the absorption and scattering co-efficiency. Fig.3.6 shows the typical water transparency as a function of wavelength, which is used in the MC simulation.

3.3.2 Decay Electrons

The decay-e sample is selected with the criteria given in Section 3.1.3. Using the relationship between the light intensity of a hit PMT and the distance the light travelled as shown in Fig. 3.7, the water transparency can be obtained from the inverse of the fit slope. The first bins are not applied for this measurement since the strange effect induced by the short distance the light travelled has never been completely understood. The contribution of each hit PMT are corrected by both the occupancy and the geometry (See Section 4.2). Fig. 3.8 shows the measured water transparency from the decay-e data during the SK-IV period. The daily water transparency is used as the input for the energy reconstruction.

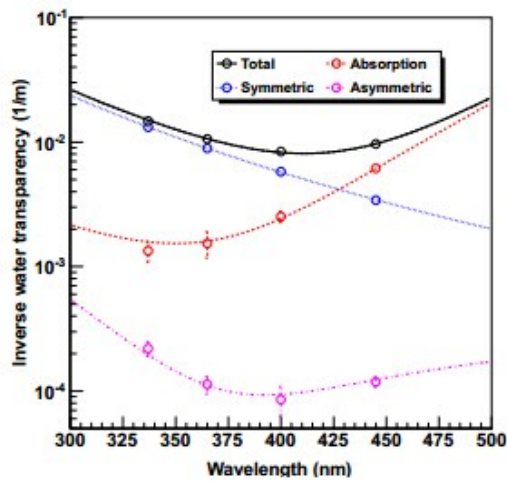


Figure 3.6 The typical water transparency as a function of wavelength.

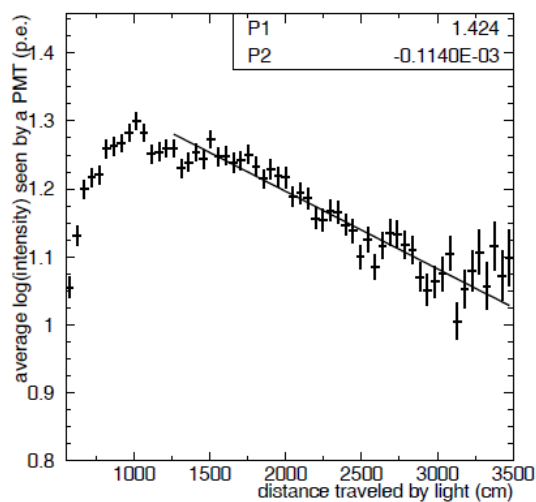


Figure 3.7 The distribution of light intensity of a hit PMT vs. the distance the light travelled.

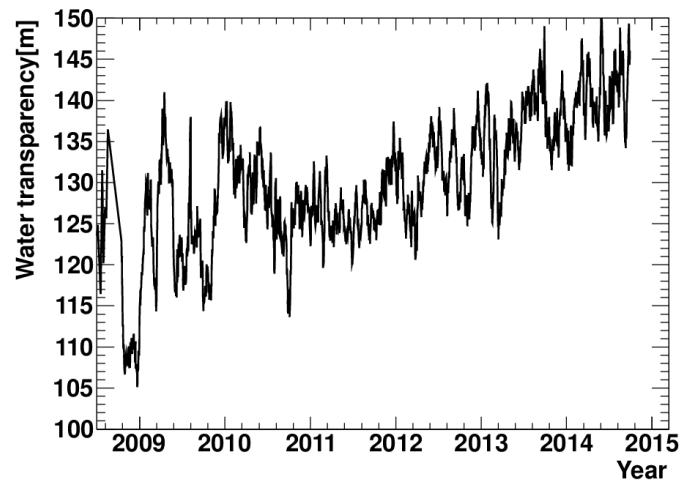


Figure 3.8 The water transparency of SK-IV measured from the decay-e data sample.

Chapter 4 Event Reconstruction

Event reconstruction will give the vertex position, direction and energy, etc. Events with lower than 1,000 PMT hits are used for low energy reconstruction while events with greater than 1,000 PMT hits (OD & HE trigger are also required) are used for the muon track reconstruction.

4.1 Vertex Reconstruction

Electrons/positrons with energy lower than 100 MeV are considered as point sources since their travel distances are less than a few ten centimeters (~ 20 cm for a 50 MeV electron). At SK, electrons and positrons cannot be differentiated and the same event reconstruction is applied. Among all the vertex fitters, BONSAI (Branch Optimization Navigating Successive Annealing Iterations)^[45] gives the best vertex resolution for low energy events.

In BONSAI, the likelihood function for the residual time distribution is obtained from the LINAC calibration data. The distribution of residual time for dark noise is assumed as flat. The vertex is given when the likelihood function is maximized. The vertex resolution is ~ 55 cm for a 10 MeV electron from the LINAC study.

4.2 Energy Reconstruction

The energy of a charged particle is proportional to the number of PMT hits in a 50 ns time window (N50). To reconstruct the energy, the effective N50 (N_{eff}) is used as described in the following expression:

$$N_{\text{eff}} = \sum_{i=1}^{N_{50}} \left\{ (X_i + \epsilon_{\text{tail}} - \epsilon_{\text{dark}}) \times \frac{N_{\text{all}}}{N_{\text{norm}}} \times \frac{R_{\text{cover}}}{S(\theta_i, \phi_i)} \times \exp\left(\frac{r_i}{L_{\text{atten}}}\right) \times G_i(t) \right\} \quad (4-1)$$

where X_i is the occupancy defined below:

$$X_i = \begin{cases} \frac{\log \frac{1}{1-x_i}}{x_i}, & x_i < 1 \\ 3.0, & x_i = 1 \end{cases} \quad (4-2)$$

x_i is the fraction of PMTs hits in a 3×3 patch. If all the PMTs in the patch are hit, then $X_i=3$. ϵ_{tail} is corrected for the late time of PMT hits due to the multiple scattering.

ϵ_{dark} is subtracted to remove the dark noise effect. N_{all} is the number of all the 11,129 PMTs in SK-IV. N_{norm} is the number of properly operating PMTs. R_{cover} is the coverage of PMTs, which is equal to 40.41%. Fig. 4.1 shows the definition of θ_i and ϕ_i . $S(\theta_i, \phi_i)$ is a correction factor for the incident angle, which is shown in Fig.4.2. r_i is the distance from the vertex position of the particle to the position of the hit PMT and L_{atten} is the water transparency. $G_i(t)$ is the relative gain.

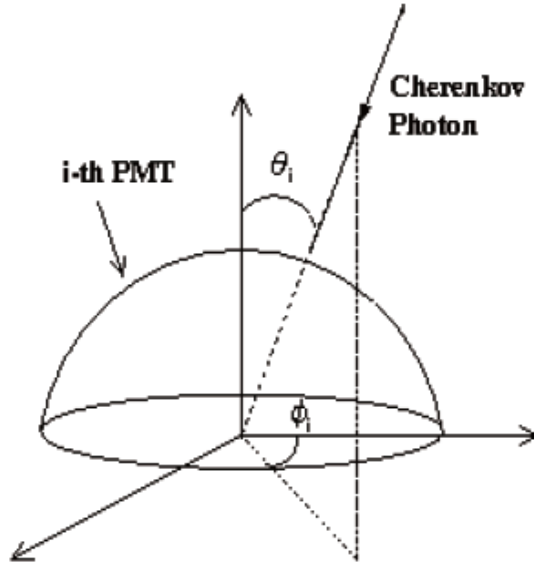


Figure 4.1 The definition of θ_i and ϕ_i .

The energy resolution is $\sim 14\%$ for a 10 MeV electron. Note that all particles are considered as electrons, so the reconstructed energies for other particles such as muons, pions are inappropriate. However, only electrons/positrons are left in the final sample using additional cuts. It is also noted that the energy used in this thesis is the total energy of electrons/positrons.

4.3 Direction Reconstruction

An angular likelihood function is obtained from the MC simulation. The likelihood function peaks around 42° of the Cherenkov angle and can expand a wide range due to the multiple scattering. Various directions are scanned until the likelihood function is

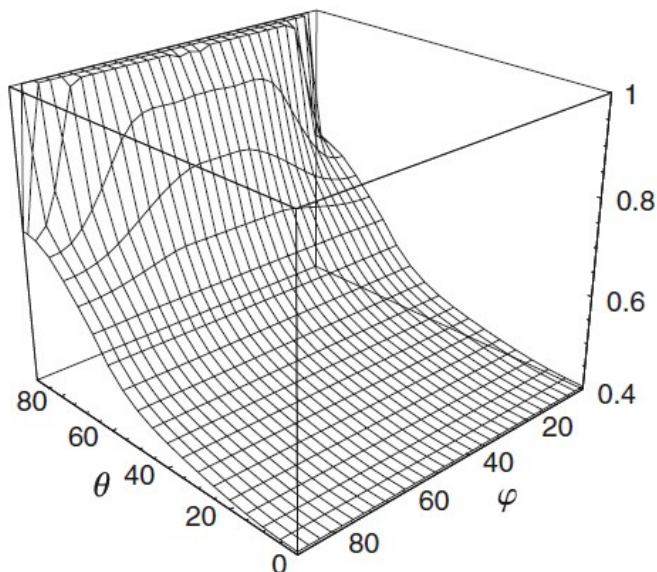


Figure 4.2 Incident angle correction $S(\theta_i, \phi_i)$ used in the energy reconstruction.

maximized. The angular resolution is $\sim 25^\circ$ for a 10 MeV electron and becomes better with the increase of energy.

4.4 Muon Reconstruction

Muon reconstruction plays an important role in the study of the spallation background. Cosmic-ray muon spallation induced radioactive isotopes are the major background for the low energy analysis above 6.5 MeV. This background can be removed using the spatial and temporal relationship between the low energy events and the preceding muon events. In this section, the muon fitters are described.

4.4.1 Muboy Fitter

Perhaps the most effective muon fitter at SK is Muboy as described in Refs^[46,47]. Muboy categorizes muons into 4 classes: single through-going muons, stopping muons, multiple muons and corner-clipping muons. Single through-going muons pass through the detector with only one track and are usually vertical downward; Stopping muons enter the detector and stop inside the detector; Multiple muons are the muon bundles with parallel tracks; Corner-clipping muons clipper the corner of the detector and are believed not to induce spallation background since no time correlation is found. At SK-IV, the time length of HE trigger event is enlarged to $40 \mu\text{s}$, during the time of $0\sim 35 \mu\text{s}$ un-tagged

muons may hide. In order to search for the un-tagged muons, a software trigger is applied requiring HE & OD trigger pair. This can remedy the loss of a few hundreds un-tagged muons per day.

4.4.2 Brute Force Fitter

For $\sim 1.5\%$ single through-going muons reconstructed by Muboy, the reconstruction may not be reliable since the return goodness is lower than 0.4. In such cases, muons are refitted by Brute Force Fitter (BFF). BFF can remedy $\sim 75\%$ of the poorly fitted muons reconstructed by Muboy. More details about BFF can be found in Ref. ^[48].

4.4.3 Energy Loss

The energy loss dE/dx for an energetic cosmic muon usually peaks around the spallation point. To make the distribution of dE/dx , the number of p.e.s in each 50 cm bin along the muon track are calculated.

4.5 Cherenkov Angle Reconstruction

The Cherenkov angle reconstruction is a key factor to remove non-e events such as μ/π 's and multiple γ 's. Electrons/positrons are usually ultra-relativistic events to have a Cherenkov angle of 42° , while μ/π events can have a smaller Cherenkov angle since they are less relativistic and multiple γ events can have a larger Cherenkov angle due to the isotropic pattern.

The Cherenkov angle is calculated from the distribution of the 3-PMT combinations. Each 3-PMT combination can give three hit vectors (from the reconstructed position to the hit PMT) and thus can determine a Cherenkov angle. The Cherenkov angle distribution can be obtained from all 3-PMT combinations. The Cherenkov angle is determined from the peak of the distribution instead of the mean value due to the multiple scattering.

Chapter 5 Event Simulation

5.1 Simulation Package

SKDETSIM^[49,50], the official simulation package at SK, is based on Geant 3.21. The tracking of particle and the response of the detector are well simulated and tested. The neutrino interactions are simulated by NEUT^[51] and hadronic interactions are simulated by a combination of SK codes and CARLO^[52,53].

5.2 Spallation Products

The spectrum of decay products (β and γ) from the spallation induced radioactive isotopes are simulated using the SKDETSIM. The decay information of the radioactive isotopes can be found in Refs.^[54–57]. In order to simulate the decay products, the following procedures are applied:

1) Simulation in the ID: The MC events are simulated in the full volume of the ID with both the position and the direction randomly distributed. For a β decay accompanied by a de-excitation γ , the positions of the β and γ are assigned to be the same while the directions of the β and the γ are given randomly with no correlation. The events are generated by taking into account the decay BRs of the radioactive isotopes.

2) Reconstruction: The events are reconstructed with the dedicated software tools described in Chapter 4.

3) FV cut: After the reconstruction, events in the FV of 22.5 kton are selected. The fraction of survival events after the FV cut is $22.5/32.5=0.69$.

5.2.1 ^{12}B Decay

The ^{12}B decays with a Q-value of ~ 13.4 MeV and a mean life time (τ) of ~ 29.1 ms. Fig. 5.1 shows the decay channels of ^{12}B , which can go through a β^- decay to ^{12}C on the ground state with a BR of $\sim 97.2\%$. For a β^- decay with the accompany of the de-excitation γ , the β^- and the γ are simulated individually in one event. All the decays of the radioactive isotopes are simulated in this fashion. Fig.5.2 shows the distribution of

the reconstructed energy from the β decay of ^{12}B . Due to the energy resolution effect, the energy distribution can have a higher tail. Also notice that the reconstructed energy is the sum of β (in total energy) + γ .

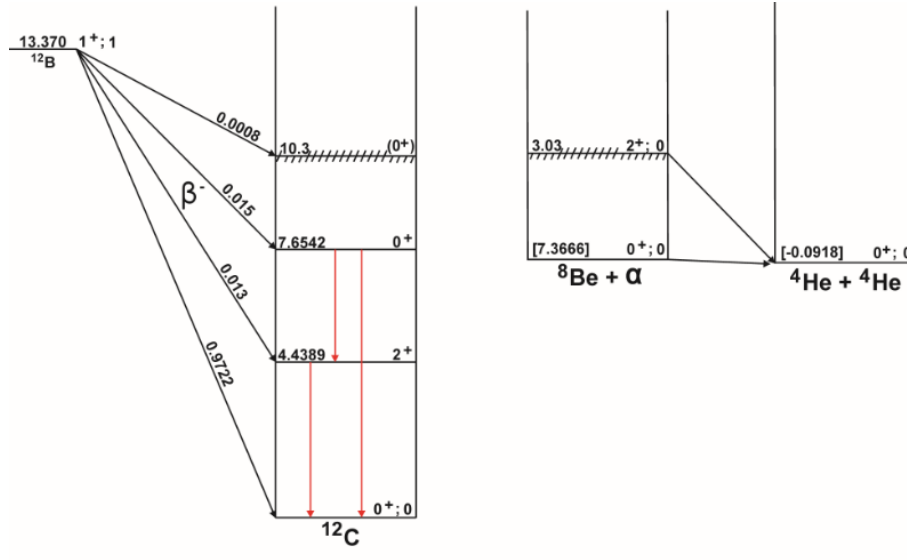


Figure 5.1 The decay channels of ^{12}B [56].

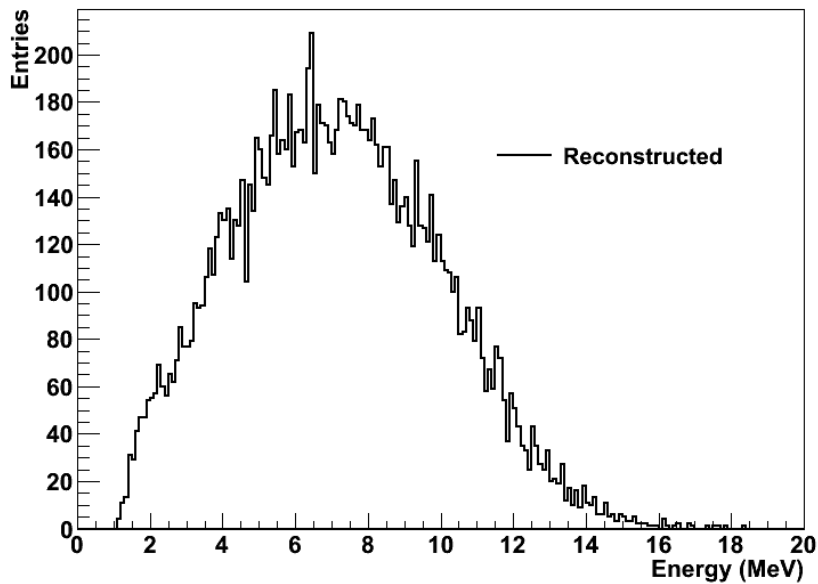


Figure 5.2 The distribution of the reconstructed energy from the β decay of ^{12}B .

5.2.2 ^{12}N Decay

The ^{12}N decays with a Q-value of ~ 17.3 MeV and a τ of ~ 15.9 ms. Fig. 5.3 shows the decay channels of ^{12}N , which can go through a β^+ decay to ^{12}C on the ground state with a BR of $\sim 94.6\%$. Fig.5.4 shows the distribution of the reconstructed energy from the β decay of ^{12}N .

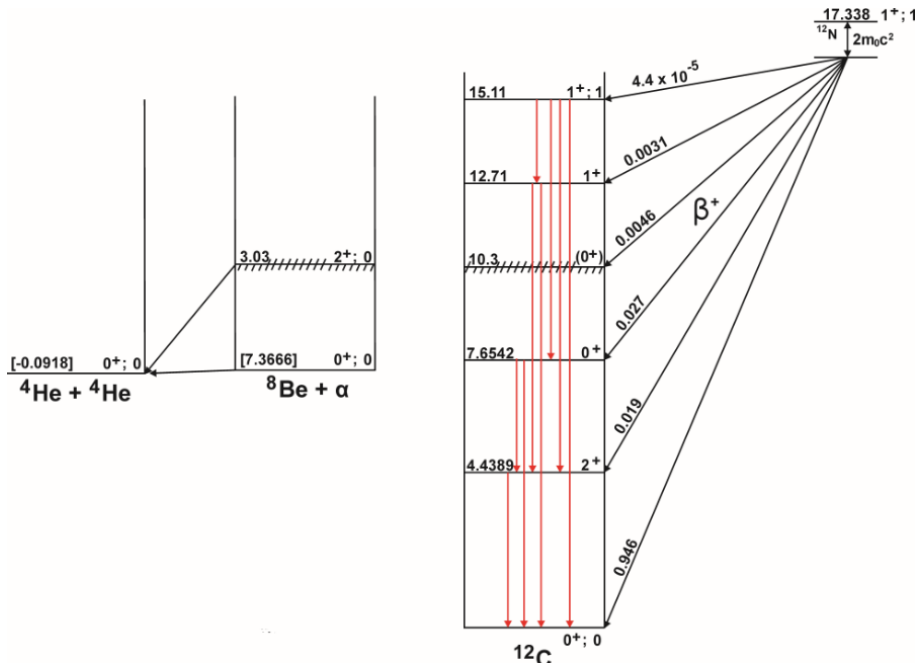


Figure 5.3 The decay channels of ^{12}N [56].

5.2.3 ^{16}N Decay

The ^{16}N decays with a Q-value of ~ 10.4 MeV and a τ of ~ 10.3 s. Fig. 5.5 shows the decay channels of ^{16}N . The decay of ^{16}N are dominated by its β^- decay to ^{16}O on the energy level of 6.1 MeV with a BR of $\sim 66\%$ [44], in which the endpoint energy of electron is 4.3 MeV and the energy of γ 's is 6.1 MeV. Another main decay channel of ^{16}N is the β^- decay to ^{16}O on the ground state with a BR of $\sim 28\%$, in which the endpoint energy of electron is 10.4 MeV. Other minor decay channels shown in Ref[44] are also simulated. Fig.5.6 shows the distribution of the reconstructed energy from the β decay of ^{16}N .

5.2.4 ^{11}Be Decay

The ^{11}Be decays with a Q-value of ~ 11.5 MeV and a τ of ~ 19.9 s. Fig. 5.7 shows the decay channels of ^{11}Be . The decay of ^{11}Be are dominated by its β^- decay to ^{11}B

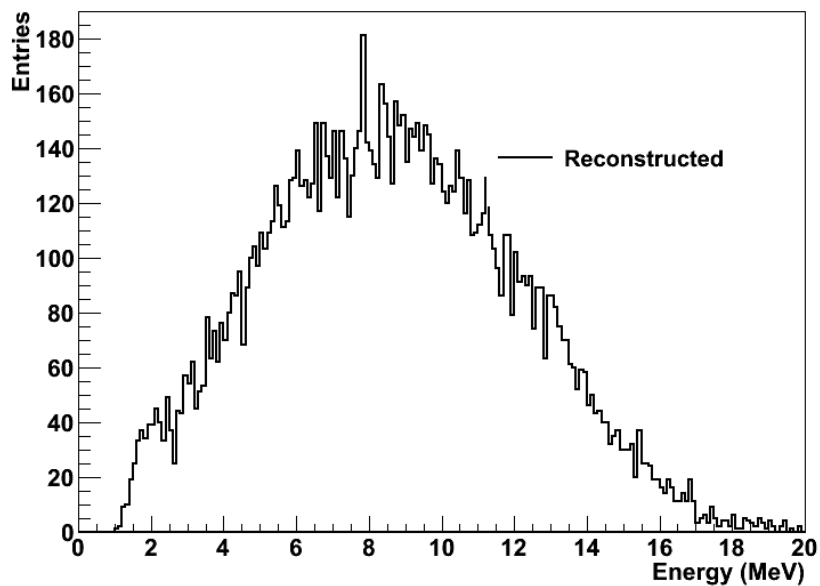


Figure 5.4 The distribution of the reconstructed energy from the β decay of ^{12}N .

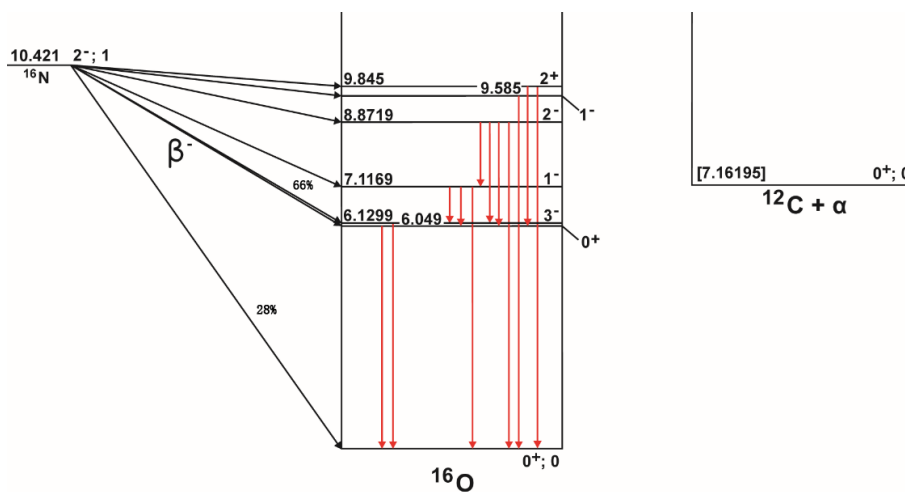


Figure 5.5 The decay channels of ^{16}N [56].

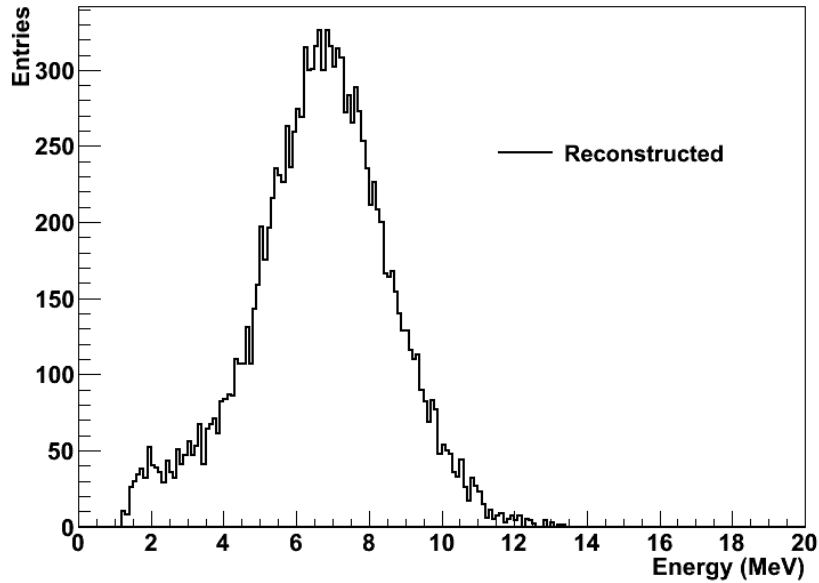


Figure 5.6 The distribution of the reconstructed energy from the β decay of ^{16}N .

on the ground state with a BR of $\sim 54.7\%$, in which the endpoint energy is 11.5 MeV. Another major channel of ^{11}Be decays to ^{11}B on the energy level of 2.1 MeV with a BR of 31.4%. Fig.5.8 shows the distribution of the reconstructed energy from the β decay of ^{11}Be .

5.2.5 ^9Li Decay

The ^9Li decays with a Q-value of ~ 13.6 MeV and a τ of ~ 0.26 s. Fig. 5.9 shows the decay channels of ^9Li , which decays to a final state of β^-n with a BR of 50.8%. Another major channel of ^9Li decays to ^9Be on the ground state with a BR of $\sim 49\%$. The left panel and the right panel of Fig. 5.10 show the distribution of the reconstructed energy from both the β and the βn decays of ^9Li , respectively. The peak around 1.5 MeV in the right panel of Fig. 5.10 is due to the fact that the 3% (1%) of ^9Li decays to ^9Be on the energy level of 11.8 (11.3) MeV.

5.2.6 ^8He Decay

The ^8He decays with a Q-value of ~ 10.7 MeV and a τ of ~ 0.17 s. Fig. 5.11 shows the decay channels of ^8He . The major decay of ^8He is to ^8Li on energy level of 0.98 MeV with a BR of $\sim 84\%$ ($\beta^- + \gamma$). ^8He decays to a final state of β^-n with a BR of 16%. Fig.5.12 shows the distribution of the reconstructed energy from both the β and the βn

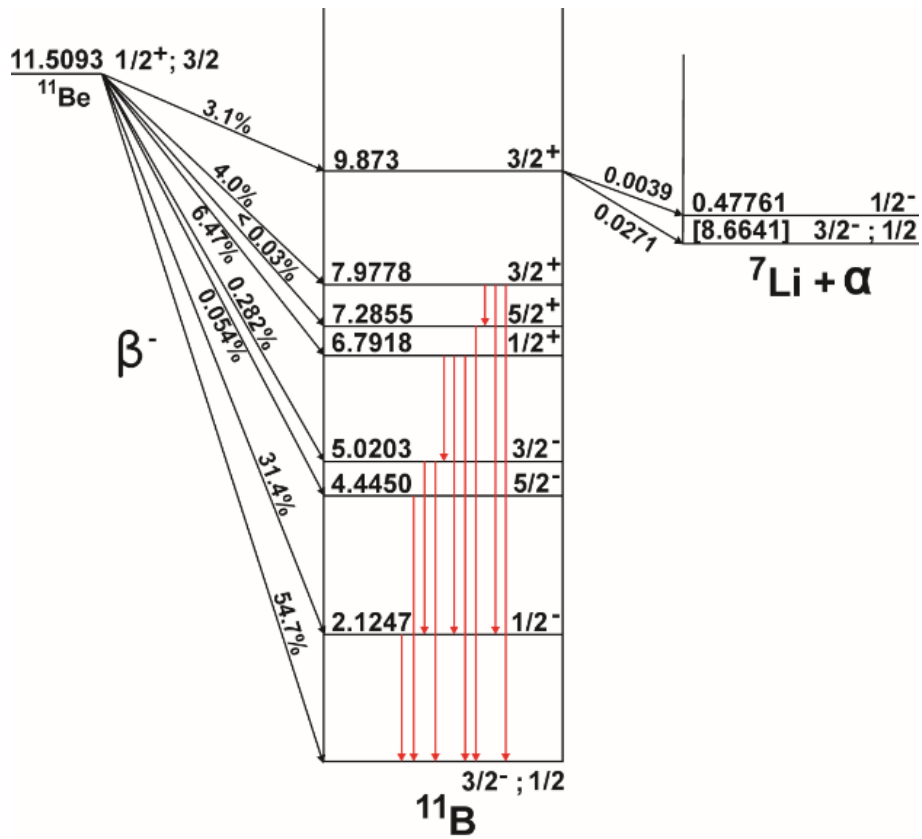


Figure 5.7 The decay channels of ^{11}Be ^[56].

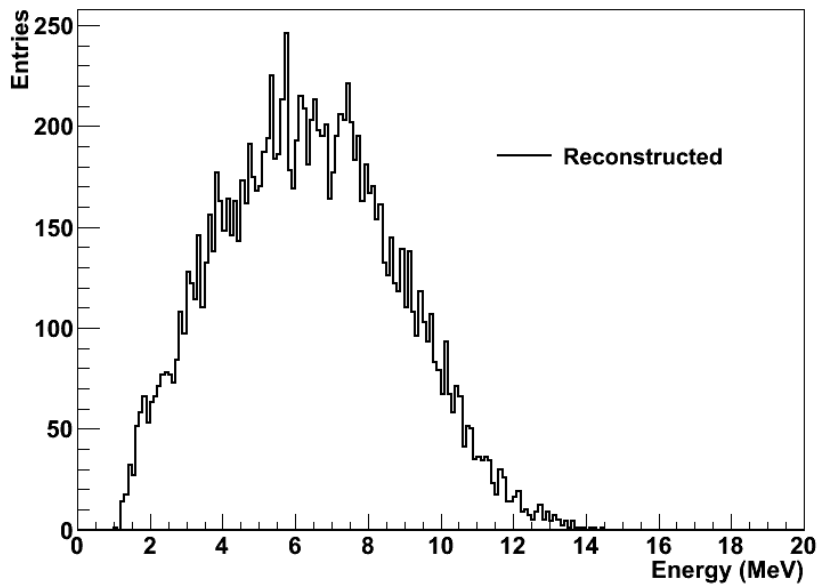


Figure 5.8 The distribution of the reconstructed energy from the β decay of ^{11}Be .

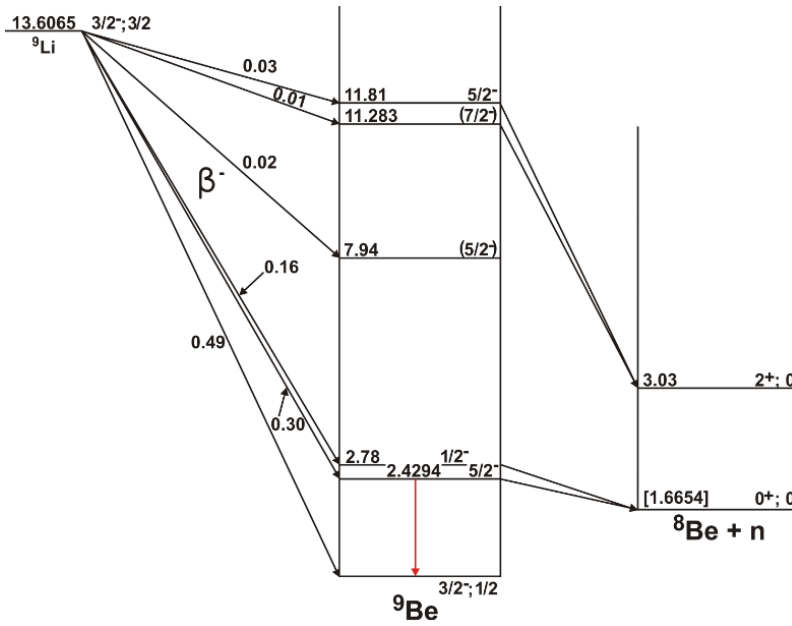


Figure 5.9 The decay channels of ${}^9\text{Li}$ ^[56].

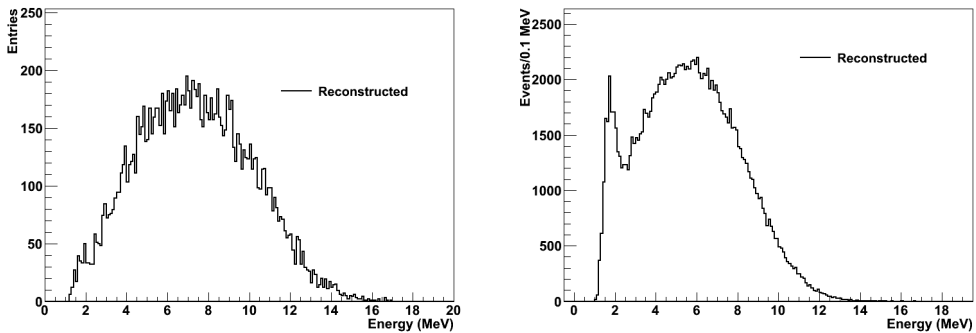


Figure 5.10 Left panel: the distribution of the reconstructed energy from the β decay of ${}^9\text{Li}$. Right panel: the distribution of the reconstructed energy from the βn decay of ${}^9\text{Li}$. The peak around 1.5 MeV in the right panel is due to the fact that 3% (1%) of ${}^9\text{Li}$ decays to ${}^9\text{B}$ on the energy level of 11.8 (11.3) MeV.

decay of ${}^8\text{He}$, respectively.

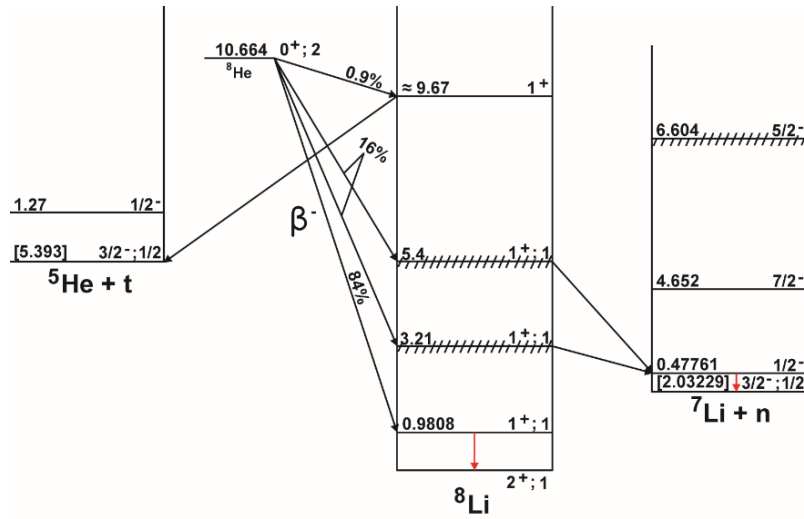


Figure 5.11 The decay channels of ${}^8\text{He}$ ^[56].

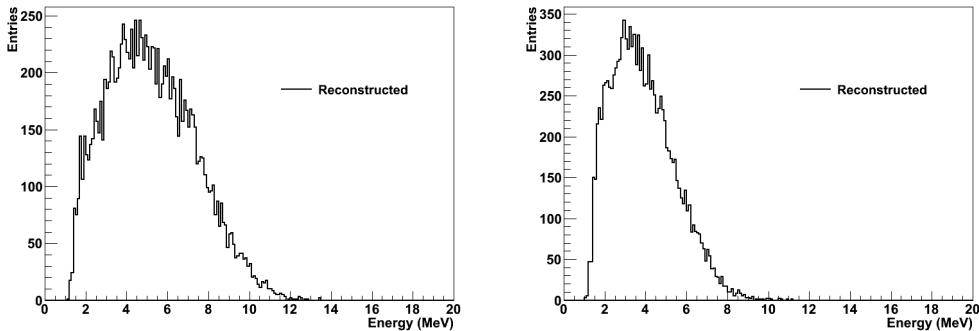


Figure 5.12 Left panel: the distribution of the reconstructed energy from the β decay of ${}^8\text{He}$. Right panel: the distribution of the reconstructed energy from the βn decay of ${}^8\text{He}$.

5.2.7 ${}^9\text{C}$ Decay

The ${}^9\text{C}$ decays with a Q-value of ~ 16.5 MeV and a τ of ~ 0.18 s. Fig. 5.13 shows the decay channels of ${}^9\text{C}$, which mainly goes through a β^+ decay to ${}^9\text{B}$ on the ground state with a BR of 54%. Another major channel of ${}^9\text{C}$ decays to ${}^9\text{B}$ on the energy of 2.3 MeV with a BR of $\sim 30\%$. Fig.5.14 shows the distribution of the reconstructed energy from the β decay of ${}^9\text{C}$.

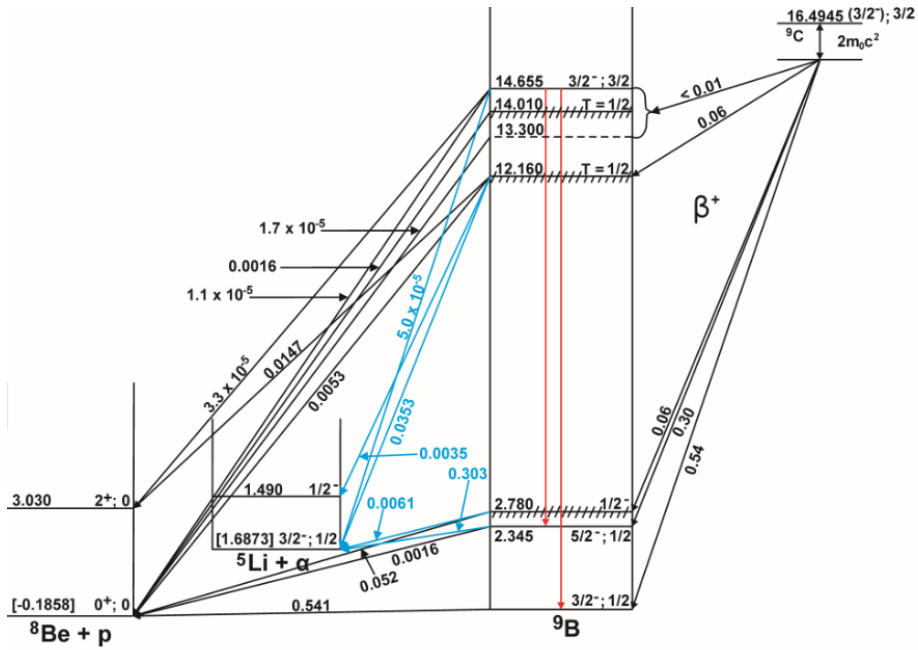


Figure 5.13 The decay channels of ${}^9\text{C}$ [56].

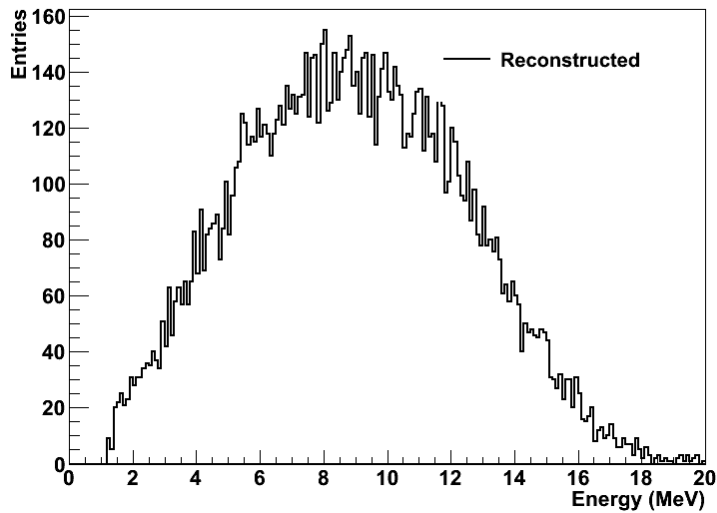


Figure 5.14 The distribution of the reconstructed energy from the β decay of ${}^9\text{C}$.

5.2.8 ${}^8\text{Li}$ Decay

The ${}^8\text{Li}$ decays with a Q-value of ~ 16.0 MeV and a τ of ~ 1.21 s. Fig. 5.15 shows the decay channels of ${}^8\text{Li}$, which mainly goes through a β^- decay to ${}^8\text{Be}$ on the energy level of 3.03 MeV. Fig.5.16 shows the distribution of the reconstructed energy from the β decay of ${}^8\text{Li}$.

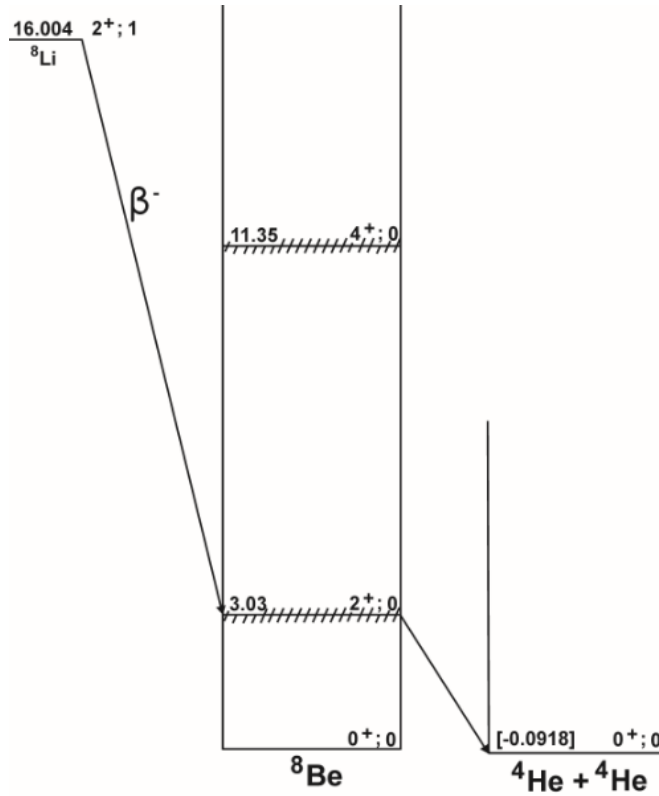


Figure 5.15 The decay channels of ${}^8\text{Li}$ ^[56].

5.2.9 ${}^{15}\text{C}$ Decay

The ${}^{15}\text{C}$ decays with a Q-value of ~ 9.8 MeV and a τ of ~ 3.53 s. Fig. 5.17 shows the decay channels of ${}^{15}\text{C}$, which mainly goes through a β^- decay to ${}^{15}\text{N}$ on the energy level of 5.3 MeV with a BR of $\sim 68\%$. Another major channel of ${}^{15}\text{C}$ decays to ${}^{15}\text{N}$ on the ground state with a BR of $\sim 32\%$. Fig.5.18 shows the distribution of the reconstructed energy from the β decay of ${}^{15}\text{C}$.

Table 5.1 lists the number fraction of events with energy above 8 (10) MeV for the βn decays from ${}^9\text{Li}$ and ${}^8\text{He}$.

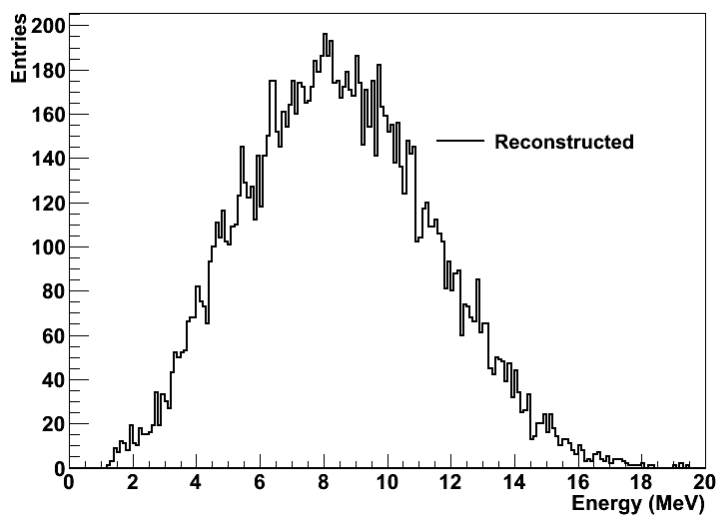


Figure 5.16 The distribution of the reconstructed energy from the β decay of ${}^8\text{Li}$.

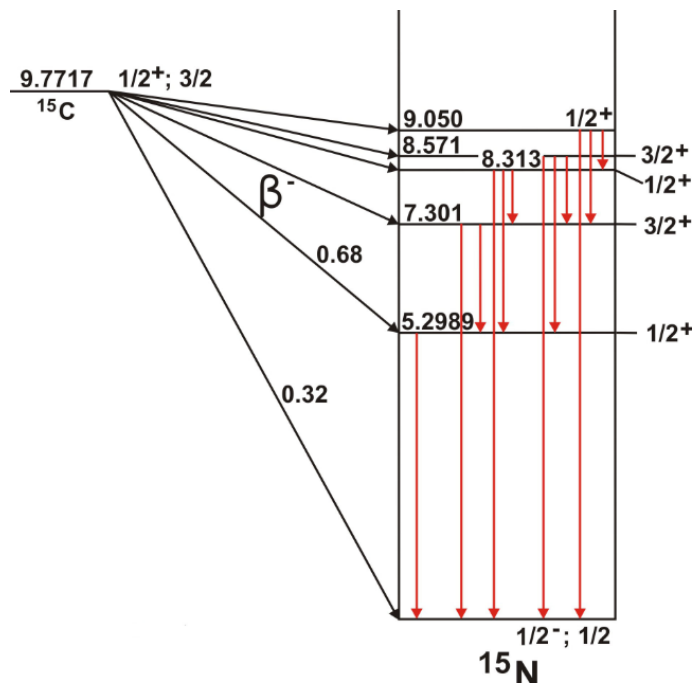


Figure 5.17 The decay channels of ${}^{15}\text{C}$ ^[56].

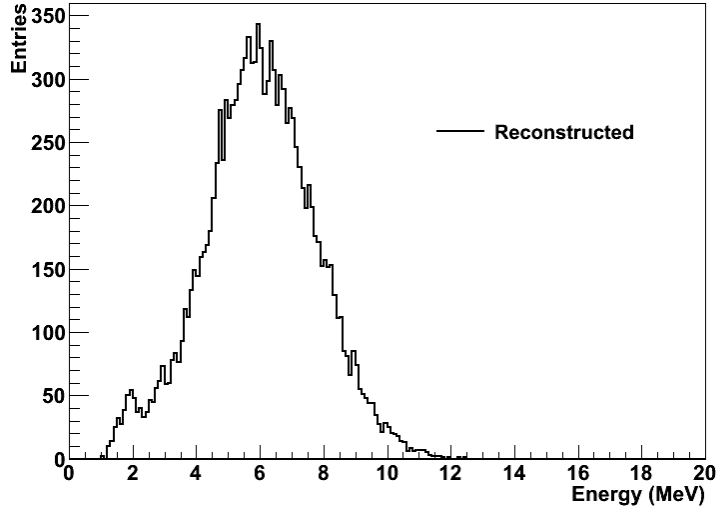


Figure 5.18 The distribution of the reconstructed energy from the β decay of ^{15}C .

Table 5.1 The expected number fraction of β events with energy above 8 (10) MeV from the βn decay mode of ^9Li and ^8He . Notice that the energy here is the total energy.

Isotope	fraction above 8 MeV	fraction above 10 MeV
^9Li	$(16.3 \pm 1.3)\%$	$(3.2 \pm 1.4)\%$
^8He	$<1.0\%$	$<0.1\%$

5.3 SRN

Fig.5.19 shows the positron energy spectrum using the LMA model. The cross section of the IBD reaction in Ref^[58] is used to obtain this spectrum. The detailed information about SRN simulation can be found in Ref^[59]. The expected number of SRN events in 10~30 MeV is ~ 5 events/year/22.5 kton. The energy of $\bar{\nu}_e$ is calculated by the following formula:

$$E_{\bar{\nu}_e} \simeq E_{e^+} + 1.3 \text{ MeV} \quad (5-1)$$

5.4 Atmospheric Neutrino Background

The remaining background from atmospheric neutrinos for the SRN analysis is estimated using NEUT. The major atmospheric neutrino background to the final SRN sample are ν_e CC, ν_μ CC and NC background. These backgrounds are described in

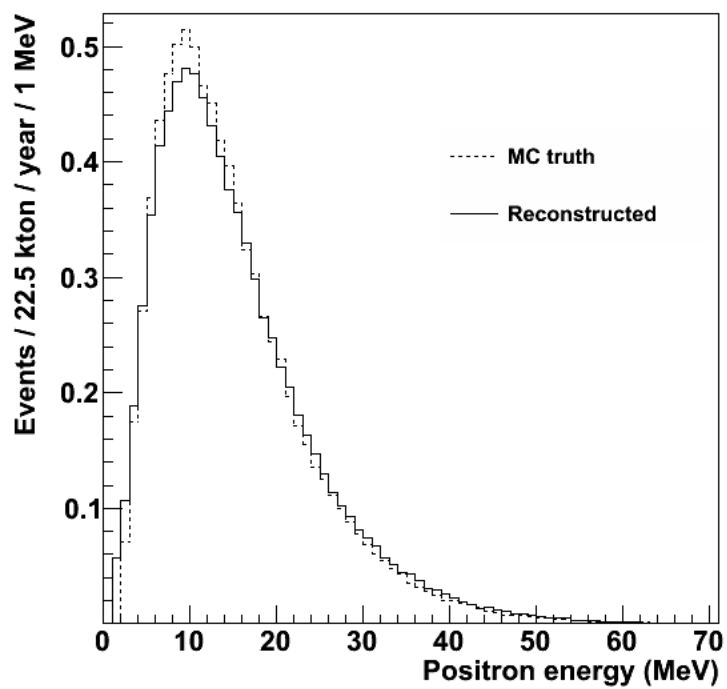


Figure 5.19 The positron spectrum using the LMA model.

Ref.^[48] in details.

Chapter 6 Neutron Tagging

Free neutrons from the IBD reaction can be thermalized quickly and then be captured by water. A water molecule consists of two hydrogen atoms and one oxygen atom. The cross section of neutron capture on hydrogen is ~ 0.33 bars, which is $\sim 1,700$ higher than that of neutron capture on oxygen (~ 0.19 mbars). So in this analysis, neutron is assumed to be $\sim 100\%$ captured by hydrogen with the reaction below:



The 2.2 MeV γ emitted from a neutron capture on hydrogen can be used to tag the neutron. The 2.2 MeV γ tagging method is also termed as neutron tagging. The neutron tagging method was first introduced to SK in 2005 for the purpose of SRN search^[60]. The SRN search results in 13.3 \sim 31.3 MeV with the neutron tagging were published in Ref^[13]. The neutron tagging efficiency is $\sim 20\%$ with the accidental background of $\sim 1\%$ in Ref^[13].

This chapter will describe the selection criteria of 2.2 MeV γ 's, the effort on improving the neutron tagging, the demonstration of neutron tagging method with an Am/Be source, the application of neutron tagging for atmospheric neutrino and solar neutrino events, respectively. At the end of the chapter, we will discuss the possible improvement of neutron tagging method in future.

6.1 Discriminating Variables for 2.2 MeV γ Events

The mean free path length of a thermal neutron is ~ 50 cm in water, while the vertex resolution of a 10 MeV electron/positron is ~ 55 cm^[61]. As an approximation, the vertex of the primary electron/positron is applied as the vertex of the 2.2 MeV γ .

The MC simulated sample of 2.2 MeV γ 's is obtained from the SKDETSIM (see Section 5.1), in which the dark noise is embedded using a random trigger data that is periodically collected to monitor the dark noise level and the low energy radioactivities. The background sample is obtained using the random trigger data. Several discriminating variables are developed and used as inputs in Multivariate Analysis (TMVA)^[62] in ROOT^[63] to differentiate the 2.2 MeV γ from the noise background.

6.1.1 N_{10}

A 2.2 MeV γ can fire ~ 8 PMT hits on average. About 90% of these PMT hits can cluster in a 10 ns time window after the time-of-flight subtraction. While for noise hits, the number of average PMT hits in the 10 ns time window is ~ 0.5 . However, the number of PMT hits in the 10 ns time window (N_{10}) for the background tends to have a large tail. N_{10} is used to select the 2.2 MeV γ signal from the background as the first step.

Fig. 6.1 shows the distribution of N_{10} for 2.2 MeV γ signal and the background. The background utilizes a data package with a time length of 500 μ s. With the increase of time length, the number of timing peaks per event for the background increases proportionately.

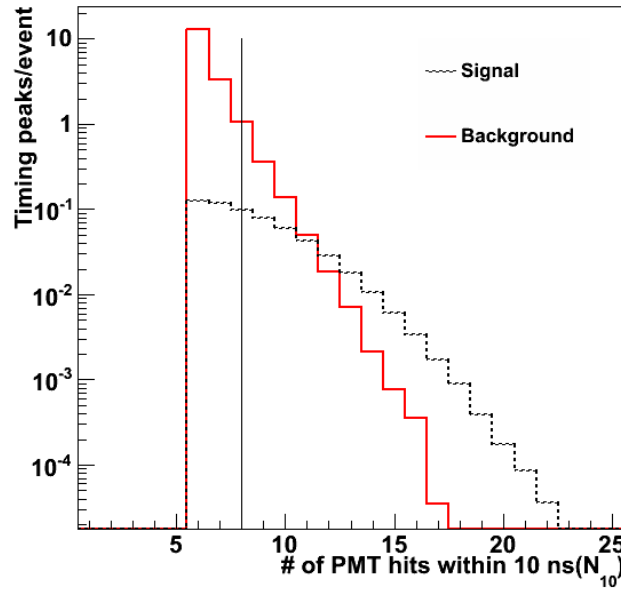


Figure 6.1 Distributions of N_{10} for the 2.2 MeV γ signal (black) and the background (red). $N_{10} \geq 6$ is applied.

N_{10} is required to be greater than 7 to remove majority of the background. After N_{10} pre-selection, the remaining timing peaks for 2.2 MeV γ signal are ~ 0.35 per event, while the remaining timing peaks for background are ~ 1.6 per event.

Fig. 6.2 shows the distribution of N_{10} after N_{10} pre-selection, which can still be used as the input in TMVA.

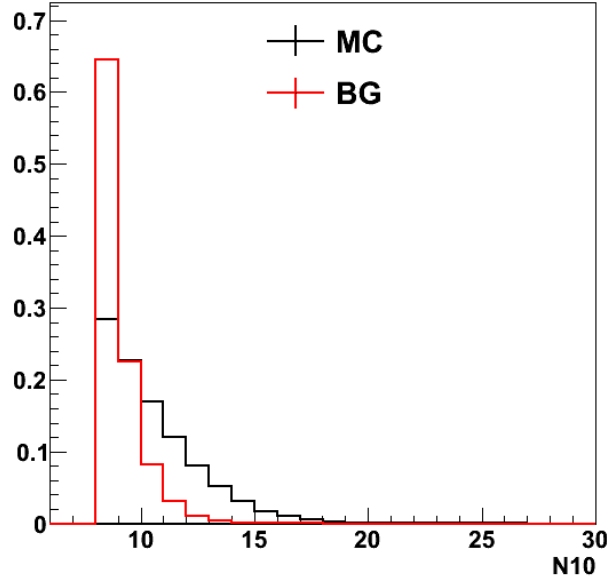


Figure 6.2 Distributions of N_{10} for the 2.2 MeV γ signal (black) and the background (red) after the N_{10} pre-selection. The distributions are scaled to unity.

6.1.2 $N_{cluster}$

Large amount of background (e.g., the radioactivities from the surrounding rock and PMT FRP case etc.) originating from the neighbor of the detector wall can cluster both in space and time. Thus, such kind of background can escape the N_{10} cut. An angle α is defined as the angle between any two hit vectors (from the vertex of 2.2 MeV γ to the vertex of hit PMT). The number of PMT hits with the α lower than 14.1° is referred to as $N_{cluster}$. Fig. 6.3 shows the distribution of $N_{10}-N_{cluster}$.

6.1.3 N_{back}

A Compton electron scattered by a 2.2 MeV γ emits Cherenkov light in the forward direction, while the noise hits tend to be uniformly distributed in the detector. An angle β is defined as the angle between the hit vector and the sum of the all hit vectors in a 10 ns time window. The number of PMT hits with $\beta > 90^\circ$ is referred to as N_{back} . Fig. 6.4 shows the distribution of $N_{10}-N_{back}$.

6.1.4 N_{low}

For Cherenkov light emitted from a given vertex, PMTs closer to the vertex are easier to be hit due to the attenuation of Cherenkov light in water. While for noise hits,

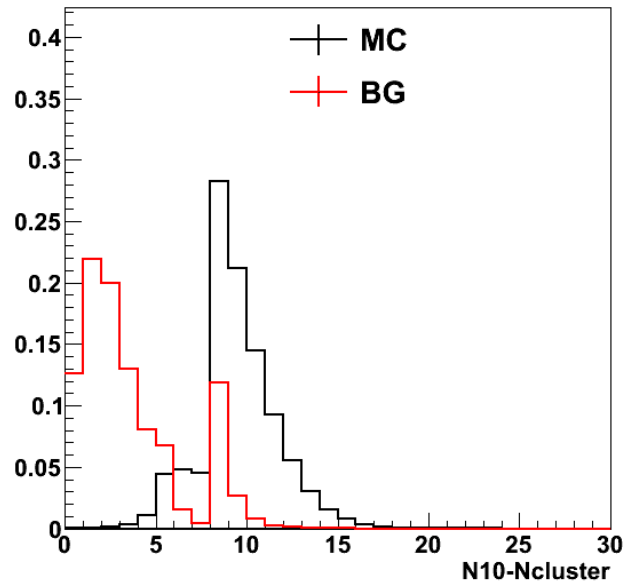


Figure 6.3 Distributions of $N_{10} - N_{cluster}$ for the 2.2 MeV γ signal (black) and the background (red) after the N_{10} pre-selection. The distributions are scaled to unity.

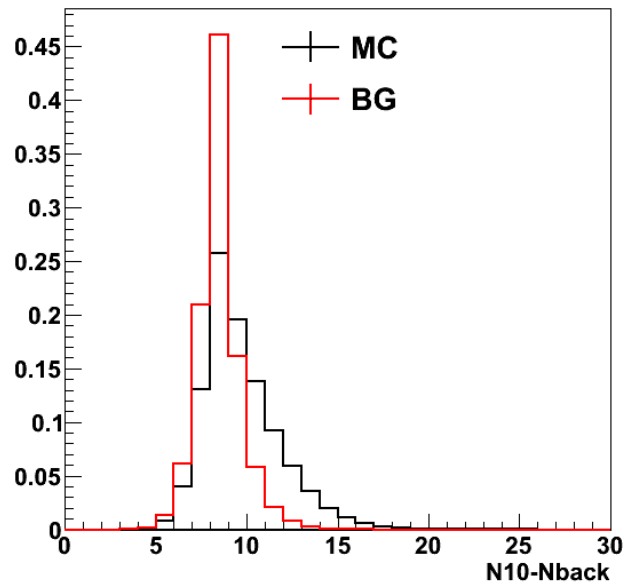


Figure 6.4 Distributions of $N_{10} - N_{back}$ for the 2.2 MeV γ signal (black) and the background (red) after the N_{10} pre-selection. The distributions are scaled to unity.

the hit probability is independent with the given vertex. The hit probability P_i of i -th PMT is described with the following formula:

$$P_i \propto \frac{(\cos \theta_i)_{eff}}{R_i^2} e^{-R_i/L_{atten}} \quad (6-2)$$

where $(\cos \theta_i)_{eff} = 0.205 + 0.523 \cos \theta_i + 0.389 \cos^2 \theta_i - 0.131 \cos^3 \theta_i$, R_i is the distance from the vertex of the 2.2 MeV γ to the vertex of the i -th hit PMT and L_{atten} is attenuation length of light in SK water.

The hit probability P_i is calculated for all the 11,129 PMTs. These probabilities are sorted with a decreasing order. The lower 20%~30% part PMTs are defined to be the PMTs with low hit probability. The number of PMTs with low hit probability in the 10 ns time window is referred to as N_{low} . Fig. 6.5 shows the distribution of $N_{10}-N_{low}$.

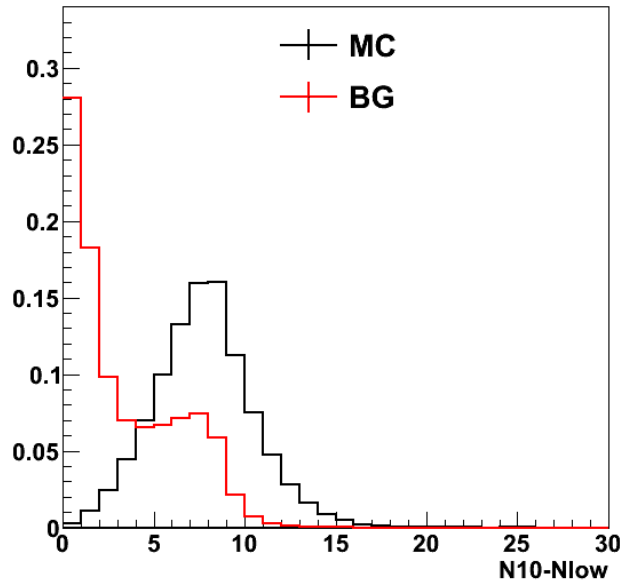


Figure 6.5 Distributions of $N_{10}-N_{low}$ for the 2.2 MeV γ signal (black) and the background (red) after the N_{10} pre-selection. The distributions are scaled to unity.

6.1.5 N_{300}

For some background, parts of PMT hits can cluster in a 10 ns time window, while the remaining PMT hits are out of the time window. In order to remove this background, the number of PMT hits ± 150 ns (N_{300}) around the timing peak of N_{10} is calculated. Fig. 6.6 shows the distribution of $N_{300}-N_{10}$.

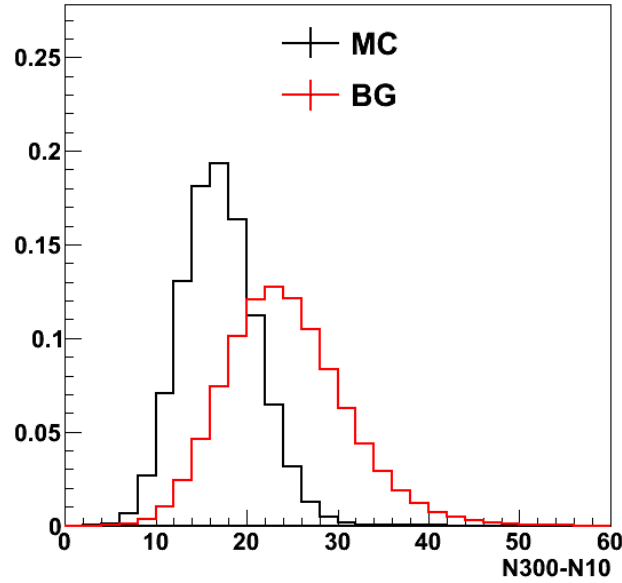


Figure 6.6 Distributions of $N_{300} - N_{10}$ for the 2.2 MeV γ signal (black) and the background (red) after the N_{10} pre-selection. The distributions are scaled to unity.

6.1.6 T_{rms}

The distribution of PMT hit timings of the 2.2 MeV γ is narrower than that of the background events. The root mean square of PMT hit timings (T_{rms}) is calculated. Fig. 6.7 shows the distribution of T_{rms} .

6.1.7 ϕ_{rms}

The distribution of azimuth angle difference between any two neighbor hit vectors for the 2.2 MeV γ signal tend to be narrower than the background events. The root mean square of azimuth angle difference (ϕ_{rms}) is calculated. Fig. 6.8 shows the distribution of ϕ_{rms} .

6.1.8 $\theta_{mean}, \theta_{rms}$

θ_{mean} is the mean value of the angles between the hit vector and the sum of the hit vectors. The θ_{mean} for Compton electron peaks around 42° , while noise hits cluster in space and time tend to have smaller θ_{mean} . The left panel of Fig. 6.9 shows the distribution of θ_{mean} . θ_{rms} is the root mean square value of the angles between the hit vector and the sum of the hit vectors. The right panel of Fig. 6.9 shows the distribution of θ_{rms} .

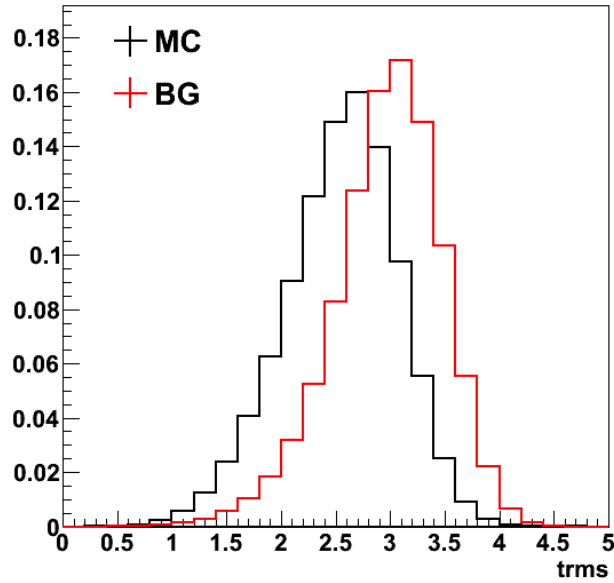


Figure 6.7 Distributions of T_{rms} for the 2.2 MeV γ signal (black) and the background (red) after the N_{10} pre-selection. The distributions are scaled to unity.

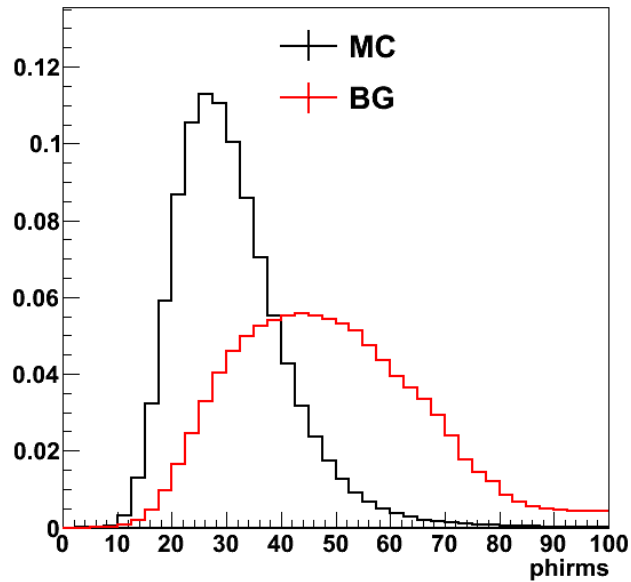


Figure 6.8 Distributions of ϕ_{rms} for the 2.2 MeV γ signal (black) and the background (red) after the N_{10} pre-selection. The distributions are scaled to unity.

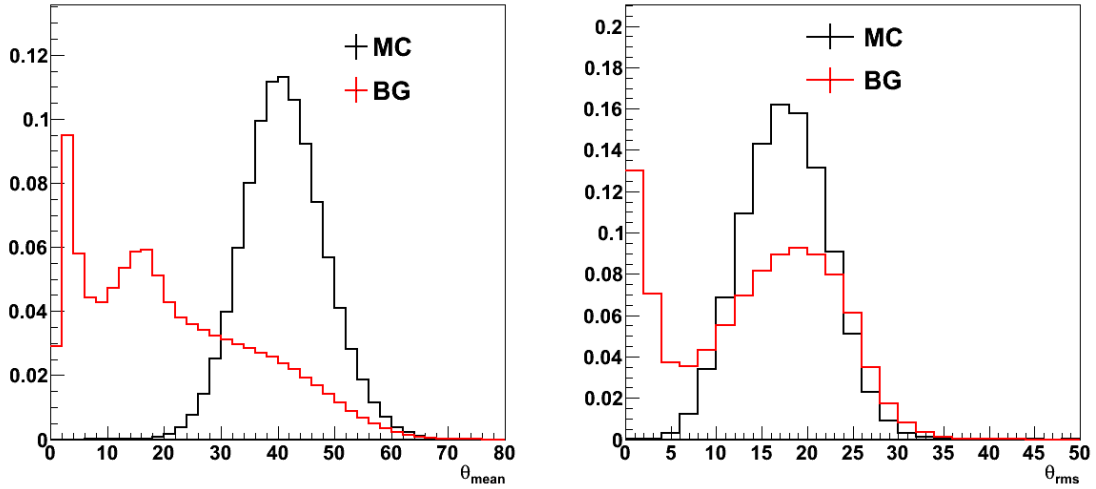


Figure 6.9 Distributions of θ_{mean} (left panel) and θ_{rms} (right panel) for the 2.2 MeV γ signal (black) and the background (red) after the N_{10} pre-selection. The distributions are scaled to unity.

6.1.9 $N_{LowTheta}$

The number of PMT hits with the angle between the hit vector and the sum of the hit vectors lower than 20° is referred to as $N_{LowTheta}$. Fig. 6.10 shows the distribution of $N_{10}-N_{LowTheta}$.

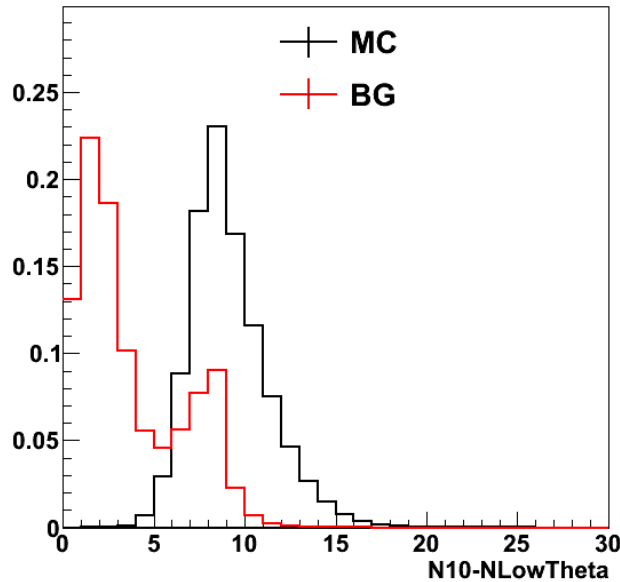


Figure 6.10 Distributions of $N_{10}-N_{LowTheta}$ for the 2.2 MeV γ signal (black) and the background (red) after the N_{10} pre-selection. The distributions are scaled to unity.

6.1.10 Q_{mean} , Q_{rms}

Q_{mean} is the mean value of number of p.e.s in a 10 ns time window. The left panel of Fig. 6.11 shows the distribution of Q_{mean} . Q_{rms} is the root mean square value of number of p.e.s in the 10 ns time window. The right panel of Fig. 6.11 shows the distribution of Q_{rms} .

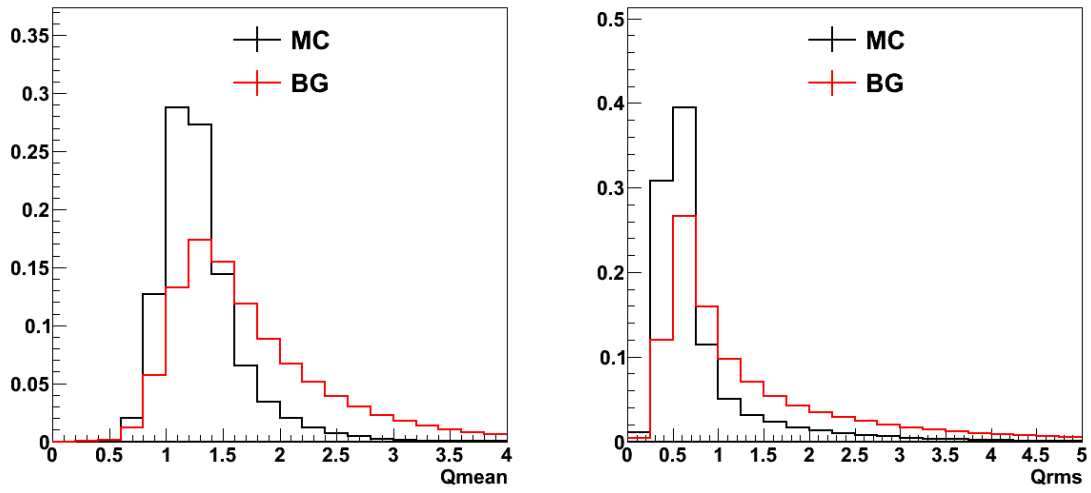


Figure 6.11 Distributions of Q_{mean} (left panel) and Q_{rms} (right panel) for the 2.2 MeV γ signal (black) and the background (red) after the N_{10} pre-selection. The distributions are scaled to unity.

6.1.11 N_{highQ}

The number of PMT hits with more than 3. p.e.s in a 10 ns time window is referred to as N_{highQ} . Fig. 6.12 shows the distribution of $N_{10}-N_{highQ}$.

6.2 TMVA Output

The 13 discriminating variables described above are used as the inputs of TMVA using the Multiple-Layer-Perceptron (MLP) choice in ROOT. Fig. 6.13 shows the distribution of the output of MLP.

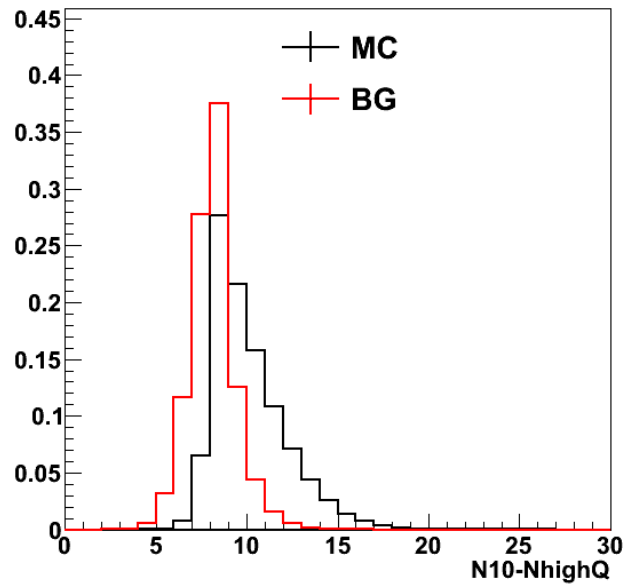


Figure 6.12 Distributions of $N_{10} - N_{highQ}$ for the 2.2 MeV γ signal (black) and the background (red) after the N_{10} pre-selection. The distributions are scaled to unity.

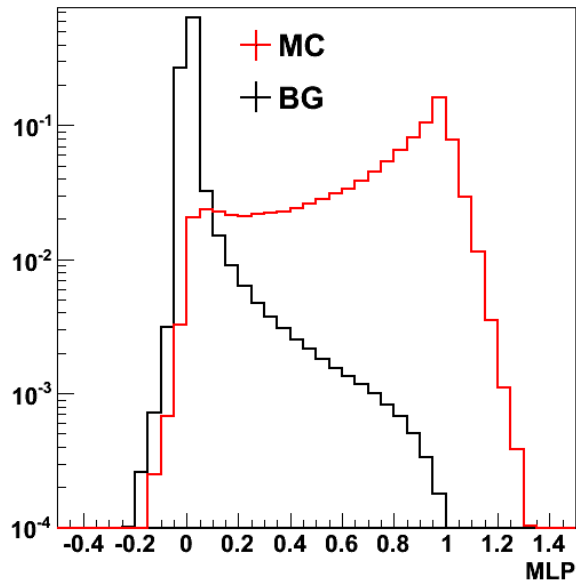


Figure 6.13 Distributions of the output of MLP for the 2.2 MeV γ signal (black) and the background (red). The distributions are scaled to unity.

6.3 Determination of Efficiency

6.3.1 Efficiency for the SRN Search $E_{\bar{\nu}_e} < 14.3$ MeV

Since the spallation background increases rapidly below 14.3 MeV, a tighten cut of neutron tagging is applied. The neutron tagging efficiency and the accidental background level is defined with the formulas in Eqn. 6-3 and Eqn. 6-4, respectively:

$$\text{Neutron tagging efficiency} = \frac{\text{the number of remaining timing peaks}}{\text{the number of total 2.2 MeV gamma events}} \quad (6-3)$$

$$\text{Accidental background level} = \frac{\text{the number of remaining timing peaks in } 500 \mu\text{s}}{\text{the number of total random trigger events}} \quad (6-4)$$

To set the MLP cut appropriately, the significance is defined with the following formula:

$$\text{significance} = \frac{s}{\sqrt{b}} \quad (6-5)$$

where the s represents the 2.2 MeV γ signal efficiency, and b represents the accidental background level. The left panel of Fig. 6.14 shows the 2.2 MeV γ signal efficiency as a function of the accidental background level. The right panel of Fig. 6.14 shows the significance as a function of 2.2 MeV gamma signal efficiency.

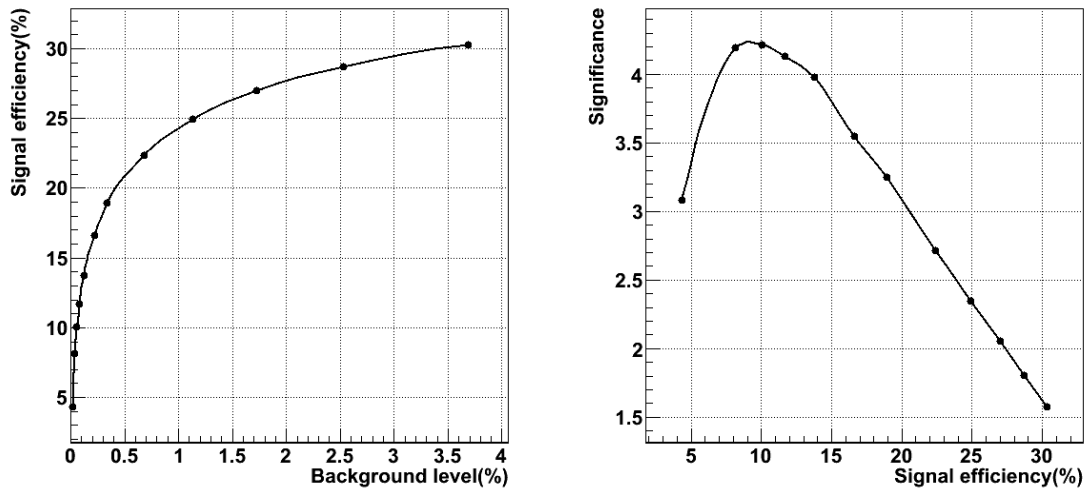


Figure 6.14 Left panel: The 2.2 MeV γ signal efficiency (vertical axis) as a function of the accidental background level (horizontal axis); Right panel: The significance as a function of the 2.2 MeV γ signal efficiency.

The significance is maximized when the signal efficiency is $\sim 10\%$, while the corresponding accidental background level is $\sim 0.065\%$. In order to make the signal efficiency and the accidental background level uniform in the tank, the MLP cut is applied with a position dependence. The more closer to the tank wall, the more stringent cut is applied since more low energy backgrounds are close to the wall of the tank. Fig. 6.15 shows the schematic view of the MLP cut. The tank is virtually divided into 10×11 cells in the $R^2 - z$ panel. The signal efficiency and the accidental background level is calculated for each cell. Fig. 6.16 shows the variation of the signal efficiency and the accidental background level in the tank.

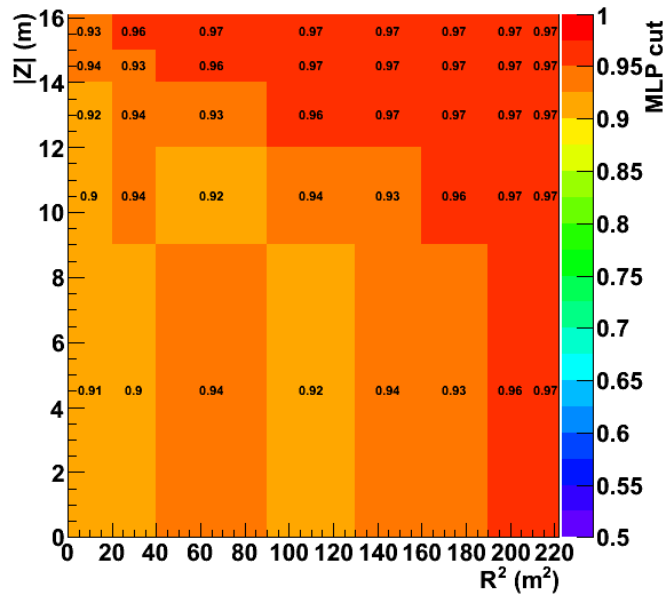


Figure 6.15 MLP cut with a position dependence.

Table 6.1 lists the 2.2 MeV γ signal efficiency and the accidental background level after each cut. Both the signal sample and the background sample are very large, thus, the statistical uncertainty of signal efficiency ($\sim 0.2\%$ relative) and the accidental background level ($\sim 1.3\%$ relative) are very small compared with the systematic uncertainties described later. Fig. 6.17 shows the distribution of time for the noise background mis-tagged as neutrons by the neutron tagging method. The distribution is flat, which is used to model the time distribution of the accidental background.

Random trigger data have been taken since the beginning of SK-IV. Fig. 6.18 shows the accidental background level with the time variation during the whole period of SK-IV. The red solid line represents the mean value, while the upper dashed line and lower

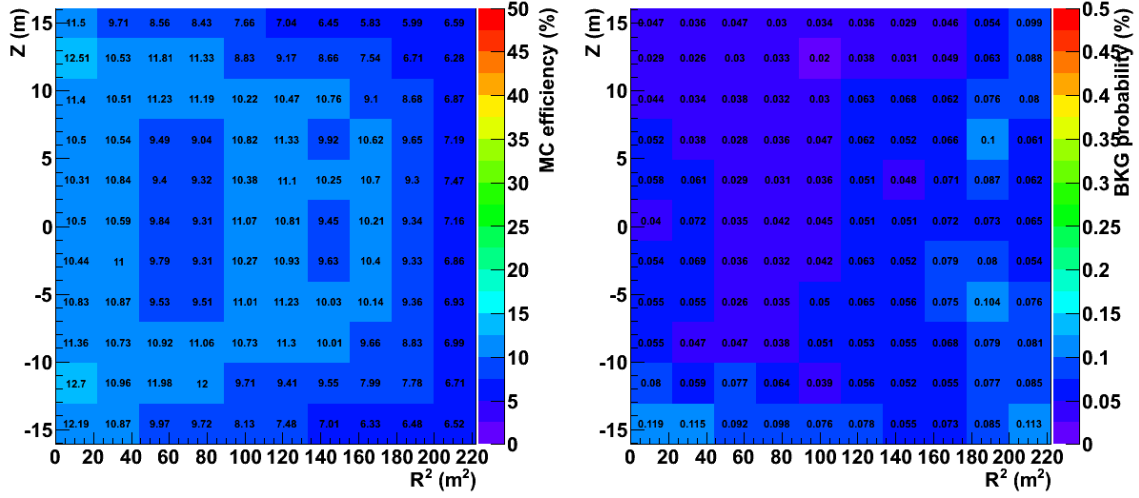


Figure 6.16 The variation of the signal efficiency (left) and the accidental background level (right) in the tank.

Table 6.1 Summary of the 2.2 MeV γ signal efficiency and the accidental background level after each cut.

Cut	Signal (MC)/event	Background (500 μ s)/event
$N_{10} > 7$	35.0%	160.1%
MLP cut	10.2%	0.065%

dashed line represent the maximum value and the minimum value, respectively. The relative systematic uncertainty of the accidental background level is estimated to be $\sim 23.1\%$. The accidental background level is $(0.065 \pm 0.015)\%$. The study shows that the decreasing accidental background level with the elapse time is due to both the slightly increasing dark noise level and the PMT gain. Increasing the dark noise from 4.6 kHz to 5.0 kHz causes no change to N_{10} distribution. However, this can shift the distribution of $N_{300}-N_{10}$ by +1.2, which can reduce the accidental background level (background events tend to have a larger $N_{300}-N_{10}$). Similarly, the increasing 2% PMT gain per year can have a slightly decrease in the final accidental background level.

6.3.2 Efficiency for the SRN Search $E_{\bar{\nu}_e} > 14.3$ MeV

The background suppression of $\sim 0.065\%$ is rather powerful with the loss of the signal efficiency. In the SRN search above 14.3 MeV, the 0.065% accidental background

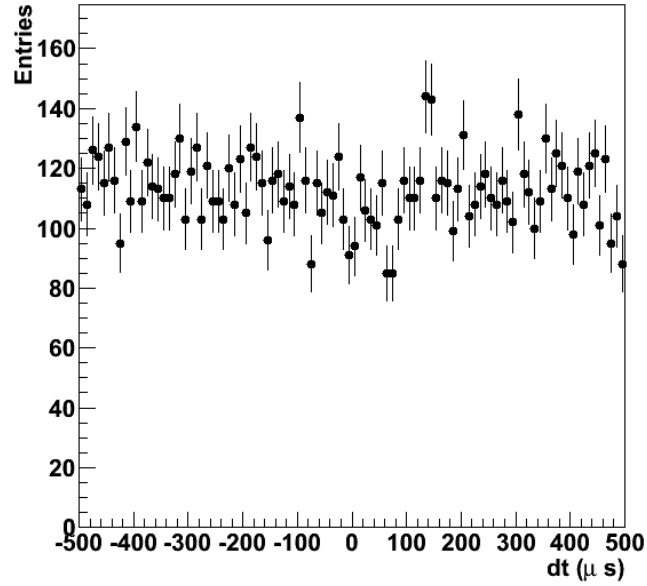


Figure 6.17 The distribution of time for the noise background mis-tagged as neutrons by the neutron tagging method.

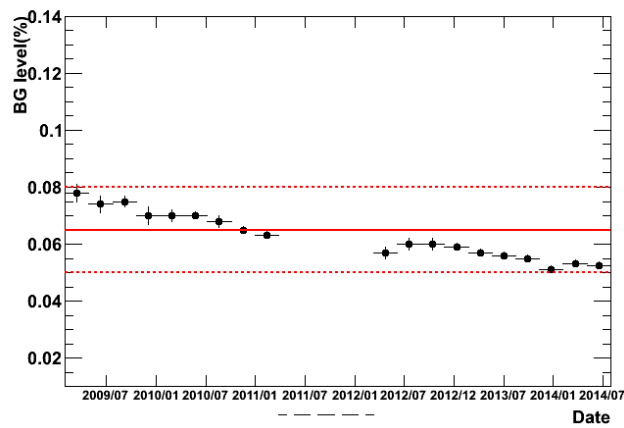


Figure 6.18 Time variation of the accidental background level in all the SK-IV periods. The vacancy around the year 2011 is due to the earthquake in Japan.

level is not necessary. The MLP cut is loosen to have a $\sim 18\%$ efficiency with a $\sim 0.3\%$ accidental background level. Fig. 6.19 shows the MLP cut with a position dependence, which is applied in the similar fashion as the subsection 6.3.1. Table 6.2 lists the 2.2 MeV γ signal efficiency and the accidental background level after each cut. Fig. 6.20 shows the signal efficiency and the accidental background level with the position variation in the tank. Fig. 6.21 shows the time variation of the accidental background level during the SK-IV period.

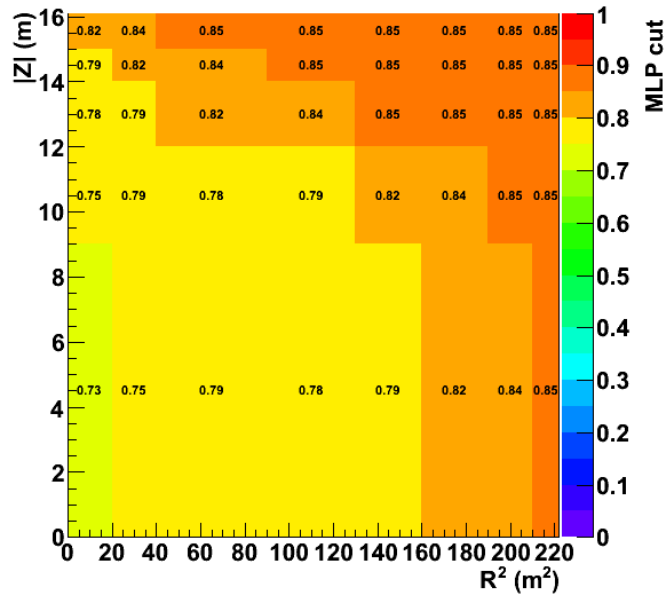


Figure 6.19 MLP cut with a position dependence for the loose cut.

Table 6.2 Summary of the 2.2 MeV γ signal efficiency and the accidental background level after each cut for the loose cut.

Cut	Signal (MC)/event	Background (500 μ s)/event
$N_{10} > 7$	35.0%	160.1%
MLP cut	18.1%	0.3%

6.3.3 Comparison with the Previous Neutron Tagging

The neutron tagging method is improved with a better signal-to-noise ratio compared with the previous version in^[59]. Table 6.3 lists the efficiencies of neutron tagging

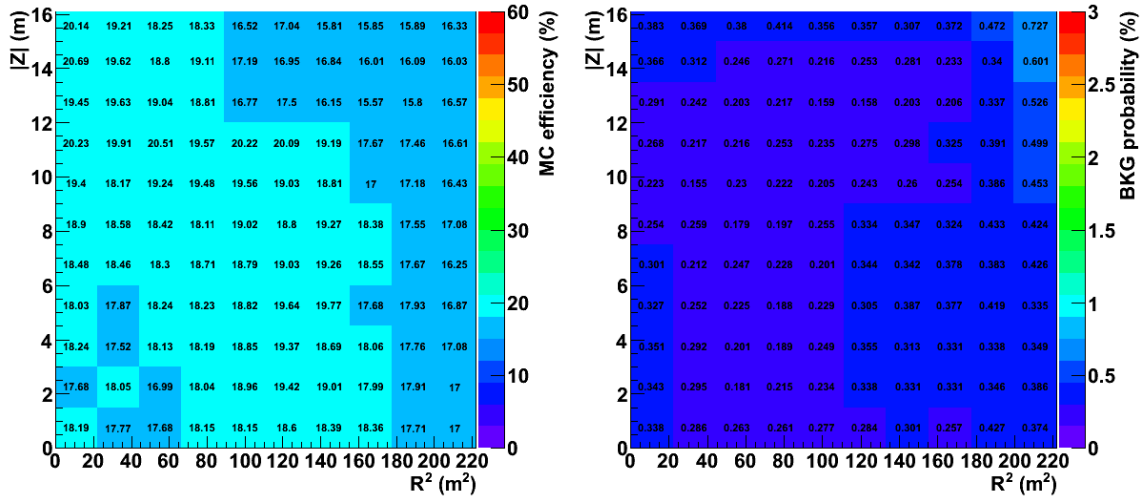


Figure 6.20 The signal efficiency (left) and the accidental background level(right) with position variation in the tank for the loose cut.

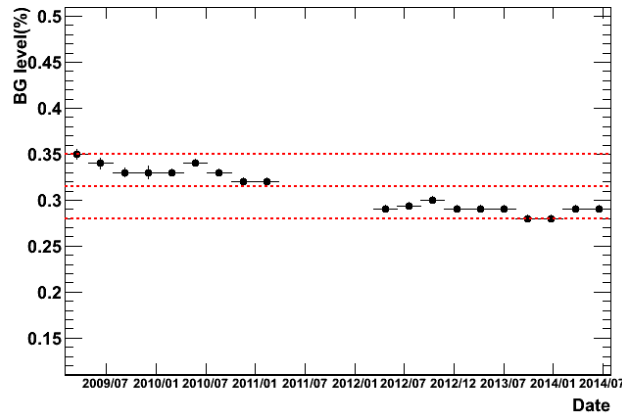


Figure 6.21 Time variation of the accidental background level in all the SK-IV periods for the loose cut. The vacancy around the year 2011 is due to the earthquake in Japan.

applied in $E_{\bar{\nu}_e}$ lower and greater than 14.3 MeV, respectively, together with the previous version. Using the similar neutron tagging efficiency (18.1% compared with 19.3%), the accidental background level is reduced by a factor of ~ 3 . Using the efficiency with the loose cut, the accidental background level is reduced by a factor of ~ 16 with the neutron tagging efficiency only reduced by a factor of ~ 2 .

Table 6.3 Comparison of the efficiency with the previous version in^[59].

neutron tagging version	Signal (MC)/event	Background (500 μ s)/event
$E_{\bar{\nu}_e} < 14.3$ MeV	10.2%	0.065%
$E_{\bar{\nu}_e} > 14.3$ MeV	18.1%	0.3%
previous version	19.3%	1.0%

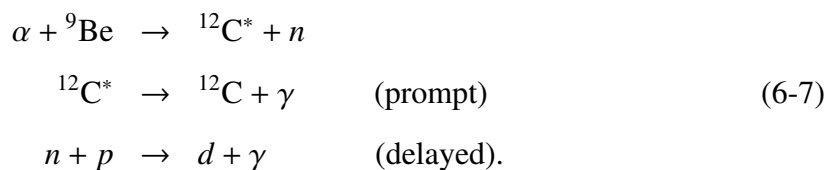
6.4 Study of Systematic Uncertainty on Neutron Tagging Efficiency

An Am/Be source was used in order to study the systematic uncertainty on the neutron tagging efficiency. During the data taking with Am/Be source in SK-IV, the AFT trigger was temporally enlarged to 800 μ s in order to cover a more complete neutron lifetime in water.

6.4.1 Experimental Setup

The experimental setup can be found in Ref^[64]. The Am/Be source was deployed at the center of 8-piece bismuth germanate oxide (BGO), which was held together with an acrylic case. Fig 6.22 shows a photo of the configuration of Am/Be source. The reaction chain of neutron production are as follows:

α particles come from the decay of ^{241}Am



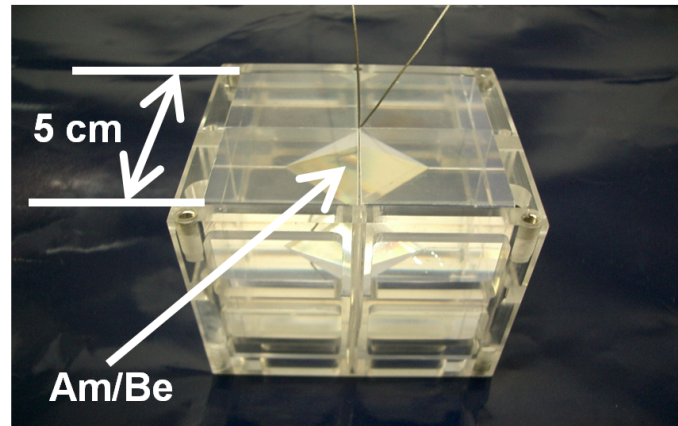


Figure 6.22 A photo of the configuration of Am/Be source.

The prompt 4.43 MeV γ from the de-excitation of $^{12}\text{C}^*$ (~ 87 Hz) can issue a SHE trigger with the light amplification of BGO, while the delayed 2.2 MeV γ can be recorded by the following AFT trigger. Notice that the ground state ^{12}C also exists with ~ 76 Hz, where no prompt 4.43 MeV γ exists. In this case, the delayed neutrons are background since there is no time correlation.

The Am/Be sources were deployed into the tank at 3 different locations to study the position dependence of neutron tagging efficiency. Table 6.4 lists the detailed positions of the sources. During the data taking with source A, a 10 Hz random trigger data was also taken to evaluate both the source related and the accidental background levels.

Table 6.4 The position of Am/Be source A, B, C.

Am/Be source	X position(cm)	Y position(cm)	Z position(cm)
A	35.3	-70.7	0.
B	35.3	-1201.9	0.
C	35.3	-70.7	1500.

6.4.2 Test on the neutron tagging cut for $E_{\bar{\nu}_e} < 14.3$ MeV

The Am/Be source data selection can be separated into two parts, the SHE trigger events and AFT trigger events. The procedures of events selection are as follows:

1. $750 < \text{total p.e.} < 1,050$ is required to select the prompt events for source A
 $850 < \text{total p.e.} < 1,150$ for source B and $900 < \text{total p.e.} < 1,150$ for source C.

2. the time difference between any two neighbor events is required to be greater than 1.5 ms to avoid the events overlap.
3. the maximum PMT hits in 200 ns (N200M) is required to be lower than 50 to avoid large events such as cosmic ray muons.

The upper panel of Fig. 6.23 shows the distribution of time for the observed neutron candidates using the random trigger data. Although delayed neutrons with no prompt signal exist, the exponential feature is smeared since there is no time correlation with the SHE trigger events. The ΔT distribution is flat, which is fit by a constant term with a $\chi^2/\text{ndf}=24.2/25$. The bottom left panel of Fig. 6.23 shows the ΔT distribution for source A, which is fit with an exponential form plus a fixed constant term. The bottom right panel of Fig. 6.23 shows the ΔT distribution for source A, which is fit with an exponential term plus a free constant term. Both fits show that the measured life times of neutron in water are consistent with $204.8 \mu\text{s}$ given in^[65]. The statistical uncertainty of life time from free background fit is larger than that of the fixed one due to one more fit parameter. The neutron tagging efficiency is calculated with the following formula:

$$\epsilon = \frac{\text{the number of neutron events from fit}}{\text{the number of total prompt events}} \quad (6-8)$$

Both the neutron tagging efficiency and the life time of neutron from the MC and Am/Be source A are listed in Table 6.5.

Table 6.5 Comparison between the MC and the Am/Be source A.

	MC	fit with BG fixed	fit with BG free
signal efficiency	$(10.5 \pm 0.3)\%$	$(10.9 \pm 0.2)\%$	$(10.9 \pm 0.2)\%$
τ	$\sim 200 \mu\text{s}$	$(202.0 \pm 3.3)\mu\text{s}$	$(202.8 \pm 4.8)\mu\text{s}$

For source B and C, no random trigger data is available. The left panel and the right panel of Fig. 6.24 show the ΔT distribution from source B and C, respectively. The statistical uncertainty of the fit life time is larger than that of source A due to the lower statistics. Both the neutron tagging efficiency and the life time of neutron from the MC and Am/Be source B, C are listed in Table 6.6 and Table 6.7, respectively. The combined neutron tagging efficiency from source A, B and C is $(11.4 \pm 0.2)\%$. The difference of signal efficiency between the MC and the Am/Be source is determined to

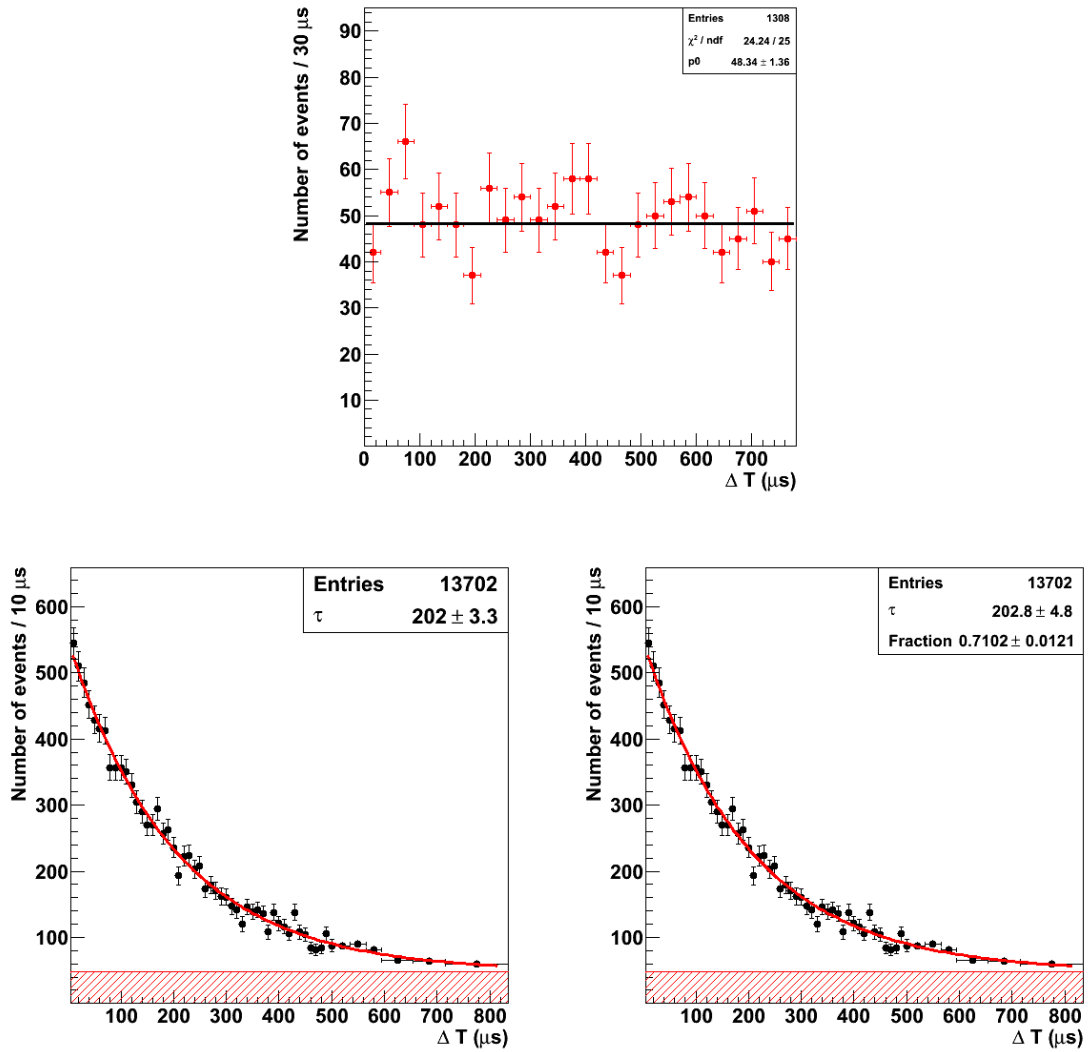


Figure 6.23 Upper panel: ΔT distribution from the random trigger data; Bottom left panel: ΔT distribution for source A which is fit with a fixed background level; Bottom right panel: ΔT distribution for source A which is fit with a free background level. The red shadow represents the expected background level.

Table 6.6 Comparison between the MC and the Am/Be source B.

	MC	fit with BG free
signal efficiency	$(10.5 \pm 0.3)\%$	$(12.9 \pm 0.4)\%$
τ	$\sim 200 \mu s$	$(201.3 \pm 8.0) \mu s$

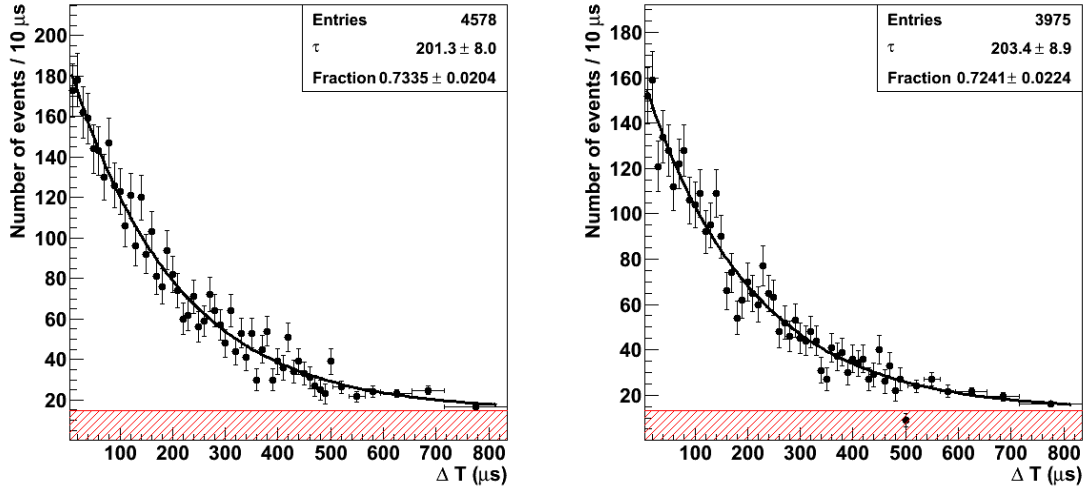


Figure 6.24 Left panel: ΔT distribution from source B which is fit with a free background level; Right panel: ΔT distribution from source C which is fit with a free background level. The red shadow represents the expected background level.

Table 6.7 Comparison between the MC and the Am/Be source C.

	MC	fit with BG free
signal efficiency	$(12.9 \pm 0.3)\%$	$(12.1 \pm 0.4)\%$
τ	$\sim 200 \mu s$	$(203.4 \pm 8.8)\mu s$

be the systematic uncertainty of the neutron tagging efficiency, which is estimated to be 10% in relative terms.

6.4.3 Test on the neutron tagging cut for $E_{\bar{\nu}_e} > 14.3 \text{ MeV}$

Fig. 6.25 shows the ΔT distribution from Am/Be source A. Both the tagging efficiency and the life time of neutron from the MC and the Am/Be source A are listed in Table 6.8. Fig. 6.26 shows the ΔT distribution from source B and C, respectively. Both the neutron tagging efficiency and the life time of neutron from the MC and Am/Be source B, C are listed Table 6.9 and Table 6.10, respectively. The combined neutron tagging efficiency from source A, B and C is $(18.5 \pm 0.2)\%$. The difference of signal efficiency between the MC and the Am/Be source data is assigned as the systematic uncertainty for the neutron tagging efficiency, giving 2.4% in relative terms.

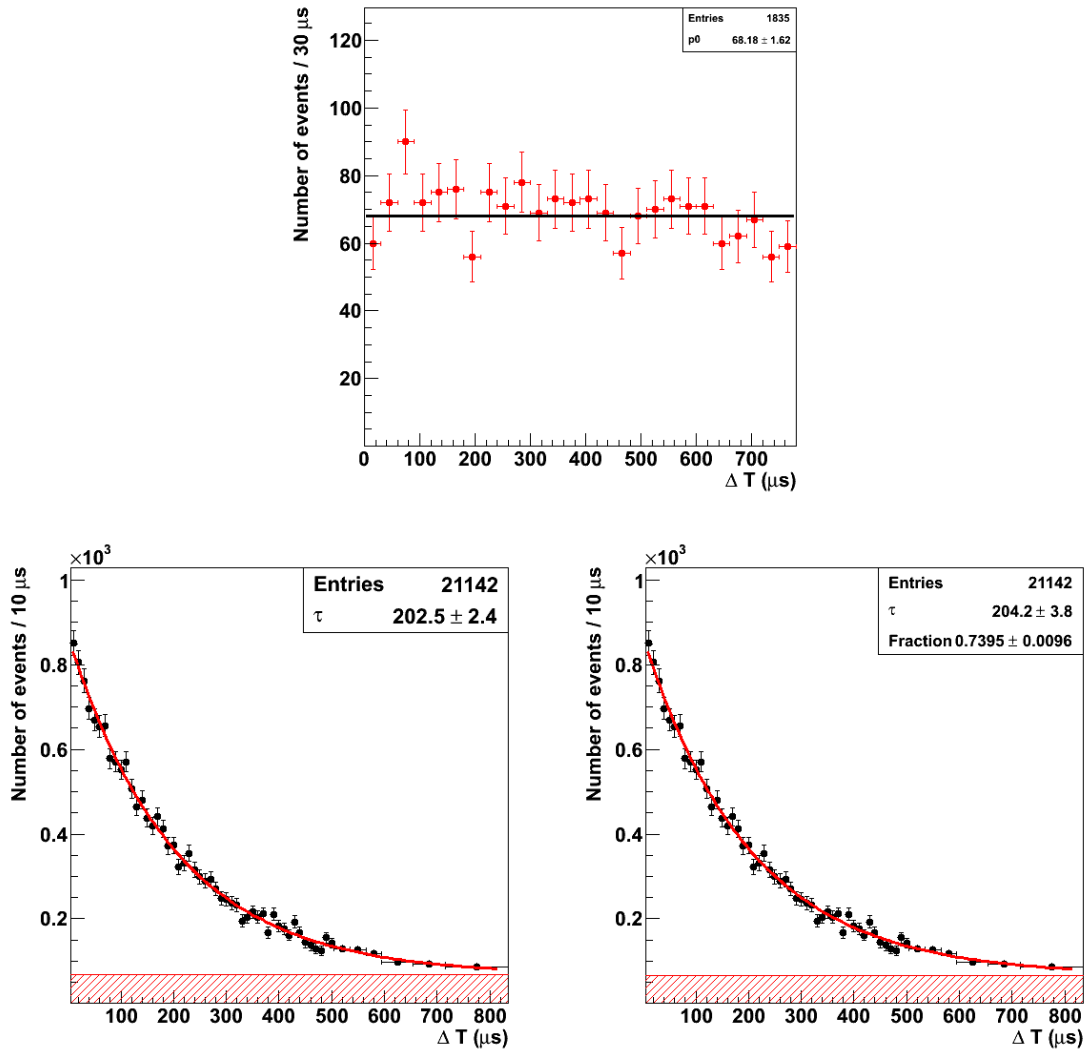


Figure 6.25 Upper panel: ΔT distribution from the random trigger data; Bottom left panel: ΔT distribution from source A which is fit with a fixed background level; Bottom right panel: ΔT distribution from source A which is fit with a free background level. The red shadow represents the expected background level.

Table 6.8 Comparison between the MC and the Am/Be source A.

	MC	fit with BG fixed	fit with BG free
signal efficiency	(18.2 \pm 0.3)%	(17.5 \pm 0.2)%	(17.6 \pm 0.2)%
τ	$\sim 200 \mu\text{s}$	(202.0 \pm 2.4) μs	(204.2 \pm 3.8) μs

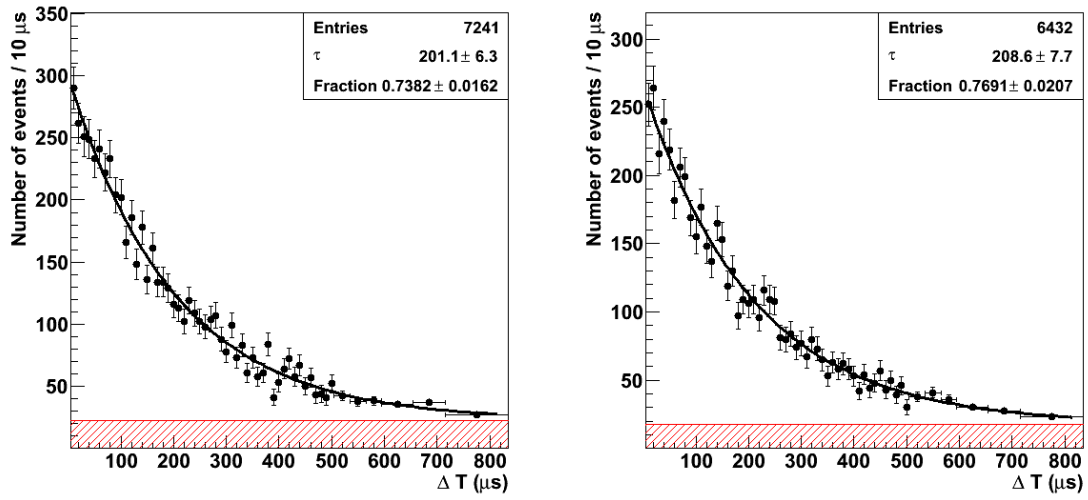


Figure 6.26 Left panel: ΔT distribution from source B which is fit with a free background level; Right panel: ΔT distribution from source C which is fit with a free background level. The red shadow represents the expected background level.

Table 6.9 Comparison between the MC and the Am/Be source B.

	MC	fit with BG free
signal efficiency	$(18.4 \pm 0.4)\%$	$(20.5 \pm 0.5)\%$
τ	$\sim 200 \mu s$	$(201.1 \pm 8.3)\mu s$

Table 6.10 Comparison between the MC and the Am/Be source C.

	MC	fit with BG free
signal efficiency	$(20.7 \pm 0.4)\%$	$(20.8 \pm 0.6)\%$
τ	$\sim 200 \mu s$	$(208.8 \pm 7.7)\mu s$

6.5 Application of the Neutron Tagging into Atmospheric Neutrino Data

Atmospheric neutrino data are also used to test the neutron tagging method. Table 6.11 lists the number of events after each reduction for atmospheric neutrinos with a live time of 1,667 days. For simplicity, only 1 ring and e-like events in FV are selected. The neutron tagging with the $\sim 10\%$ efficiency is applied to the remaining sample. The left panel and the right panel of Fig. 6.27 show the energy spectrum and the ΔT distribution, respectively. An events excess is observed in the spectrum and an exponential distribution of neutron life time is clearly seen, indicating that neutrons from atmospheric neutrinos are observed by this neutron tagging method.

Table 6.11 The number of events after each reduction for atmospheric neutrinos.

cuts	number of events
FV cut	13034
1 ring & e-like	4693

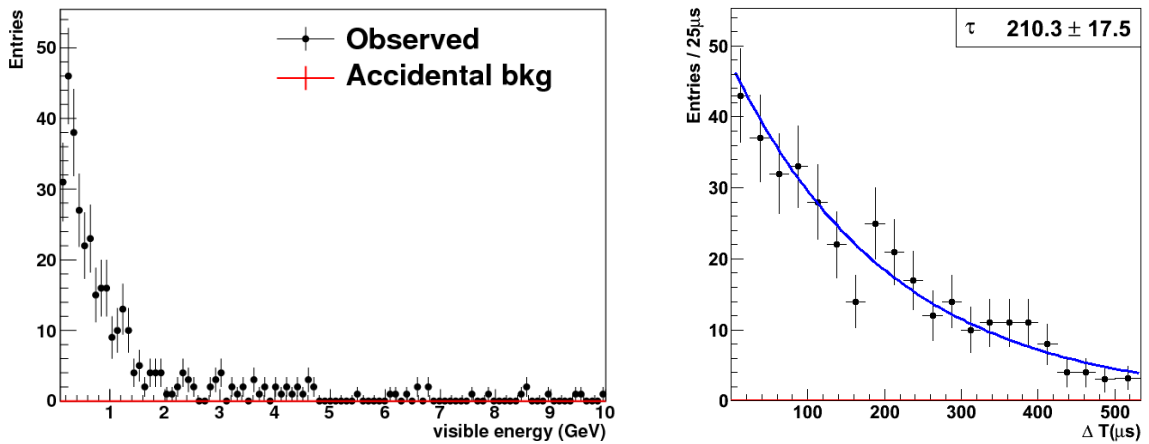


Figure 6.27 Left panel: The energy spectrum for the atmospheric neutrinos. The black points represent the data and the red line represents the expected accidental background; Right panel: ΔT distribution for the atmospheric neutrinos. The black points represent the data and the blue line represents the fit result.

6.6 Application of the Neutron Tagging to Solar Neutrino Events

For solar neutrinos with the SHE trigger, the related AFT trigger should have no correlated neutron information. The left panel and the right panel of Fig. 6.28 show the the distribution of $\cos\theta_{sun}$ and energy, respectively. θ_{sun} is the angle between the reconstructed direction of the electron and the direction from the position of the sun at the event time to the position of the electron. The expected number of the solar events after the neutron tagging is (2.5 ± 0.6) , while the observed number of solar events after the neutron tagging is one. The Poisson probability to observe lower than or equal to one event with a mean value of 2.5 $P_{2.5}(n \leq 1) = 28.7\%$. So the expected number of the solar neutrinos is consistent with the observed one event.

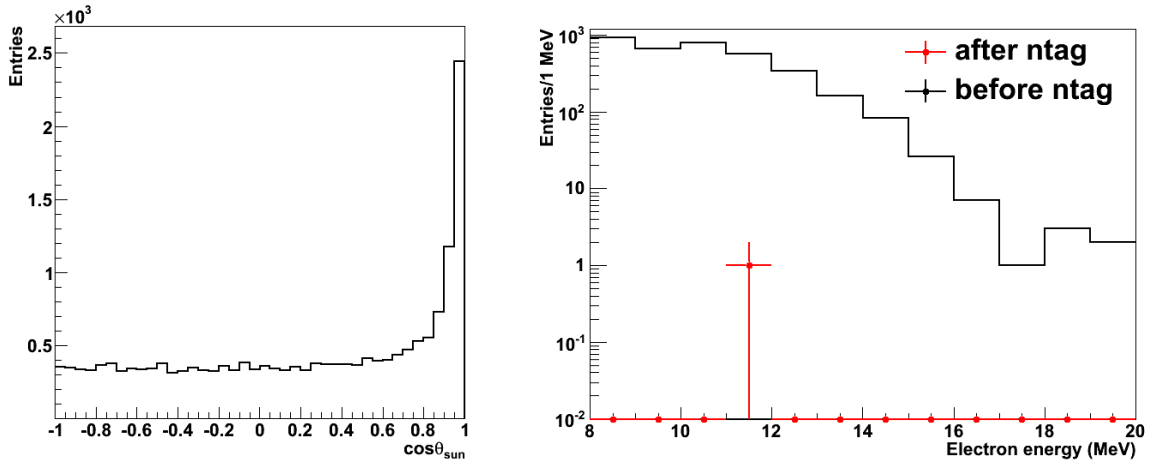


Figure 6.28 Left panel: The solar angle distribution of solar neutrinos. Right panel: The energy spectrum of solar neutrinos. The black line represent the data before neutron tagging and the red point represents the data after the neutron tagging.

6.7 Discussions of the Neutron Tagging Method

The energy and the vertex reconstruction of the 2.2 MeV γ 's could help to improve the separation between the signal and background events^[66]. Fig. 6.29 shows the reconstructed energy distribution for the MC simulated 2.2 MeV γ events and the background (random) events from the random trigger data. $N_{10} > 7$ is applied. This lead to the average energy higher than 2.2 MeV. In addition, the present energy reconstruction tool is only effective down to 3 MeV. The left panel of Fig. 6.30 shows the distribution of distance between the reconstructed and the true vertex of the MC simulated 2.2 MeV γ .

The right panel of Fig. 6.30 shows the distribution of distance between the reconstructed vertex of a random event and the vertex of a primary electron.

If the distribution of the distance could be utilized when the IBD reaction is simulated in SKDETSIM, an improvement will be expected for the signal-to-noise ratio of the neutron tagging.

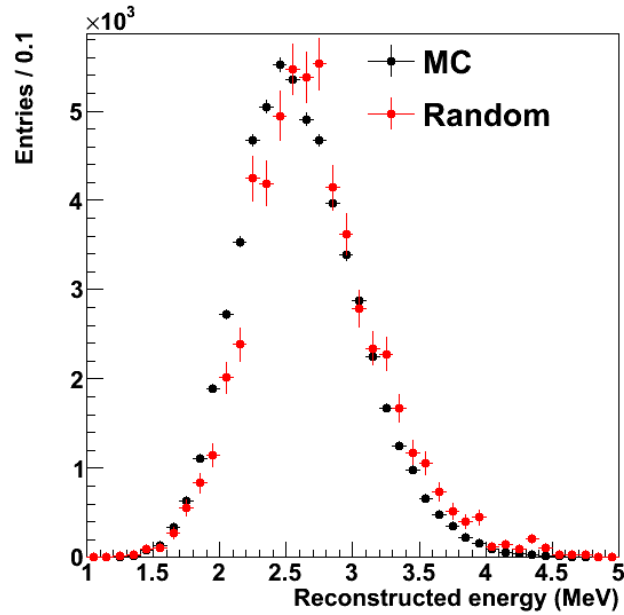


Figure 6.29 The reconstructed energy distribution for the MC simulated 2.2 MeV γ events and the background (random) events from random trigger data. $N_{10}>7$ is applied.

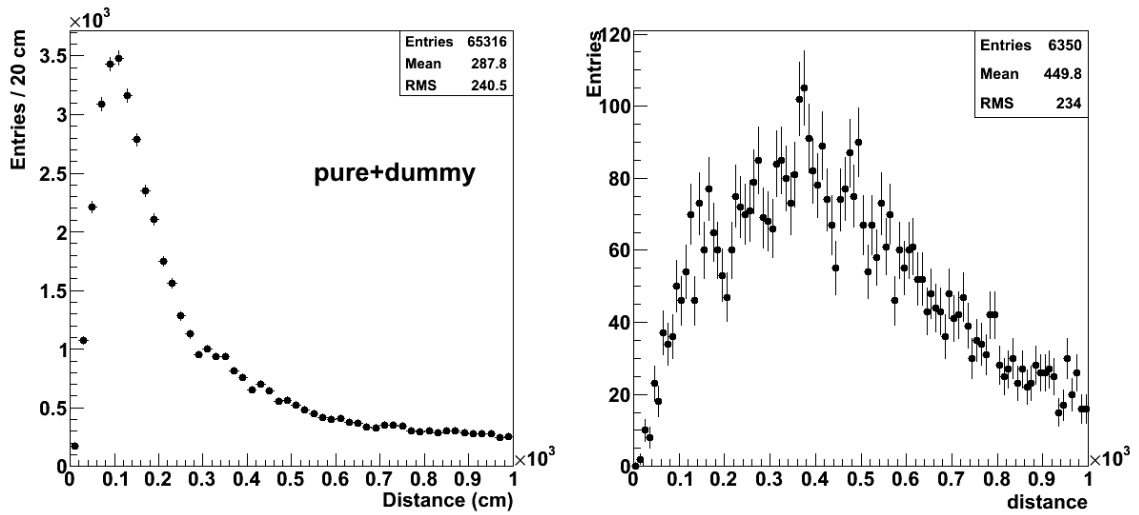


Figure 6.30 Left panel: The distribution of distance between the reconstructed and the true vertex of MC simulated 2.2 MeV γ 's. Right panel: The distribution of distance between the reconstructed vertex of a random event and the vertex of a primary electron.

Chapter 7 Analysis of the Spallation Background

In the golden energy window of 10-30 MeV for the SRN search, the dominant backgrounds are cosmic-ray muon spallation induced radioactive isotopes, among which ${}^9\text{Li}$ is the most dangerous one. This is due to the fact that ${}^9\text{Li}$ can decay into β^-n with a branch ratio of $(50.8 \pm 0.9)\%$ ^[55], and thus mimicking the IBD reaction. Although the spallation cuts can be applied to remove these backgrounds, part of ${}^9\text{Li}$ events may survive the cuts via the longer decay life time (see Table 7.1). Therefore, a precise measurement on the yield of ${}^9\text{Li}$ is of crucial importance for the SRN study. Such kind of measurement has never been conducted in water although a lot of studies have been carried on in scintillator detectors^[67,68].

This chapter will describe the first measurement on the yields of the spallation induced radioactive isotopes using the distribution of time after a muon. We will further improve the measurement of ${}^9\text{Li}$ yield using the neutron tagging method. The measurement can not only provide a useful information for the SRN search in water Cherenkov detector such as SK, the future GADZOOKS! and Hyper-K projects, but also can help to improve our knowledge on the MC simulations in Geant4 and FLUKA.

7.1 Measurement on Time Distribution

The yields of the major radioactive isotopes (listed in Table 7.2) induced by the cosmic muon spallation are measured from the time distribution. The data were collected from October, 2008 to October, 2014, corresponding to a total live time of 1,890 days. The spallation products are dominant above 6.5 MeV, while below 6.5 MeV are the radioactive events from the surrounding PMTs and FRP. The energy threshold for this measurement is therefore set at 6.5 MeV.

7.1.1 First Reduction

The first reduction includes a series of procedures to remove typical non-physical events. After the first reduction, the data sample is reduced significantly, providing an easily manageable one for the analysis. The first reduction is very similar as the long

Table 7.1 Possible radioactive isotopes induced by cosmic ray muons at SK^[55,57]. The 5-th column only lists the primary generation process of the isotopes^[34].

Isotope	Mean-life(s)	Decay mode	$E_{\text{kin.}}$ (MeV)	primary process
${}_{4}^{11}\text{Be}$	19.9	β^{-}	11.51	(n, $\alpha+2p$)
		$\beta^{-}\gamma$	9.41+2.1(γ)	
${}_{7}^{16}\text{N}$	10.3	β^{-}	10.44	(n,p)
		$\beta^{-}\gamma$	4.27+6.13(γ)	
${}_{6}^{15}\text{C}$	3.53	β^{-}	9.77	(n,2p)
		$\beta^{-}\gamma$	4.51+5.30(γ)	
${}_{3}^{8}\text{Li}$	1.21	β^{-}	~ 13.0	(π^{-} , $\alpha + {}^2H + p + n$)
${}_{5}^{8}\text{B}$	1.11	β^{+}	~ 13.9	(π^{+} , $\alpha + 2p + 2n$)
${}_{6}^{16}\text{C}$	1.08	$\beta^{-} + n$	~ 4	(π^{-} , n+p)
${}_{3}^{9}\text{Li}$	0.26	β^{-}	13.6	(π^{-} , $\alpha + 2p + n$)
		$\beta^{-} + n$	~ 10	
${}_{6}^{9}\text{C}$	0.18	$\beta^{+} + p$	3~15	(n, $\alpha + 4n$)
${}_{2}^{8}\text{He}$	0.17	$\beta^{-}\gamma$	9.67+0.98(γ)	(π^{-} , ${}^3H + 4p + n$)
		$\beta^{-} + n$		
${}_{4}^{12}\text{Be}$	0.034	β^{-}	11.71	(π^{-} , $\alpha + p + n$)
${}_{5}^{12}\text{B}$	0.029	β^{-}	13.37	(n, $\alpha + p$)
${}_{5}^{13}\text{B}$	0.025	β^{-}	13.44	(π^{-} , 2p+n)
${}_{5}^{14}\text{B}$	0.02	$\beta^{-}\gamma$	14.55+6.09(γ)	(n, 3p)
${}_{7}^{12}\text{N}$	0.016	β^{+}	16.38	(π^{+} , 2p+2n)
${}_{8}^{13}\text{O}$	0.013	$\beta^{+} + p$	8~14	(μ^{-} , $\mu^{-} + p + 2n + \pi^{-}$)
${}_{3}^{11}\text{Li}$	0.012	β^{-}	20.62	(π^{+} , 5p+ π^0 + π^{+})
		$\beta^{-} + n$	~ 16	

established SRN analysis or solar analysis. This reduction is comprised of the following cut criteria:

7.1.1.1 Bad Run Cut

The data are stored with the unit of a run. The normal run usually stores ~ 24 hours data, and is used for physical analysis. While for bad runs, the data quality is not reliable. The definition of bad runs are as follows:

- The run time is less than 5 min;
- The run time is within 15 mins after the high voltage (HV) recovery;
- Hardware or software problems happened in the runs;
- Calibration runs, test runs and the detector maintenance runs.

The bad runs are not used in physics analysis.

7.1.1.2 $50 \mu\text{s}$ Time Difference Cut

The energetic cosmic ray muons enter into the detector at ~ 2 Hz. The events within $50 \mu\text{s}$ after the LE triggered events could be decay-e events and "ringing" noise events. Such events are removed according to the SK requirement. In SK-IV, the un-tagged muon events are also taken into account when we calculate the time difference.

7.1.1.3 Fiducial Volume Cut

Enormous radioactive events from the the surrounding rock and the detector wall distribute very close to the wall of detector. In addition, the reconstruction softwares may fail to reconstruct the event with boundary close to the wall of detector. Thus, events outside the FV are removed.

7.1.1.4 Goodness Cut

G_V , the goodness value returned by BONSAI, represents the quality of vertex reconstruction. Events with G_V lower than 0.4 are removed. DirKS, another goodness value returned by BONSAI, represents the uniformity of azimuthal angle. A variable called ovaQ (One dimensional variable of Vertex and Angular reconstruction Quality) is defined as $\text{ovaQ} = G_V^2 - \text{DirKS}^2$. The events with ovaQ lower than 0.25 are removed.

7.1.1.5 Calibration Events Cut

Calibration events such as the laser and LED events were periodically taken during the normal data taking. These events are tagged by special event flags and trigger IDs. In this analysis, all calibration events are removed.

7.1.1.6 Noise Events Cut

Each PMT is fired with several thousand times per second. The p.e. value induced by dark noise tends to be small. We define a variable *ratio*, which is the fraction of $|Q|$ lower than 0.5 p.e.. The events with a *ratio* value greater than 0.55 are removed.

7.1.1.7 OD Cut

The OD triggered events indicate incoming cosmic ray muons. Events with the OD trigger are removed. In addition, events with greater than 19 OD PMT hits are also removed in case that the OD DAQ was in trouble.

7.1.2 Transverse Distance Cut

After the first reduction, physical events lower than 100 MeV are selected. Cosmic ray muons are reconstructed within ± 30 s around the low energy events using the Muboy fitter (see Sec. 4.4). The events with both OD & HE trigger pairs and the number of PMT hits greater than 1000 are sent into the muon fitter. Muboy can classify muons into 4 categories, the single through-going muons which account for $(84.1 \pm 0.3)\%$, the multiple muons which account for $(6.9 \pm 0.2)\%$, the stopping muons which account for $(4.6 \pm 0.2)\%$, the corner-clipping muons which account for $(4.1 \pm 0.1)\%$, and the remaining is no-fit muons. Discriminating variables to select the spallation product are developed:

- 1) dt , the time difference between the low energy event and the preceding or following muon event;
- 2) lt , the transverse distance between the low energy event and the preceding or following muon track.

The sample obtained using the preceding muons in 30 s advance is called the data sample, while the sample obtained using the following muons in 30 s afterwards is called the random sample. The spallation sample is obtained from the data sample subtracted by the random sample. Fig. 7.1 shows the lt distribution for the spallation sample and the

random sample using the single through-going muons. For other muon categories, the lt distribution could be obtained with similar fashion. The $lt < 200$ cm is applied to select the spallation product for all the muon categories while no lt cut is applied for no-fit and badly fit muons (goodness < 0.4). The fraction of events with a lt lower than 200 cm from the spallation sample using single through-going muons is $\sim 95\%$. However, this fraction becomes lower for other muon categories ($\sim 80\%$ for stopping muons, $\sim 65\%$ for multiple muons with only one track, and $\sim 40\%$ for multiple muons with more than one track). The efficiency of this lt cut is evaluated from a data sample with $dt < 10$ ms, 100 ms, 200 ms, 1 s, 5 s, 10 s, 20 s and 30 s to be $(78.8 \pm 3.8)\%$. It is noted that all the spallation backgrounds are assumed to have the same lt cut efficiency.

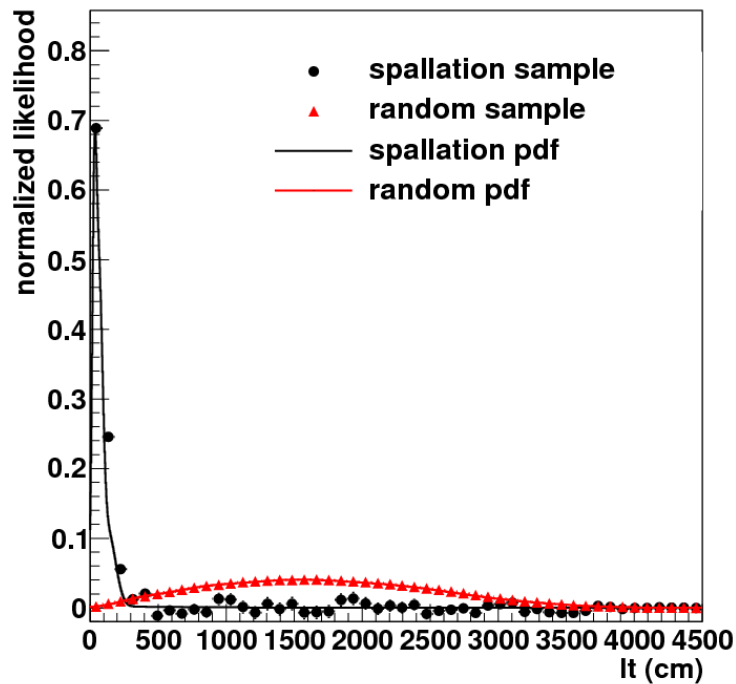


Figure 7.1 The distribution of transverse distance for the spallation sample and the random sample using the single through-going muons.

7.1.3 Life Time Analysis

It is very necessary to use a different and well-separated dt range to decouple the isotopes. First, the yields of the isotopes with a shortest life time (^{12}B and ^{12}N) are measured. The fit dt range is 0-0.1 s. This dt range is long enough to contain the isotopes

of ^{12}B and ^{12}N . Second, the yields of the isotopes with a longest life time (^{16}N and ^{11}Be) are measured. The fit dt range is 6-30 s. Third, the yields of the isotopes, ^9Li , $^8\text{Li}/^8\text{B}$, $^8\text{He}/^9\text{C}$, are measured using the dt range of 0.1~0.8 s. Notice that the life time of ^8He and ^9C is very close (0.17 s for ^8He and 0.18 s for ^9C), so the yields of ^8He and ^9C are grouped together. The case is similar for ^8Li and ^8B (1.21 s for ^8Li and 1.11 s for ^8B). In the fit range of 0.1-0.8 s, the yield of ^{16}N can not be neglected due to its large yield. At last, the yields of the isotopes, ^{15}C and ^{16}N , are measured using the dt range of 0.8-6.0 s. After all the yields of the isotopes are obtained from the different and well-separated dt range, these values are used as the initial inputs to fit the entire dt range of 0-30 s with the minimization of χ^2 . No limits are imposed on to the fit parameters.

The number of the i -th isotope events (N_i) is obtained from a χ^2 fit with the following pdf function:

$$F(t) = \sum_i \frac{N_i \cdot \epsilon_i}{\tau_i} e^{-dt/\tau_i} + \text{const} \quad (7-1)$$

where ϵ_i is the total selection efficiency for the i -th radioactive isotope, τ_i is the mean lifetime of the i -th radioactive isotope and const is the expected number of accidental background events, which is assumed to give a flat time distribution.

The yield of the i -th isotopes (Y_i) in the whole energy spectrum can be deduced from N_i using the following formula:

$$Y_i = \frac{N_i}{R_\mu T \rho L_\mu} \quad (7-2)$$

where R_μ is the measured muon rate, T is the livetime of the data set, ρ is the density of water, and L_μ is the measured path length of the muon track.

The production rate of the i -th isotopes (R_i) in the whole energy spectrum can be deduced from N_i using the following formula:

$$R_i = \frac{N_i}{\text{FV} \cdot T} \quad (7-3)$$

Where FV is the fiducial volume.

Fig. 7.2 shows the global fit result in 0~30 s. The χ^2/ndf is 5167.7/4991. The large χ^2 is due to the fact that only statistical uncertainty is used in the calculation. The p-value is 4.0%. To further show the fit quality, the fit residual (data-fit) is also shown and the result is uniformly distributed around zero. It is noted that the relative fraction between

^8B and ^8Li can affect the fit. However, the yields of ^8B and ^8Li can not be decoupled due to the similar life times and similar endpoint energies (~ 13 MeV for ^8Li and ~ 14 MeV for ^8B). In the global fit, the fractions of ^8B and ^8Li are assumed to be half and half, respectively. By changing the fraction of ^8Li from 0 to 100%, the differences in the yields are assigned as the systematic uncertainties.

Table 7.2 lists the production rates (R_i) in the whole energy spectrum for the spallation backgrounds from the global fit.

Table 7.2 The production rates (R_i) in the whole energy spectrum for the spallation backgrounds from the global fit. The second column lists the total selection efficiency (ϵ_i) for the i -th radioactive isotope. The first and second error in R_i represent the statistical and systematic uncertainties, respectively. The systematic uncertainty is obtained by changing the relative fraction of ^8Li from 0 to 1, together with the uncertainties from the data reduction.

radioactive isotopes	ϵ_i	production rate (R_i) in /kton/day
$^{12}_5\text{B}$	45.5%	$19.8 \pm 0.1 \pm 1.0$
$^{12}_7\text{N}$	56.2%	$2.8 \pm 0.1 \pm 0.1$
$^{16}_7\text{N}$	45.0%	$39.7 \pm 3.3 \pm 2.8$
$^{11}_4\text{Be}$	38.1%	$5.3 \pm 5.8 \pm 4.0$
^9_3Li	39.2%	$0.9 \pm 0.3 \pm 0.3$
$^8_2\text{He}/^9_6\text{C}$	22.2%, 50.2%	$0.4 \pm 0.5 \pm 0.3$
$^8_3\text{Li}/^8_5\text{B}$	42.8%, 51.3%	$8.3 \pm 0.3 \pm 0.3$
$^{15}_6\text{C}$	31.8%	$3.6 \pm 1.1 \pm 1.5$

7.2 Further Study on ^9Li Yield with the Neutron Tagging Method

We further improve the measurement on the ^9Li yield by tagging neutrons in the 500 μs forced trigger data. First reduction is applied as described in Sec 7.1. In order to select the β^- events, the following selection criteria are applied:

- 1) Time difference cut:** The distributions of the time difference (dt) for both the spallation sample and the random sample are shown in Fig 7.3. In order to suppress the contribution from both ^{12}B (mean-life 0.029 s) and ^{12}N (mean-life 0.016 s), the lower end of dt set at 0.05 s. In the time range of 0.05~0.5 s, the fraction of ^9Li is $\sim 68.1\%$.

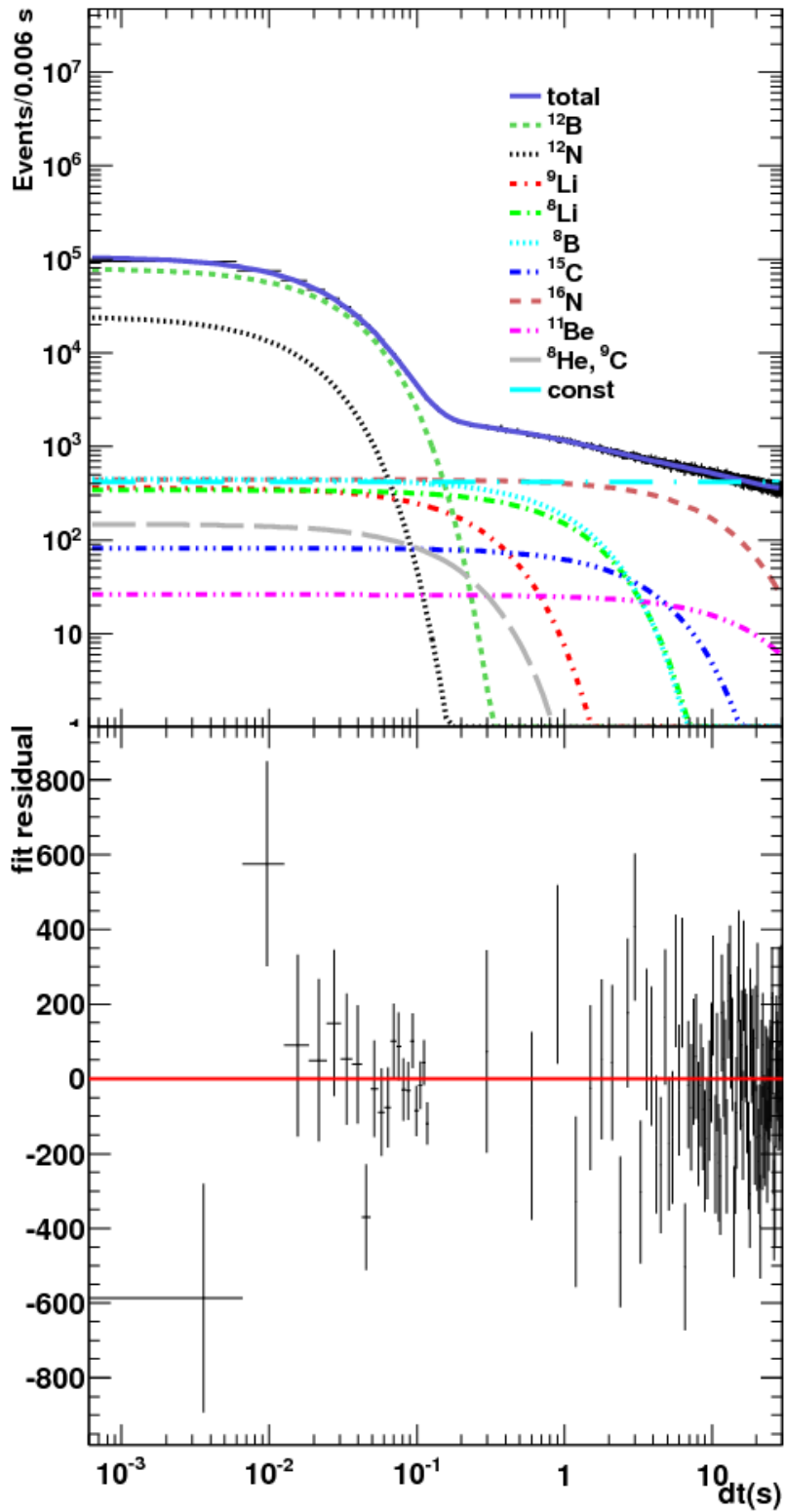


Figure 7.2 The global fit to the time difference distribution from 0 to 30 s. The χ^2/ndf is 5167.7/4991. The fit residual (data-fit) is also shown and the result is uniformly distributed around zero. For the purpose of display, bins are combined.

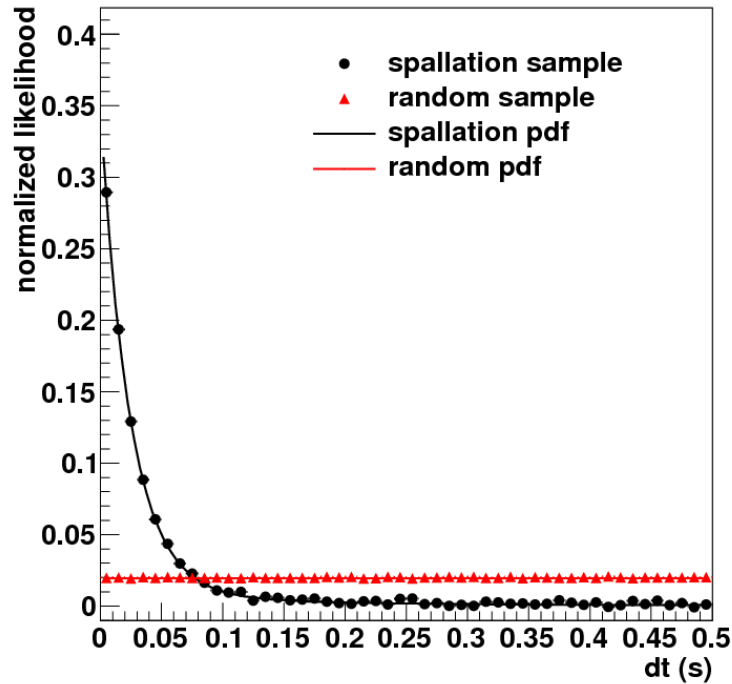


Figure 7.3 The distributions of the time difference for the spallation sample and the random sample using the single through-going muons.

2) Transverse distance cut: The lt is required to be shorter than 200 cm to select the spallation background for all the muon categories while no lt cut is applied for no-fit and badly-fit (goodness < 0.4) muons.

3) 1 ms muons cut: The study shows that the preceding muons within 1 ms before the low energy events are very likely to produce multiple neutrons events. While for the βn decay from ${}^9\text{Li}$, only 1 neutron can be produced. Therefore, no other preceding muons in within 1 ms is required.

The Q-value of ${}^9\text{Li}$ is ~ 13.6 MeV. For the βn decay of ${}^9\text{Li}$, the endpoint energy of the β 's is smaller. However, the ${}^9\text{Li}$ events can sneak into the region up to 15 MeV through the energy resolution effect. Fig. 7.4 shows the distributions for the true and the reconstructed energy from the βn decay mode of ${}^9\text{Li}$, respectively. Events with the energy above the SHE trigger threshold and lower than 15 MeV are used for this analysis.

The SHE trigger threshold was 10 MeV at the beginning of SK-IV and was lowered down to 8 MeV in the summer of 2011. Above the SHE energy threshold, the trigger efficiency is greater than 99%. The live time is 998 days for the 8 MeV trigger data and 892 days for the 10 MeV trigger data, respectively.

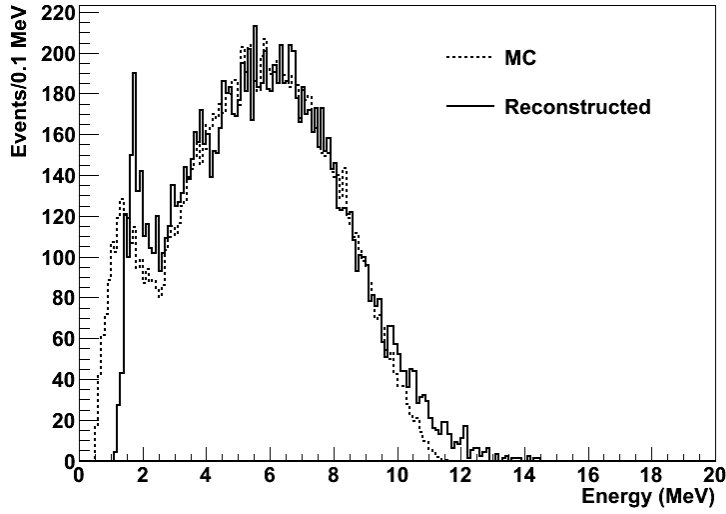


Figure 7.4 The distributions of the true (MC) and reconstructed energy from the βn decay mode of ${}^9\text{Li}$, respectively.

After the above cuts, the neutron tagging is applied to the remaining events. The left panel of Fig. 7.5 shows the energy distribution of the electron candidates. Events excess compared with the background-only scenario (black points over the black line) is observed. The right panel of Fig. 7.5 shows the distribution of lifetime for the observed neutron candidates. An unbinned maximum likelihood method with an exponential form plus a constant term is used to fit the ΔT distribution. The measured neutron lifetime is $(256 \pm 57) \mu\text{s}$, which is consistent with the expected $204.8 \mu\text{s}$ in^[65]. The events excess in both the energy spectrum and the exponential ΔT distribution indicate that βn pairs are observed.

Fig. 7.6 shows the distribution of time difference between the electron candidates and the preceding muon events. The total expected accidental backgrounds are 29 events of ${}^{12}\text{B}$, 17 events of ${}^8\text{Li}/{}^8\text{B}$, 7 events of ${}^{16}\text{N}$. A χ^2 fit with four exponentials is applied. The $\chi^2/\text{ndf}=11.2/13$. The measured lifetime of ${}^9\text{Li}$ is $(0.25 \pm 0.07)\text{s}$, which is in good agreement with the expected 0.26 s.

There are 151 βn pairs observed, in which (49.6 ± 11.5) accidental background events are expected. No multiple neutrons is observed. The production rate of ${}^9\text{Li}$ is calculated with the following formula:

$$N = R \cdot FV \cdot BR \cdot \epsilon(T1 \cdot \epsilon_1 + T2 \cdot \epsilon_2) \quad (7-4)$$

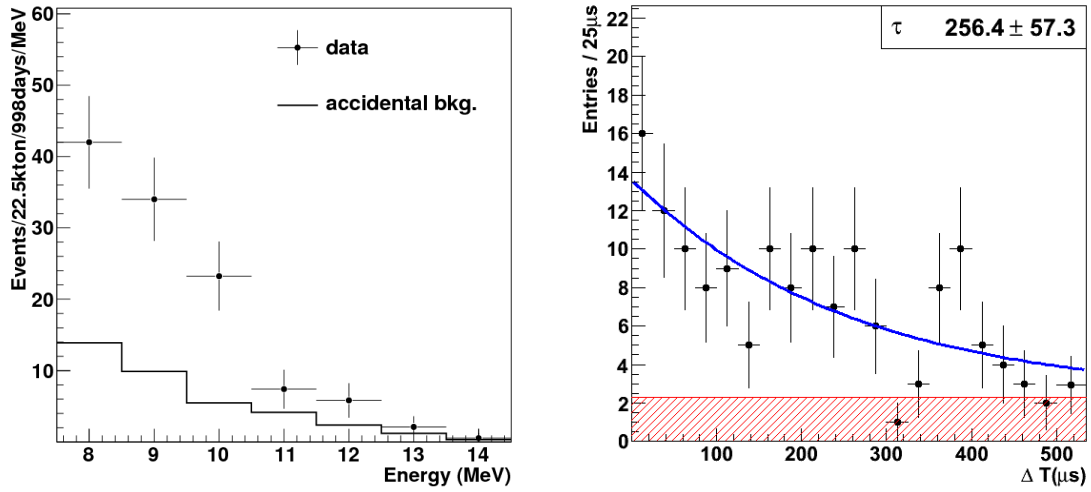


Figure 7.5 Left panel: The distribution of the reconstructed electron energy. The points represent the observed data with neutron tagging (scaled to live time of 8 MeV trigger data), the solid line represents the expected accidental background. Right panel: The distribution of lifetime for the observed neutron candidates. The black points represent the observed data, the blue line represents the fit result, and the red shadow represents the expected accidental background.

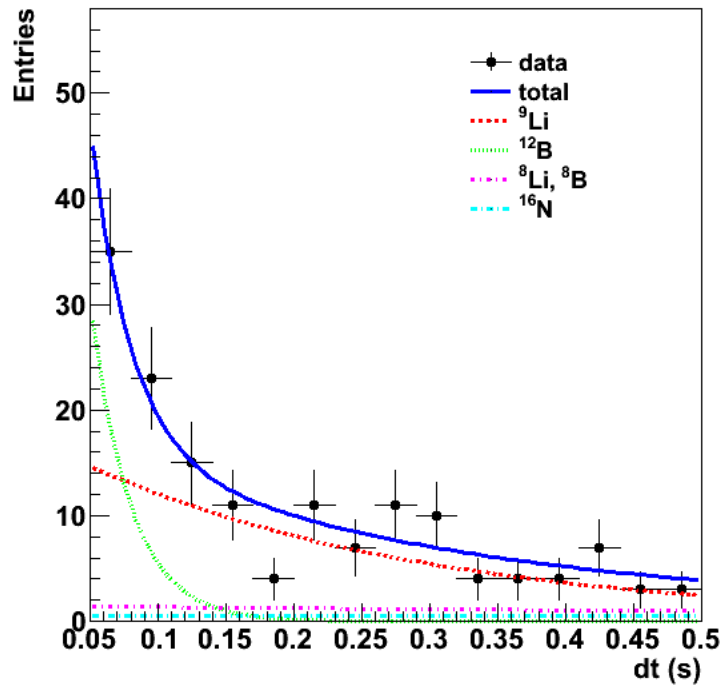


Figure 7.6 The distribution of time difference between the electron candidates and preceding muon events.

where $N = 101.4 \pm 12.3$ is the number of the ${}^9\text{Li}$ events, R is the production rate of ${}^9\text{Li}$ in the whole energy spectrum, FV is the fiducial volume, BR is the branch ratio, ϵ is the selection efficiency, $T1$ is the live time for the 8 MeV trigger data, ϵ_1 is the fraction of electrons above 8 MeV in β spectrum from βn decay mode of ${}^9\text{Li}$, $T2$ is the live time for the 10 MeV trigger data, ϵ_2 is the fraction of electrons above 10 MeV in β spectrum from βn decay mode of ${}^9\text{Li}$. The value of the variables in Eq. 7-4 can be found in Table 7.3. Therefore, the production rate of ${}^9\text{Li}$ is measured to be:

Table 7.3 The values of the variables in Eq.7-4.

N	FV	BR	ϵ	T1/T2(days)	ϵ_1	ϵ_2
101.4 ± 12.3	22.5	50.8%	4.9%	998/892	(16.3 \pm 1.3)%	(3.2 \pm 1.4)%

$$R = (0.95 \pm 0.12_{\text{stat.}}) \text{ kton}^{-1} \text{ day}^{-1} \quad (7-5)$$

The systematic uncertainty of ${}^9\text{Li}$ yield is listed in Table 7.4. The dominant systematic uncertainties come from the neutron tagging efficiency, the background estimation, the simulated energy spectrum of ${}^9\text{Li}$ and the multiple muons. Other systematic uncertainties are from the live time calculation, the first reduction, BR , lt cut. The total systematic uncertainty is 23.4%, which is added in quadrature. The production rate of ${}^9\text{Li}$ is $(0.95 \pm 0.12_{\text{stat.}} \pm 0.22_{\text{sys.}}) / \text{kton/day}$.

The yield of ${}^9\text{Li}$ (Y) is calculated with the following formula:

$$Y = \frac{N}{BR \cdot \epsilon(T1 \cdot \epsilon_1 + T2 \cdot \epsilon_2) \cdot R_\mu \cdot \rho \cdot L_\mu} \quad (7-6)$$

Y is $(0.56 \pm 0.07_{\text{stat.}} \pm 0.13_{\text{sys.}}) \times 10^{-7} \mu^{-1} \text{ g}^{-1} \text{ cm}^2$. We compare this measurement with the theoretical prediction in Ref^[34]. Table 7.5 lists a comparison of the isotope yields between the measurement and the prediction. For most of the isotopes, the measurements agree within the errors of the theoretical prediction. Although the measured yields of ${}^9\text{Li}$ and ${}^8\text{Li}/{}^8\text{B}$ are observed to deviate from the theoretical value, they are still consistent given a factor of two theoretical uncertainties.

Table 7.4 The systematic uncertainty of ${}^9\text{Li}$ yield.

systematic source	systematic uncertainty
neutron tagging efficiency	10.0%
background estimation	11.0%
ef1/ef2	15.4%
multiple muons	7.9%
live time	0.1%
First reduction	1.0%
BR	1.8%
It reduction	4.8%
total	23.4%

Table 7.5 Comparison of the yields (Y_i) in the whole energy spectrum for the radioactive isotopes between the measurement and the theory^[34]. Note that the theoretical prediction could have a factor of 2 uncertainty. The unit is $10^{-7}\mu^{-1}\text{g}^{-1}\text{cm}^2$.

radioactive isotopes	Y_i in measurement	Y_i in Ref. ^[34]
${}^{12}_5\text{B}$	$11.7\pm 0.1\pm 0.6$	12
${}^{12}_7\text{N}$	$1.6\pm 0.1\pm 0.1$	1.3
${}^{16}_7\text{N}$	$23.4\pm 1.9\pm 1.7$	18
${}^{11}_4\text{Be}$	$3.1\pm 3.4\pm 2.4$	0.81
${}^9_3\text{Li}$ w/o ntag	$0.5\pm 0.2\pm 0.2$	1.9
${}^9_3\text{Li}$ w/ ntag	$0.56\pm 0.07\pm 0.13$	1.9
${}^8_2\text{He}/{}^9_6\text{C}$	$0.2\pm 0.3\pm 0.2$	1.1
${}^8_3\text{Li}/{}^8_5\text{B}$	$4.9\pm 0.2\pm 0.2$	18.8
${}^{15}_6\text{C}$	$2.1\pm 0.6\pm 0.9$	0.82

We also compare the measurement results from the global fit with the results in Table IV in Ref^[69]. All are consistent within the uncertainties.

We now discuss the distribution of residual charges (Q_{res}) for muons. Q_{res} is defined using the follow formula:

$$Q_{\text{res}} = Q_{\text{obs}} - Q_{\text{unit}} \times L_{\mu} \quad (7-7)$$

where Q_{obs} is the observed charge for a muon, Q_{unit} is the expected average charge per cm. A Q_{res} much greater than zero indicates that muon showers are generated and spallation backgrounds may be produced. Fig. 7.7 shows the residual charge distribution for muons that are selected in the ${}^9\text{Li}$ analysis with neutron tagging method, together with that for muon data sample and random sample with both $dt < 10$ ms and $lt < 200$ cm using the low energy data above 6.5 MeV, without the neutron tagging applied. The number of muons decreases as the Q_{res} increases. As a result, we will not expect the ${}^9\text{Li}$ background induced by muons with large $Q_{\text{res}} > 2 \times 10^6$ p.e is significant, and can thus ignore. The peak around 2.5×10^6 p.e. of Q_{res} for the muon data sample is due to the PMT saturations. The spallation backgrounds induced by muons with large $Q_{\text{res}} > 2 \times 10^6$ p.e. is not significant.

For further concerns about very energetic muon track which could be not well-fitted but can produce spallation backgrounds, we state that

- The lt cut efficiency is directly evaluated from data, any such effect are efficiency corrected.
- The measured yields of ${}^{12}\text{N}$ and ${}^{16}\text{N}$ are already larger than that of the prediction, while for ${}^{12}\text{B}$, the yields are comparable.

The measurement of ${}^9\text{Li}$ yield is of importance for the present and future low-energy astrophysical neutrino experiments using the water Cherenkov technique, such as SK, future GADZOOKS! and Hyper-Kamiokande projects, since the IBD-like spallation background can affect the SRN search. GADZOOKS! has proposed to add 0.2% solution of gadolinium into SK water, which could greatly improve the signal-to-noise ratio for the SRN search. Assuming 99.5% rejection for ${}^9\text{Li}$ background after the spallation cuts, the expected number of ${}^9\text{Li}$ background is $2.3 \pm 0.3 \pm 0.5$ events/22.5kton/year above $E_{\bar{\nu}_e} = 10$ MeV. The measurement can also help to improve the simulations based on FLUKA and GEANT4.

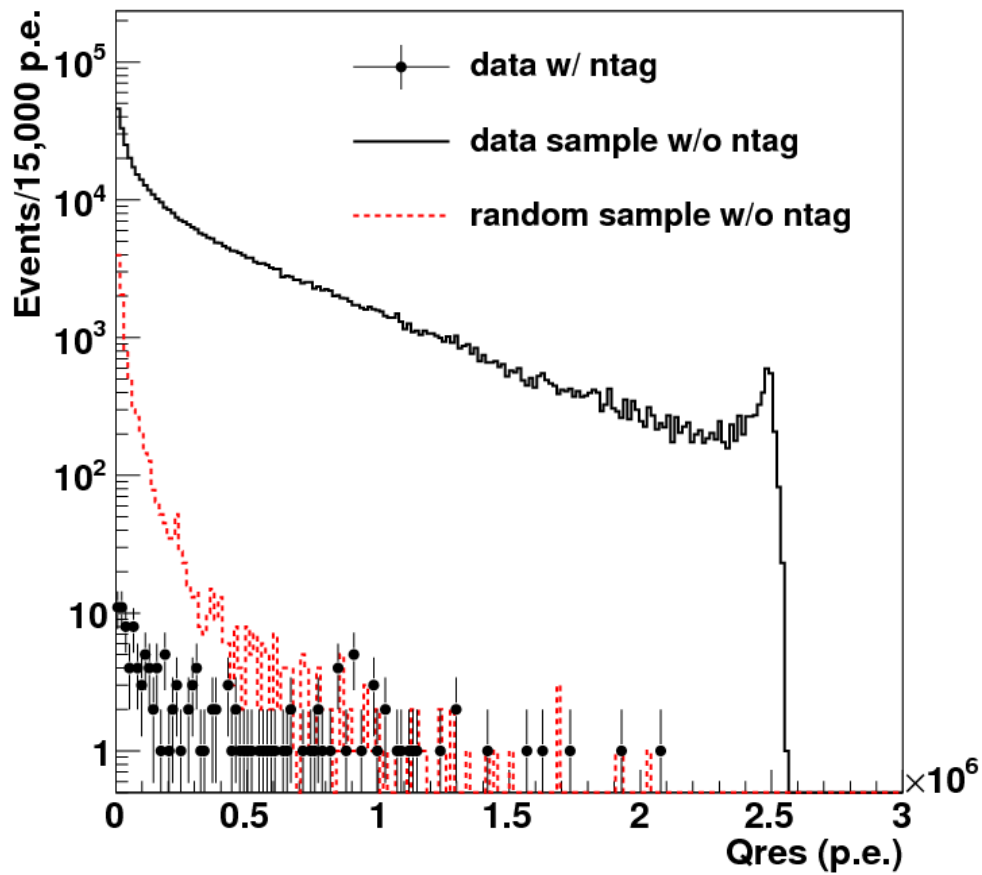


Fig. 7.7 The residual charge distribution for muons that were selected in the ${}^9\text{Li}$ analysis with neutron tagging (points, ntag is short for neutron tagging), together with that for muon data sample (solid) and random sample (dashed) with $dt < 10$ ms and $lt < 200$ cm using the low energy data above 6.5 MeV, but without the neutron tagging applied).

Chapter 8 Data Reduction for SRN Search

The search for the SRN in 13.3 MeV - 31.3 MeV at SK was conducted in Ref^[13]. Below 13.3 MeV, the spallation backgrounds were found to increase rapidly, limiting the search down to 10 MeV. Using the improved neutron tagging method with the better signal-to-noise ratio, we first get down to 9.3 MeV for the SRN search at SK. In order to search for the SRN $\bar{\nu}_e$ signal, a prompt e^+ and a delayed neutron signals are required. In this analysis, the data reduction is divided into two parts: the first one selects a e^+ sample and the second one further selects the e^+ with a delayed neutron sample.

8.1 First Reduction

The first reduction is exactly same as that described in Sec 7.1. No need to repeat in this section.

8.2 Spallation Cuts

The spallation cuts used in Ref^[59] is same as the cuts in SK-III^[36], which is based on the distributions of four variables (described in this section) above 16 MeV. In order to let the SRN search down to 9.3 MeV, the spallation cuts are re-tuned according to the s/\sqrt{b} . Although the neutron tagging can significantly suppress the spallation background with no associated neutron, the spallation cuts are still needed to remove the IBD-like spallation background.

Theoretically, the end point kinetic energy of the spallation induced radioactive isotopes cannot be greater than 20.6 MeV (see Table 7.1). However, the reconstructed energy can still extend up to 24 MeV due to the resolution effect. Therefore, the spallation cuts are only applied below 24 MeV.

A spallation likelihood is constructed using four discriminating variables^[48] described below:

- Dt , the time difference between the low energy event and the muon;
- lt , the transverse distance between the low energy event and the muon track;

- ln , the longitude distance between the low energy event and the spallation point (position of the dE/dx peak) along the muon track;
- Q_{peak} , the peak value of the dE/dx in the distribution of the deposited Cherenkov photons per 50 cm bin along the muon track.

It is noted that the distributions of the four variables change for different muon categories. The values of the four variables are calculated for the muons within ± 30 s around the low energy event. The definition of the data sample, the random sample and the spallation sample are already described in Sec 7.1.

8.2.1 Determination of Spallation background

Fig. 8.1 shows the distributions of dt , lt , ln and Q_{peak} using the single through muon as an example.

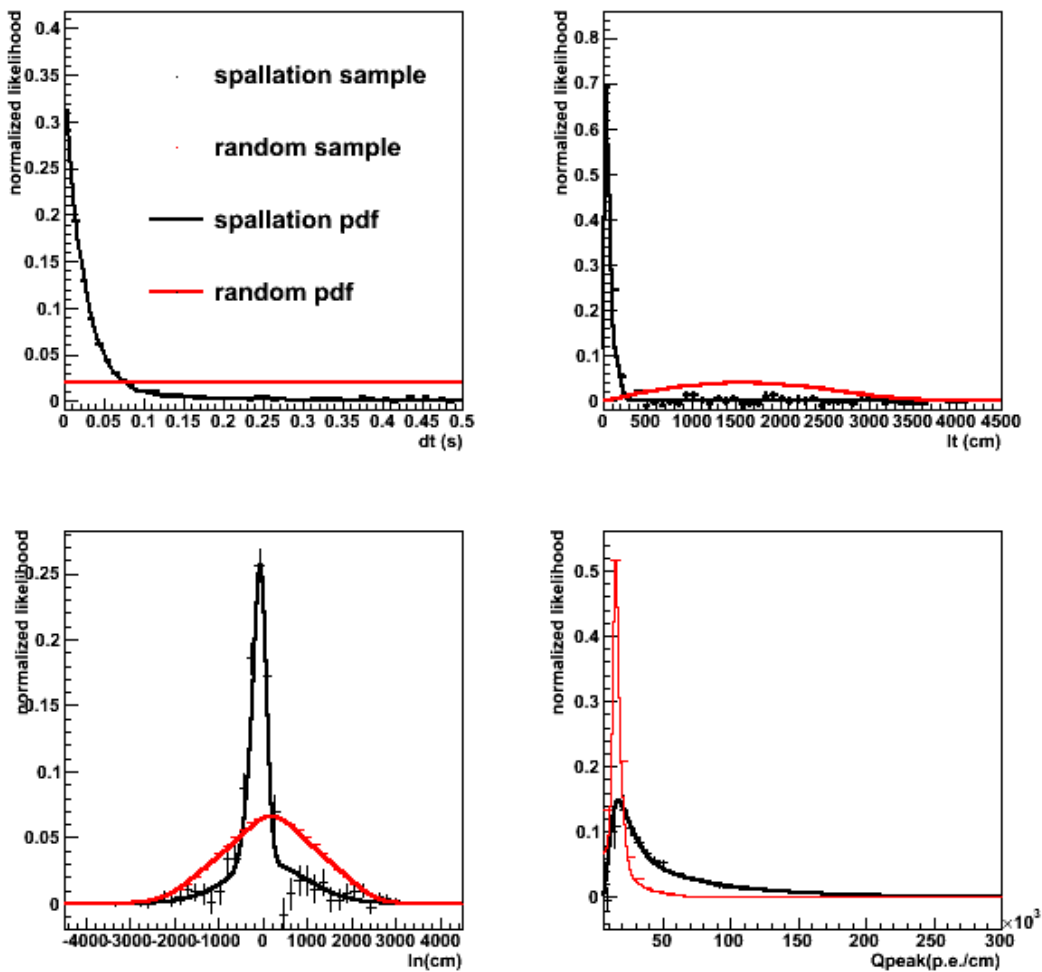


Figure 8.1 Distributions of the dt , lt , ln and Q_{peak} using the single through muon.

A spallation likelihood $L_{\text{spallation}}$ is calculated as:

$$L_{\text{spallation}} = \sum_i \log \frac{\text{PDF}_{\text{spallation}}^i}{\text{PDF}_{\text{random}}^i}, \quad (8-1)$$

where i runs over dt , lt , ln and Q_{peak} . Fig. 8.2 shows the distribution of the spallation likelihood for both the data sample and the random sample, respectively. The spallation cut position on the likelihood function is determined by the significance (s/\sqrt{b}) curve shown in Fig. 8.3. The cuts for the other muon categories are treated in a similar fashion.

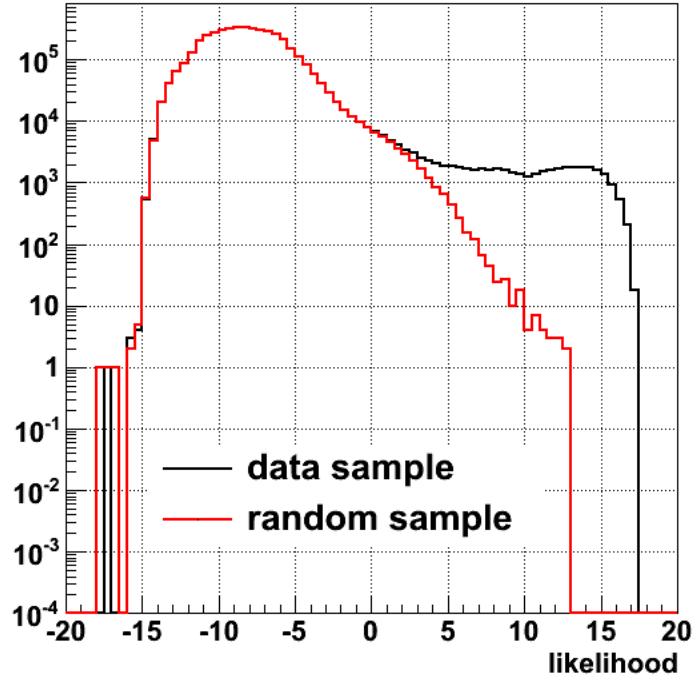


Figure 8.2 Distributions of the spallation likelihood using the single through-going muons.

The random sample is used to evaluate the inefficiency of the spallation cuts, which is then calculated in the $R^2 - z$ panel with a position dependence. The overall inefficiency is calculated with the position distribution of SRN MC (LMA model) simulated events. The SRN efficiency for the spallation cuts are listed in Table 8.1. The efficiencies above 14 MeV are similar between SK-IV and SK-III since the similar cuts are used.

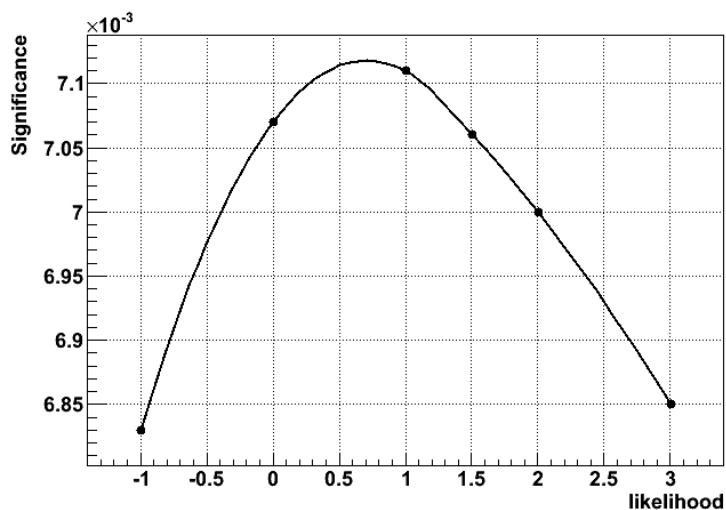


Figure 8.3 Distributions of the significance as a function of the spallation likelihood for events around 10 MeV.

Table 8.1 SRN efficiency for the spallation cuts.

Energy range	Efficiency in SK-IV	Efficiency in SK-I/III
18-24 MeV	89.8%	89.7%
14-18 MeV	80.5%	80.3%
12-14 MeV	72.1%	-
11-12 MeV	61.2%	-
8-11 MeV	51.3%	-

8.3 Incoming Events Cut

The physics events originating outside the detector can travel further into the FV. The *effwall* is the distance between the reconstructed vertex and the position on the wall of detector by opposite projecting along the reconstructed direction. Fig. 8.4 shows the distributions of the *effwall* for both the data and the SRN signal, respectively. All events with an *effwall* shorter than 300 cm are removed; Events with an *effwall* shorter than 450 cm are also removed if the reconstructed energy is lower than 22 MeV. Events with an *effwall* shorter than 600 cm are removed if the reconstructed energy is lower than 12 MeV.

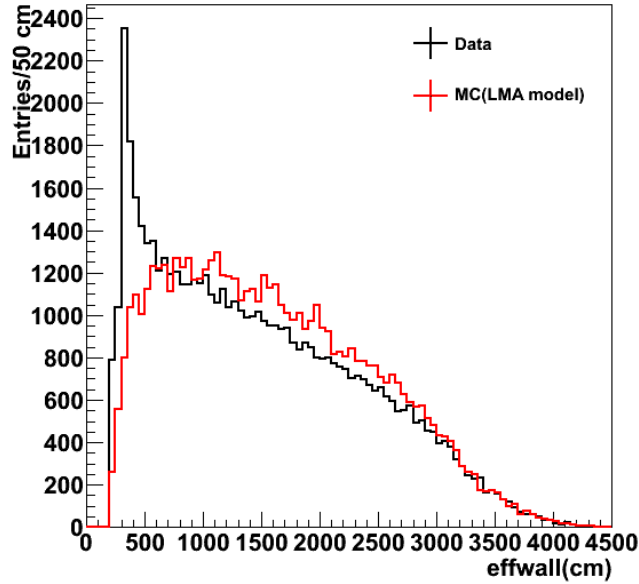


Figure 8.4 Distributions of the *effwall* for the data (black line) and the SRN signal (red line).

8.4 Solar Events Cut

The electron scattered by a solar neutrino event via $\nu + e^- \rightarrow \nu + e^-$ carries the direction information of solar neutrino. The angle between the direction of a solar neutrino event (from the position of the sun at the event time to the reconstructed vertex) and the reconstructed direction of the electron is referred to as the θ_{sun} . Fig. 8.5 shows the distribution of the $\cos \theta_{sun}$. A sharp peak of $\cos \theta_{sun}$ is seen around 1. Events with both the $\cos \theta_{sun}$ greater than 0.9 and the energy lower than 16 MeV are rejected. The residuals of the solar neutrinos with energy greater than 16 MeV are expected to be removed by the neutron tagging cut.

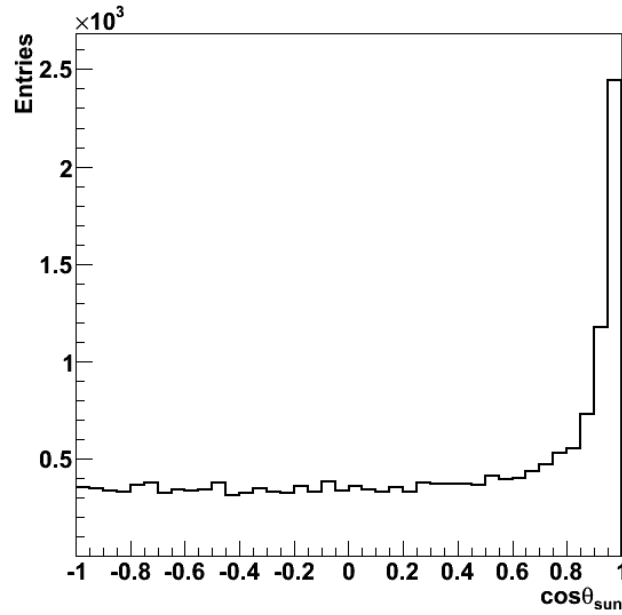


Figure 8.5 The distribution of the $\cos \theta_{\text{sun}}$. The peak at one is for the solar neutrinos.

8.5 Cherenkov Angle Cut

Above the SHE trigger threshold, the e^\pm 's are relativistic. The Cherenkov angle for a relativistic charged particle is $\sim 42^\circ$. For muons with momentum around 100-500 MeV, the reconstructed energy can be within 10-90 MeV. These muons are produced by the atmospheric $\nu_\mu/\bar{\nu}_\mu$ events and have a lower Cherenkov angle than 42° . Multiple γ events tend to have a larger Cherenkov angle since they have an isotropic light pattern. Events with an electron and a γ from the spallation induced radioactive isotopes also have the similar pattern. Fig. 8.6 shows the distribution of Cherenkov angle. Events with a Cherenkov angle lower than 38° or greater than 50° are removed.

8.6 Pre/post Activity Cut

The events with more than one peak on the distribution of the residual time are removed since the expected prompt signal can only have one peak. The time length of the SHE trigger is $40 \mu\text{s}$, ranging from $-5 \mu\text{s}$ to $35 \mu\text{s}$. A muon with energy lower than the Cherenkov threshold cannot be observed and thus is called the invisible muon. The decay-e's from these invisible muons are irreducible background since the preceding muon can not be tagged. These decay-e's can be removed if a prompt gamma is produced in the interaction between the incident atmospheric neutrino and the oxygen. The number

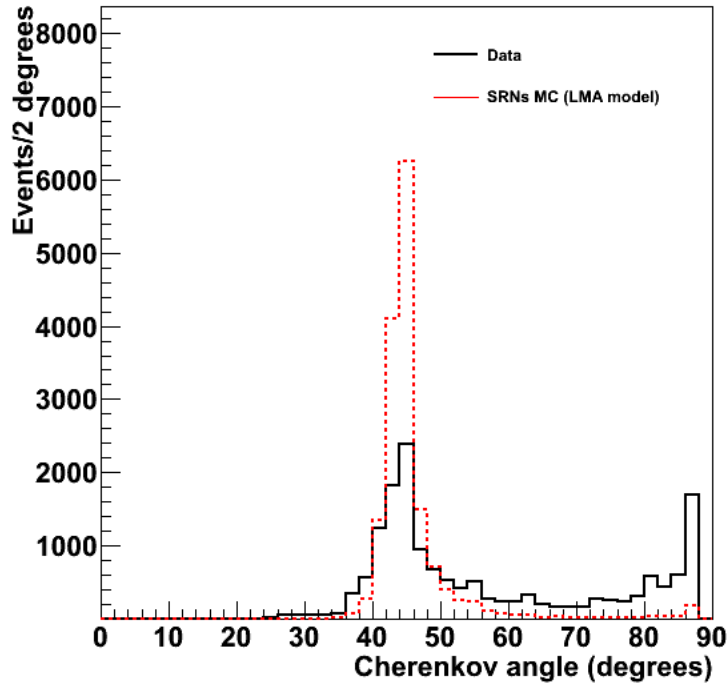


Figure 8.6 Distributions of the Cherenkov angles for the data (solid histogram) and the SRN signal (dashed histogram).

of maximum PMT hits in a 15 ns time window (N_{15}) is calculated. Fig. 8.7 shows the distribution of the maximum N_{15} using the 5 μ s random trigger data. Events with a maximum N_{15} in the 5 μ s data greater than 11 (referred to as the pre-activity events) are removed. For the events with energy lower 12 MeV, the maximum N_{15} is required to be lower than 8. In most cases, the μ - e decay events can have two peaks on the time profile. Although the Cherenkov angle cut removes most of these μ - e decay events, some may survive the cut. The later 35 μ s can cover the decay- e event with 100% since the lifetime of the muons is 2.2 μ s. The right panel of Fig. 8.7 shows the distribution of the maximum N_{15} using the 35 μ s random trigger data with a 2.2 MeV γ . The events with the maximum N_{15} in later 35 μ s data greater than 19 (referred to as the post-activity events) are removed. For the event with energy lower 12 MeV, the maximum N_{15} is required to be lower than 18. The inefficiency for this cut is 1.7%.

Fig. 8.8 and Fig. 8.9 shows the event display of a typical pre-activity and post-activity event, respectively.

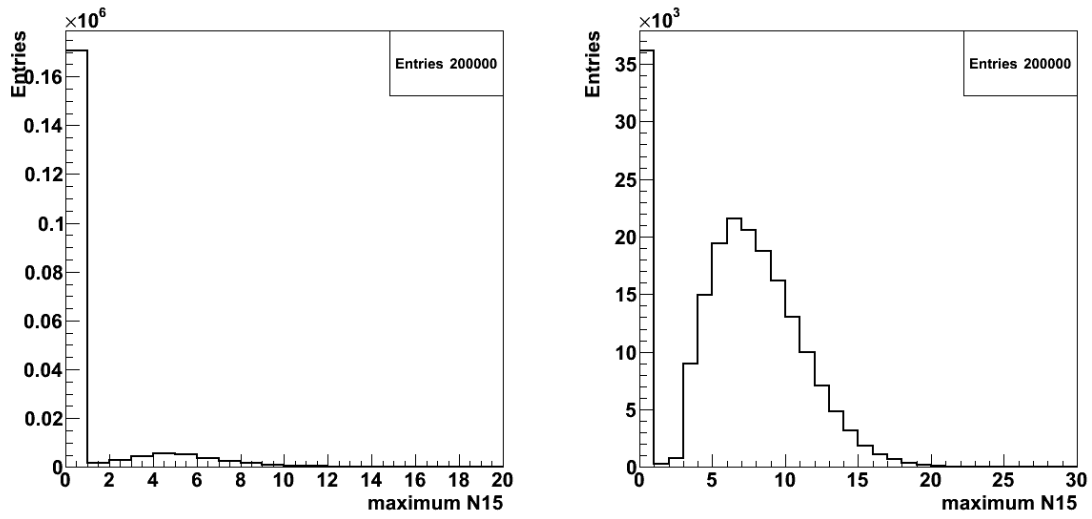


Figure 8.7 Left panel: The distribution of the maximum N_{15} using the $5 \mu\text{s}$ random trigger data. Right panel: The distribution of the maximum N_{15} using the $35 \mu\text{s}$ random trigger data with a 2.2 MeV γ .

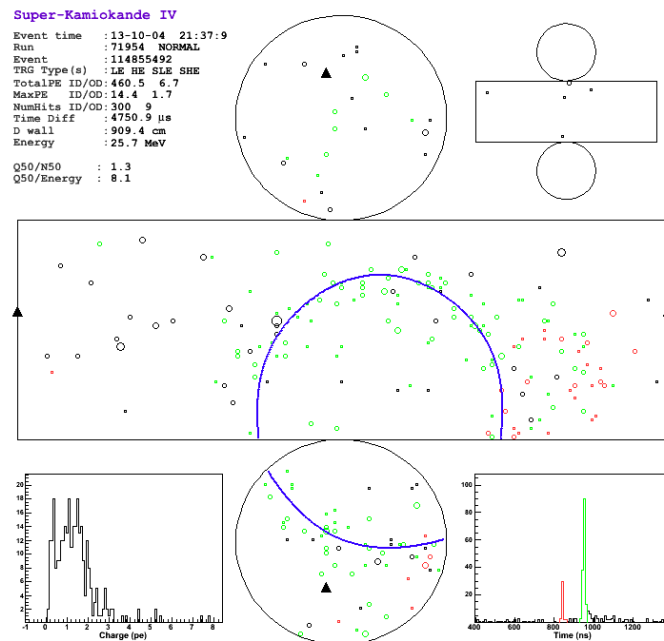


Figure 8.8 Event display for a pre-activity event. A small pre-activity is observed at 850 ns in the time distribution.

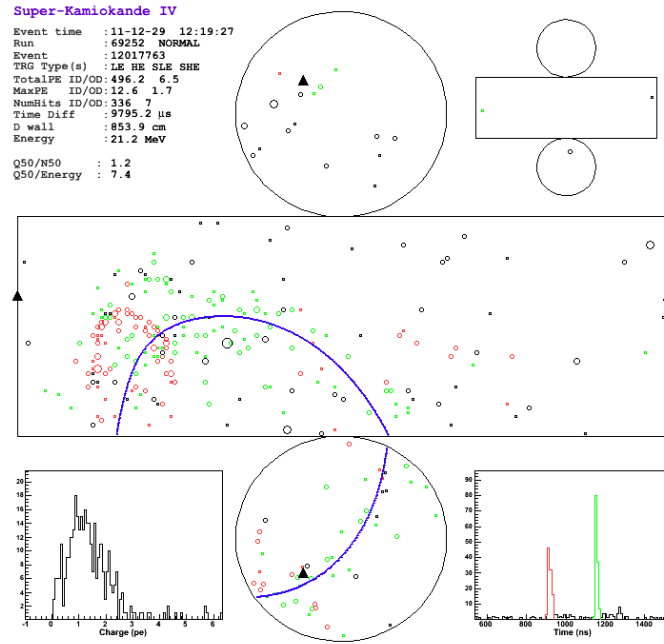


Figure 8.9 Event display for a post-activity event. A post-activity is observed at 1200 ns in the time distribution.

8.7 Pion Cut

Pion events with higher momentum cannot be rejected by the Cherenkov angle cut. Such pion events tend to have a sharper Cherenkov angle distribution. While for electrons, the distribution of the Cherenkov angle tend to be wider due to the multiple scattering. Based on this logic, a variable called π_{like} is constructed with the definition of number of entries within $\pm 3^\circ$ around the peak of the Cherenkov angle distribution over that of within $\pm 10^\circ$. Events with π_{like} greater than 0.58 are removed.

8.8 Multi-ring Cut

Atmospheric neutrino events can produce multiple charged particles by the interaction with water. As the multiple charged particles may share the same timing peak, such events can not be removed by the pre/post activity cut. These multiple charged events can have multiple Cherenkov rings. We use a ring counting tool described in Ref^[70] to remove this background. The number of rings for a single electron event can have more than one ring due to the fuzziness of Cherenkov ring pattern. To reduce the inefficiency, we define θ_{ring} as the angle between any two rings. Events with $\theta_{ring} > 60^\circ$ are removed.

8.9 μ/π Cut

There are about 2 μ/π events/year that can survive all the cuts described above. In order to remove the remaining μ/π background, a variable on Q50/N50 is constructed in SK-IV^[59]. Fig. 8.10 shows the distribution of Q50/N50 as a function of the reconstructed energy for e , μ and π , respectively. Events with a Q50/N50 greater than $(2.0+0.0025\times\text{energy})$ are removed.

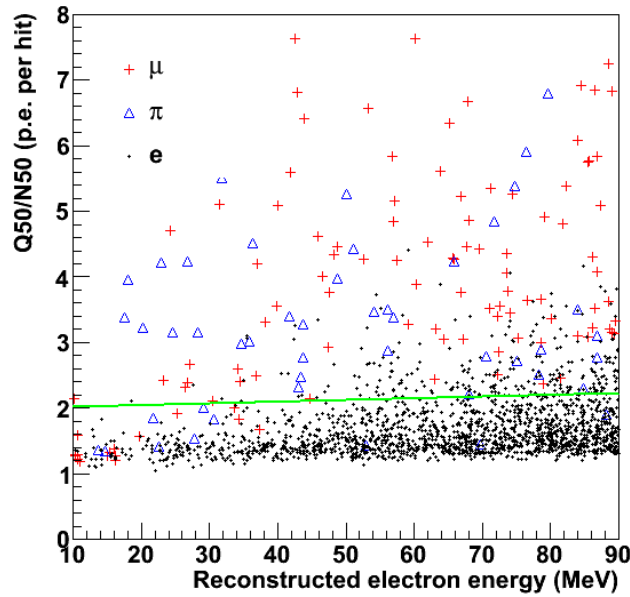


Figure 8.10 The distribution of Q50/N50 as a function of the reconstructed energy for e , μ and π , respectively. The atmospheric neutrino MC simulated events are used for this calculation.

8.10 Neutron Tagging

We use the improved neutron tagging method (see Sec. 6.3.3) with the better signal-to-noise ratio to tag the delayed neutron signal. For $E_{\bar{\nu}_e} > 14.3$ MeV, the neutron tagging with the loose cut ($\sim 18\%$ signal efficiency and $\sim 0.3\%$ accidental background level) is applied. For $E_{\bar{\nu}_e} < 14.3$ MeV, the neutron tagging with the tighten cut ($\sim 10\%$ signal efficiency and $\sim 0.065\%$ accidental background level) is applied.

8.11 Summary of Reduction Efficiency

For most the cuts, the signal efficiencies are evaluated by the MC simulation. Various SRN models have slightly different efficiencies. Here, the LMA model is used for estimating the efficiencies. For the spallation cuts, the inefficiency is calculated with both an inefficiency map in the $R^2 - z$ panel and the position distribution of the simulated SRN sample. The pre/post-activity inefficiency is estimated using the random trigger data. Table 8.2 lists the summary of the reduction efficiencies.

Table 8.2 Summary of the reduction efficiencies for both data sets with different trigger thresholds.

Reduction step	Efficiency in 8-30 MeV	Efficiency in 10-30 MeV
First reduction	>99%	>99%
Spallation cut	77.1%	80.9%
Incoming event cut	92.8%	93.5%
Solar cut	97.2%	97.5%
Cherenkov angle cut	88.6%	90.2%
Pre/post activity cut	98.3%	98.3%
π_{like} cut	99.2%	99.2%
Multi-ring cut	99.5%	99.4%
μ/π cut	99.8%	99.4%
neutron tagging	14.9%	15.4%
Total efficiency	8.8%	9.9%

Chapter 9 SRN Analysis and Results

The final $\bar{\nu}_e$'s sample is obtained from the events with both a prompt e^+ signal and a delayed neutron signal. Since the sample used in the analysis consists of both data sets for 11.3 MeV and 9.3 MeV neutrino energy thresholds, we refer these two data sets as data I and data II, which correspond to the live time of 892 days and 998 days, respectively. This chapter will describe the features of SRN candidates, the evaluation of background, the systematics on both the efficiency and the background estimation. In the end, the upper limit of SRN flux will be calculated and compared with the theoretical models as well.

9.1 The SRN Candidates

The data collected from year 2008 to 2014 are used to search for the SRN signal at SK. After applying all the cuts, there are 18 (7 in data I and 11 in data II) candidate events leftover. Fig. 9.1 shows the energy spectrum for these candidates. It is observed that the background still dominates the region with energy less than 15 MeV. Most of the background originate from the accidental ones with a prompt e^+ associated with a noise mis-tagged as a neutron. Table 9.1 lists the numbers of the observed data and the expected background, the latter will be explained in Sec.9.2. Fig. 9.2 also shows the distribution of the life time for the observed neutron candidates. Using an exponential plus a constant function to fit the life time distribution gives a result of $(197.7 \pm 284.4)\mu\text{s}$ with $\chi^2/\text{ndf}=19.5/20$, while using a constant term to fit gives a result of $\chi^2/\text{ndf}=17.3/20$, indicating that most of events are not IBD events. Therefore, we can conclude that no obvious SRN signal is observed.

9.2 Background Estimation

9.2.1 Atmospheric $\bar{\nu}_\mu/\nu'_\mu$ s

Atmospheric $\bar{\nu}_\mu/\nu_\mu$ can interact with water via the CC process: $\nu_\mu + n \rightarrow \mu^- + p$ or $\bar{\nu}_\mu + p \rightarrow \mu^+ + n$. In the first process, no direct neutron is produced, and the secondary neutron production is negligible in low energy case. While in the second

Table 9.1 The number of both the observed and the expected events in each MeV bin.

Positron/electron energy (MeV)	observed events	expected events
8-9	6	6.2
9-10	2	3.2
10-11	2	2.2
11-12	2	1.2
12-13	2	0.7
13-14	0	1.0
14-15	1	0.5
15-16	0	0.3
16-17	0	0.2
17-18	0	0.1
18-19	1	0.1
19-20	0	0.2
20-21	0	0.2
21-22	0	0.2
22-23	0	0.2
23-24	0	0.2
24-25	0	0.3
25-26	0	0.2
26-27	1	0.2
27-28	1	0.3
28-29	0	0.3
29-30	0	0.2

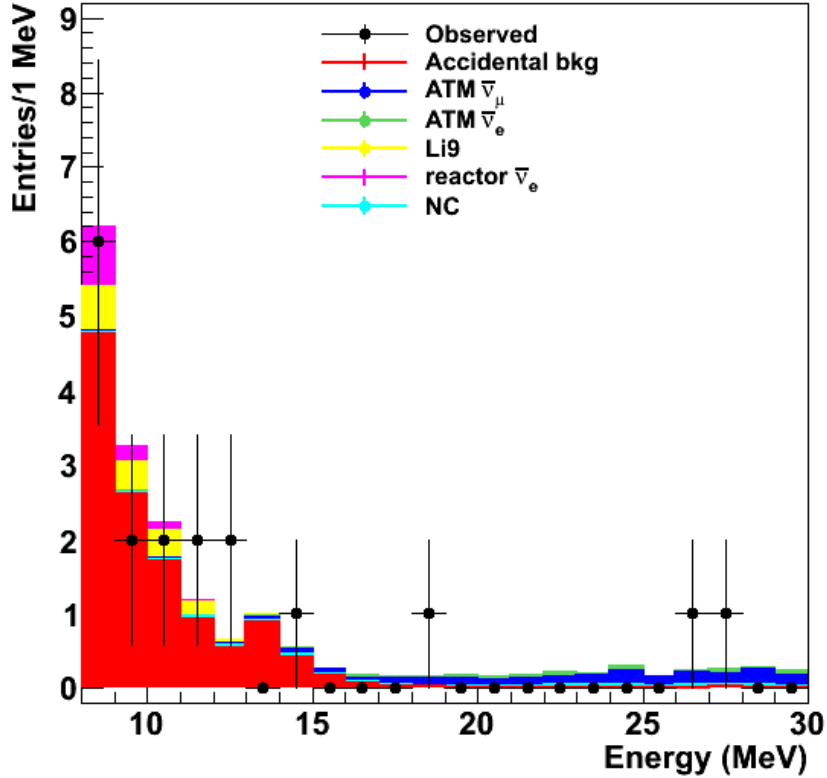


Figure 9.1 Positron/electron energy spectrum for the final SRN candidates.

process, daughter muons and direct neutron are produced. However, the daughter muons can have energy below the Cherenkov threshold, these invisible muons decay to positrons which fake the primary signal, forming the irreducible background at SK^[36]. Because of the tagging of the delayed neutrons, only the atmospheric $\bar{\nu}_\mu$ CC events can contribute to the final sample. The number of atmospheric $\bar{\nu}_\mu$ CC background is estimated by using a MC sample of simulated atmospheric neutrino events^[71], which corresponds to a live time of 100 years. Fig. 9.3 shows the energy spectrum of decay-e from the invisible muons. The distribution follows Michel electron spectrum. In this MC sample, all the primary cuts are applied except for the spallation cuts and the solar cut, since the efficiencies for these two categories of cuts can be well estimated from the data. The number of $\bar{\nu}_\mu$ background events in the SRN candidates is finally estimated to be (2.0 ± 0.4) (0.9 ± 0.2 in data I and 1.1 ± 0.2 in data II), taking into account of the effect of oscillation, the efficiency of neutron tagging and the efficiency of both the spallation and solar cuts.

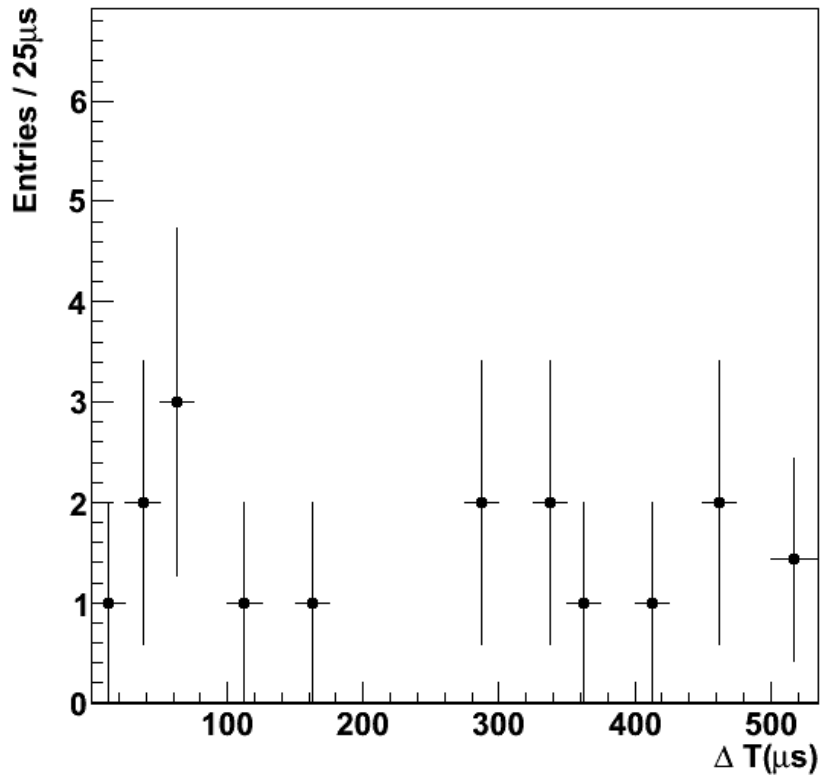


Figure 9.2 The distribution of the neutron life time for the observed SRN candidates.

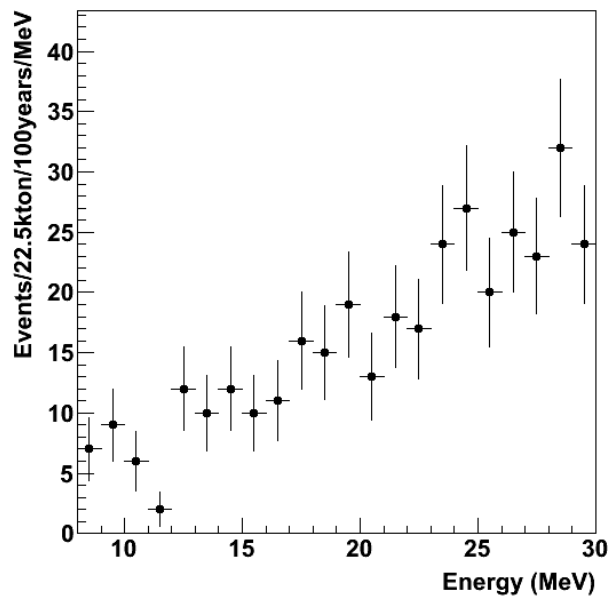


Figure 9.3 The positron/electron energy spectrum for the MC simulated atmospheric $\bar{\nu}_\mu/\nu_\mu$ CC events. The sample corresponds to a live time of 100 year.

9.2.2 Atmospheric $\bar{\nu}_e$'s

The atmospheric $\bar{\nu}_e$ CC background has exactly the same signature as the SRN signal and are therefore irreducible in this analysis, while the atmospheric ν_e background has no neutron and can thus be ignored. The number of atmospheric $\bar{\nu}_e$ background in the SRN candidates is estimated to be (0.5 ± 0.1) (0.23 ± 0.05 in data I and 0.27 ± 0.05 in data II) from a MC simulated sample of atmospheric neutrino events for a live time of 100 years. This background evaluation also takes into account of the effect of oscillation, the efficiency of neutron tagging and the efficiency of both the spallation and solar cuts. Fig. 9.5 shows the positron/electron energy spectrum.

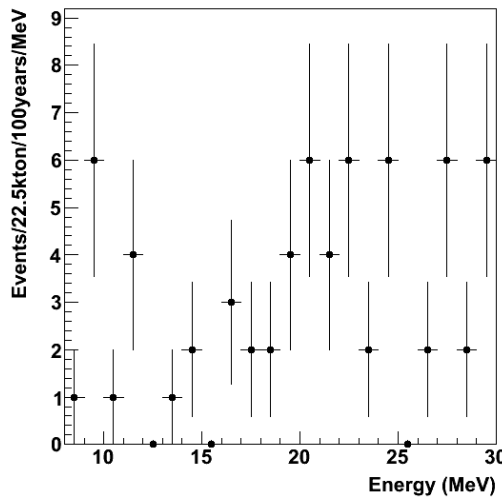


Figure 9.4 The positron/electron energy spectrum for the MC simulated atmospheric $\bar{\nu}_e$ CC events. The sample corresponds to a live time of 100 year.

9.2.3 Neutral Current (NC) Events

The detailed information of NC background can be found in Ref^[48]. The dominant NC process is the NC elastic scattering: $\nu + n \rightarrow \nu + n$. The outgoing neutron can produce primary gamma rays and secondary neutrons from the interactions with water, in which the primary events have an isotropic light feature. Most of the NC events are removed by the Cherenkov angle cut. Since SK cannot distinguish between gammas and positrons/electrons, the survival NC events become the background. Fig. 9.5 shows the energy spectrum for the NC background, which shows a trend of enhancement in the low energy region according the model^[48]. The estimated NC background is (0.6 ± 0.6)

(0.2 ± 0.2 in data I and 0.4 ± 0.4 in data II). The NC component is quite complicated in low energy region of interest, we assign a 100% uncertainty to this background estimation.

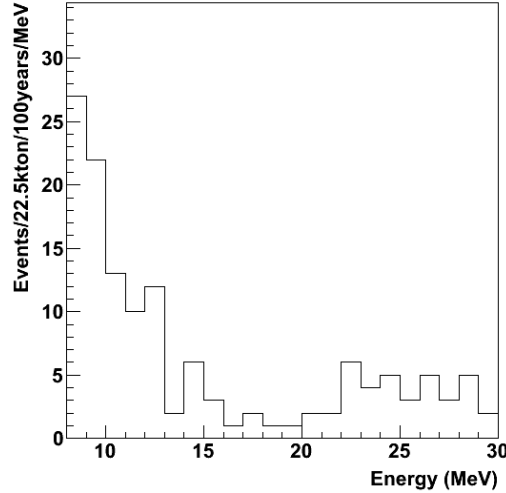


Figure 9.5 The positron/electron energy spectrum for the MC simulated atmospheric NC events. The sample corresponds to a live time of 100 year.

9.2.4 Reactor Neutrinos

The neutrinos from reactors are $\bar{\nu}_e$'s and cannot be distinguished from the SRN $\bar{\nu}_e$ either. Although the nuclear power plants in Japan were shut down after the Fukushima accident in 2011, there are still some reactor neutrino background from South Korea. The energy of reactor neutrinos is known to be below 10 MeV, however, the reactor events can still sneak into the energy region beyond 10 MeV through the resolution effect. According to the daily measured reactor neutrino flux by KamLAND in Kamioka site, we estimate (1.1 ± 0.2) (0.10 ± 0.02 in data I and 1.0 ± 0.2 in data II) events for the reactor neutrinos background.

9.2.5 ${}^9\text{Li}$ Events

Most of the spallation induced ${}^9\text{Li}$ events are removed by the spallation cuts. The distributions of the four discriminating variables to calculate the spallation likelihood (see Sec 8.2) are given by a toy MC for the ${}^9\text{Li}$ events and the random events. Fig. 9.6 and Fig. 9.7 show the distributions of four discriminating variables for the simulated ${}^9\text{Li}$ sample and the random data sample, separately. Fig. 9.8 shows the distributions of the spallation likelihoods for both the random sample and the ${}^9\text{Li}$ samples. With the present

cuts, the remaining ${}^9\text{Li}$ events in the final sample is estimated to be (1.6 ± 0.4) (0.12 ± 0.02 in data I and 1.48 ± 0.35 in data II) from the MC simulation.

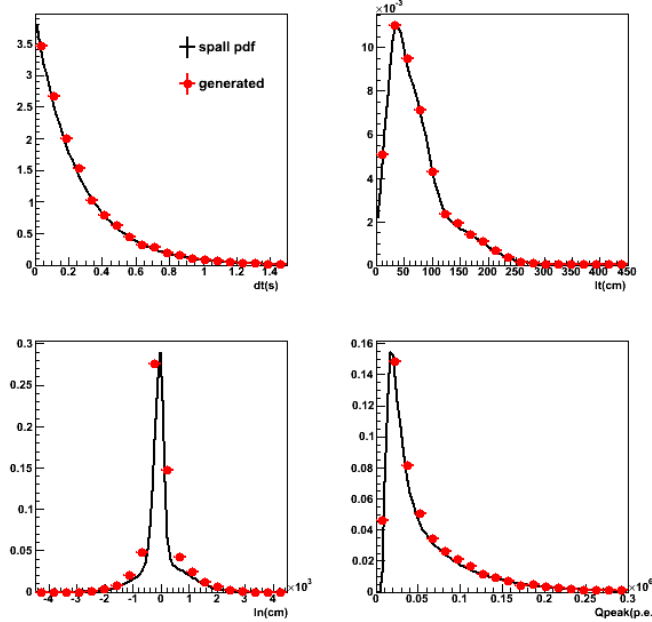


Figure 9.6 The distributions of four discriminating variables for the ${}^9\text{Li}$ events.

9.2.6 Accidental Background

The number of expected accidental background events is estimated to be (12.2 ± 2.8) (2.5 ± 0.6 in data I and 9.7 ± 2.2 in data II), which is model-independent and directly from the random trigger data during the data collection period. The accidental background consists of two parts: one is from the remaining solar neutrinos, the other one is from the spallation induced radioactive isotopes. To estimate the number of remaining solar neutrinos, the $\cos \theta_{sun}$ distribution is used. The number of events with the $\cos \theta_{sun}$ in $-1\sim 0$ is assumed to be the background for solar neutrinos. The number of solar events is obtained using the number of events with a $\cos \theta_{sun}$ in $0\sim 0.9$ subtracting the scaled background for the solar neutrinos. The remaining number of solar neutrino events is ~ 1.4 out of the total 12.2 accidental background events with an efficiency correction for the neutron tagging. The evaluation of the remaining number of spallation induced radioactive isotopes is performed in the similar fashion as that for the ${}^9\text{Li}$ background estimation. The radioactive isotopes ${}^{12}\text{B}$ and ${}^{12}\text{N}$ are all removed by the spallation cuts due to the short life time. The remaining radioactive isotopes are ${}^{16}\text{N}$, ${}^8\text{Li}/{}^8\text{B}$.

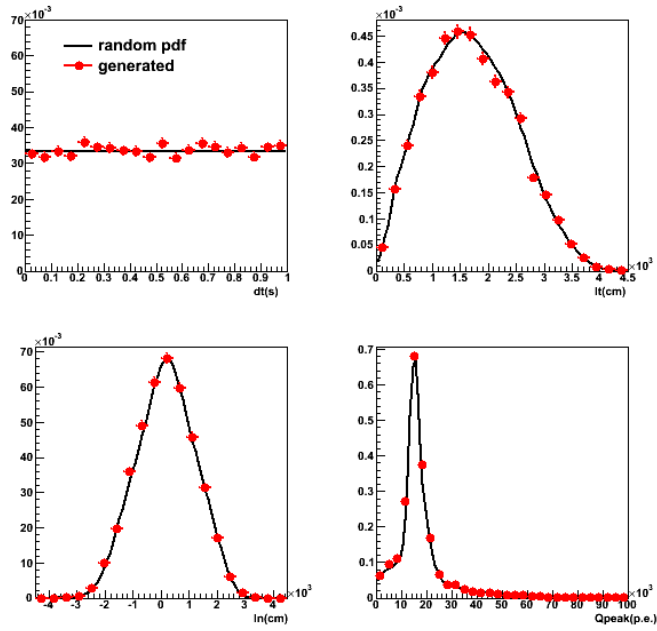


Figure 9.7 The distributions of four discriminating variables for the random events.

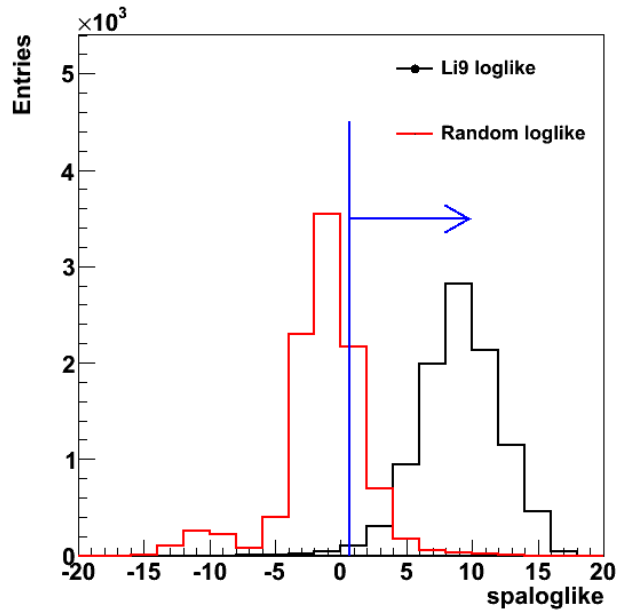


Figure 9.8 The spallation likelihoods for the random events and the ⁹Li sample, respectively. The SRN signal is required to be lower than 0.7 (1.4) below 11 (12) MeV.

The summaries of the expected number of background are listed in Table 9.2, Table 9.3 and Table 9.4, respectively.

Table 9.2 Summary of the expected numbers for all kinds of the background in the observed SRN sample for data I.

Background	Expected number of events
Atmospheric $\bar{\nu}_\mu/\nu_\mu$	0.9 ± 0.2
Atmospheric $\bar{\nu}_e$	0.23 ± 0.05
NC	0.2 ± 0.2
Reactor neutrinos	0.10 ± 0.02
${}^9\text{Li}$	0.12 ± 0.02
Accidental background	2.5 ± 0.6
Total	4.1 ± 0.7

Table 9.3 Summary of the expected numbers for all kinds of the background in the observed SRN sample for data II.

Background	Expected number of events
Atmospheric $\bar{\nu}_\mu/\nu_\mu$	1.1 ± 0.2
Atmospheric $\bar{\nu}_e$	0.27 ± 0.05
NC	0.4 ± 0.4
Reactor neutrinos	1.0 ± 0.2
${}^9\text{Li}$	1.48 ± 0.35
Accidental background	9.7 ± 2.2
Total	13.9 ± 2.3

9.3 Systematics on Both the Efficiencies and the Background Estimations

The systematic uncertainty on the efficiencies includes the effects from both the e^+ selection and neutron tagging. The systematic uncertainty of e^+ selection efficiency^[36] consists of the IBD cross section (1.0%) and the data reduction (3.1%). A 10% of systematic uncertainty is assigned to the neutron tagging efficiency (see Sec. 6.4).

Table 9.4 Summary of the expected numbers for all kinds of the background in the observed SRN sample (data I + data II).

Background	Expected number of events
Atmospheric $\bar{\nu}_\mu/\nu_\mu$	2.0 ± 0.4
Atmospheric $\bar{\nu}_e$	0.5 ± 0.1
NC	0.6 ± 0.6
Reactor neutrinos	1.1 ± 0.2
${}^9\text{Li}$	1.6 ± 0.4
Accidental background	12.2 ± 2.8
Total	18.0 ± 3.0

The total systematic uncertainty on the signal efficiency is 10.5%, which is added in quadrature.

The flux on the atmospheric neutrinos has a 10.0% uncertainty in the model used by the MC simulation^[72]. To be conservative, the estimation on atmospheric neutrinos events is assigned to have a 20% systematic uncertainty. The NC is very complicated and a 100% systematic uncertainty is assigned. The systematic uncertainty on the reactor neutrinos is estimated to be 20%. The systematic uncertainty on the ${}^9\text{Li}$ events is estimated to be 23.4% (see Sec 7.2). The systematic uncertainty on the accidental background is estimated to be 23.0% (see Sec 6.1).

9.4 Limit Extraction

9.4.1 The Upper Limit of the Differential Flux

Since the number of the observed 18 events agrees with the expected (18.0 ± 3.0) background events, no obvious signal is seen from this measurement. The estimation of accidental background events, ${}^9\text{Li}$ events and reactor neutrino events are rather robust since they are directly evaluated from the data. Although the estimated atmospheric neutrino events are obtained from the MC simulation, they are not the dominant background. Upper limits on the $\bar{\nu}_e$ flux in 9.3-31.3 MeV are calculated at 90% C.L. for each MeV bin using Poisson method^[73], Feldman-Cousins (FC) method^[74] and Rolke method^[75], respectively. In Poisson method, the upper limit is calculated by the following

formula:

$$N^{90} = N^{90}(\text{no background}) - N_b \quad (9-1)$$

where N^{90} and $N^{90}(\text{no background})$ are the numbers with and without background at 90% C.L. respectively, N_b is the expected number of background events. In FC method, an ordering principle is used to determine the confidence interval with the correct coverage. However, the systematic uncertainty on both the efficiency and the background estimation cannot be included in FC method. Rolk method computes the confidence intervals using the known profile likelihood method, which can include the additional background parameters with the uncertainties. Both FC method and Rolk method are available in ROOT^[63]. The upper limit of $\bar{\nu}_e$ flux is calculated by the following formula:

$$\phi_{90} = \frac{N_{90}}{T \cdot N_p \cdot \bar{\sigma} \cdot \epsilon} \text{ cm}^{-2}\text{s}^{-1}, \quad (9-2)$$

where ϕ_{90} is the upper limit of $\bar{\nu}_e$ flux, T is the live time, $N_p = 1.5 \times 10^{33}$ is the number of free protons, $\bar{\sigma}$ is the IBD cross section at the center of energy bin and ϵ is the IBD detection efficiency. Notice that $E_{\bar{\nu}_e} = E_{e^+} + 1.3 \text{ MeV}$. Also notice that in 8-10 MeV, the live time of data set is 998 days while above 10 MeV, the live time of the data set is 1890 days. Table 9.5 lists the ϕ_{90} values calculated by Poisson method, FC method and Rolk method, respectively. The limits are also plotted in Fig. 9.9. All the limits are found to be consistent within $\sim 30\%$. The ϕ_{90} calculated by Poisson method is lower than that of FC method since Poisson method generates the upper limits with the direct subtraction of the expected background events while FC method has the positive limitation to the true value of the interested parameter. The ϕ_{90} calculated by Rolk method is lower than that of FC method due to the effect of multi-dimensional parameters.

The limits calculated by Rolk method are used in this study in order to take into account of the systematic uncertainties on both the efficiency and the background estimation. Fig. 9.10 shows the upper limits of $\bar{\nu}_e$ flux in 9.3-31.3 MeV using Rolk method as well as KamLAND results^[35], SK-IV previous results^[13] and SK-I/II/III results^[36], respectively. The expected SRN spectrum using the constant SN rate model is also plotted for the purpose of comparison.

Compared with the previous SK-IV results, the upper limits of $\bar{\nu}_e$ flux above 14.3 MeV is more sensitive than the previous SK-IV results due to the increased (~ 2 times) live time. The previous SK-IV results cannot get down to the energy region below 13.3

Table 9.5 The ϕ_{90} values calculated by Poisson method, FC method and Rolk method, respectively. The unit is $\text{cm}^{-2}\text{s}^{-1}$. $E_{\bar{\nu}_e} = E_{e^+} + 1.3 \text{ MeV}$.

Energy range	Poisson method	FC method	Rolk method
9.3-10.3	133.0	162.0	171.9
10.3-11.3	64.2	88.0	85.1
11.3-12.3	91.7	109.4	101.4
12.3-13.3	100.1	114.5	107.7
13.3-14.3	88.4	99.6	92.6
14.3-15.3	13.9	17.1	10.6
15.3-16.3	31.3	35.7	29.4
16.3-17.3	19.3	20.6	16.4
17.3-18.3	19.0	20.2	16.2
18.3-19.3	19.0	20.2	16.3
19.3-20.3	29.9	33.6	28.1
20.3-21.3	16.3	17.4	14.0
21.3-22.3	16.8	17.9	14.4
22.3-23.3	16.5	17.6	14.1
23.3-24.3	15.6	16.6	13.3
24.3-25.3	15.9	16.9	13.5
25.3-26.3	13.5	14.4	11.4
26.3-27.3	14.5	15.5	12.4
27.3-28.3	24.1	27.2	22.6
28.3-29.3	23.5	26.5	22.0
29.3-30.3	13.4	14.3	11.4
30.3-31.3	13.6	14.5	11.6

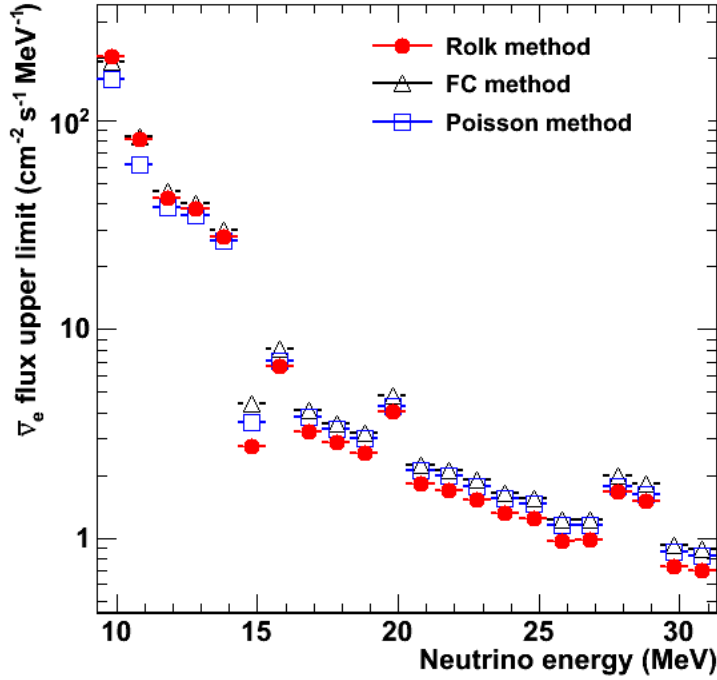


Figure 9.9 The ϕ_{90} values calculated by Poisson method, FC method and Rolk method.

MeV due to the limitation of spallation background. With the improved background suppression, the neutrino energy threshold is first lowered to 9.3 MeV at SK, covering the entire golden energy window of 10-30 MeV for the SRN search.

The upper limits of $\bar{\nu}_e$ flux are more sensitive than the KamLAND results above 13.3 MeV while the limits are weaker below 13.3 MeV. KamLAND estimated the dominate NC events from a spectral fit instead of estimation from data (see Sec 1.5). The worse limit of the KamLAND result is due to the unknown event excess.

The upper limits of $\bar{\nu}_e$ flux given by SK-I/II/III are still the most sensitive ones above 17.3 MeV due to the long live time and the higher efficiency in the detection of prompt e^+ . Since the SK-I/II/III search for the SRN only studied the prompt e^+ signal, the search could not be done for the real IBD events and also could not get down to the energy region below 17.3 MeV due to the huge spallation background.

Finally, the measurements are compared with the constant SN rate model which has the largest flux among all the SRN models.

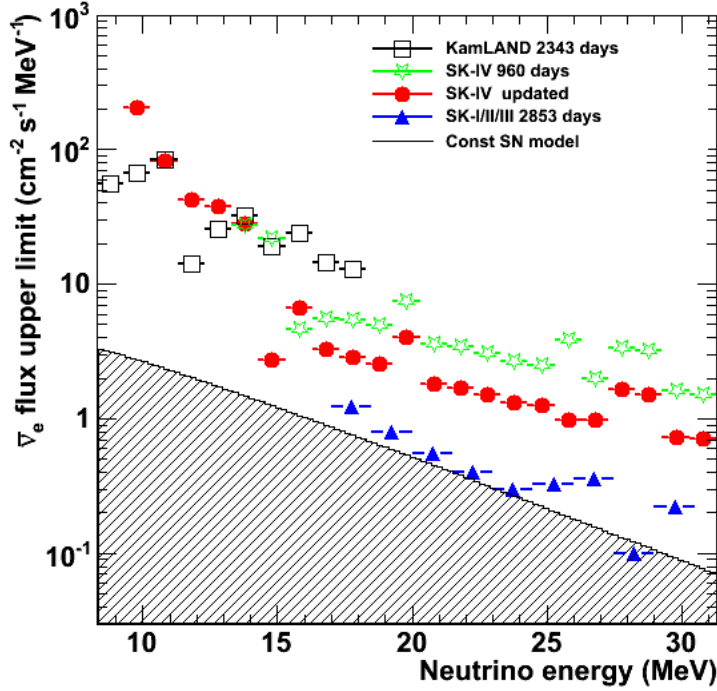


Figure 9.10 The 90% C.L. upper limits on $\bar{\nu}_e$ flux from SK-IV (red line with solid point) in 9.3-31.3 MeV. The limits from SK-I/II/III (blue line with solid triangle) above 17.3 MeV, the previous SK-IV results (green line with open star) in 13.3-31.3 MeV and the KamLAND results (black line with open rectangle) in 8.3-18.3 MeV are also shown for comparisons. The shaded area represents the predicted spectrum of SRN using the constant SN rate model.

9.4.2 The Upper Limit for the Integral Flux

Using Rolk method, the upper limit of integral number at 90% C.L. is $N_{90}=100.4$ (85.5, i.e. 34.9 events/22.5kton/year for data I and 50.6, i.e. 18.5 events/22.5kton/year for data II) events by using the number of observed 18 (7 for data I and 11 for data II) events and the number of expected (18.0 ± 3.0) (4.1 ± 0.7 for data I and 13.9 ± 2.3 for data II) background events. The upper limit of 90% C.L. integral flux F_{90} can be calculated by the following formula:

$$\frac{F_{90}}{N_{90}} = \frac{F_M}{N_P} \quad (9-3)$$

where N_P is the predicted number of the SRN events and F_M is the predicted flux at a certain energy threshold for each model. N_{P1} is the predicted number of SRN events in 22.5 kton-year with a neutrino energy range of 11.3~31.3 MeV, N_{P2} is the predicted number of SRN events in 22.5 kton-year with a neutrino energy range of 9.3~31.3 MeV. N_{PT} is the total predicted number of SRN events, which is calculated by the following

formula:

$$N_{PT} = N_{P1} \times T1 + N_{P2} \times T2 \quad (9-4)$$

where $T1$ is the live time of data I in the unit of year and $T2$ is the live time of data II in the unit of year. Table 9.6, Table 9.7 and Table 9.8 list the results for data I, data II and the combined data, respectively. Fig. 9.11 shows the N_{P1} for each SRN model as well as the

Table 9.6 The flux for each SRN model in neutrino energy of 11.3-31.3 MeV (F_{M1}), the predicted number of the SRN events in 22.5 kton·year with a neutrino energy range of 11.3~31.3 MeV (N_{P1}), upper limit of $\bar{\nu}_e$ flux at 90% C.L. (F_{90}) ($\text{cm}^{-2} \text{s}^{-1}$) in 11.3-31.3 MeV. The upper limit of integral number at 90% C.L. is $N_{90}=34.9$ events/22.5kton/year 11.3-31.3 MeV for data I.

SRN model	F_{M1}	N_{P1}	F_{90} in 11.3-31.3 MeV
LMA ^[26]	5.7	5.2	38.3
Constant SN rate ^[21]	12.7	12.6	35.2
Cosmic gas ^[23]	1.0	0.9	38.8
Chemical evolution ^[24]	2.0	1.9	36.7
Heavy metal ^[20,25]	6.3	5.7	38.6
Population synthesis ^[22]	1.7	1.6	37.1
HBD 6 MeV ^[27]	5.3	5.3	34.9
Star formation rate ^[28]	2.6	2.3	39.5
Failed SN ^[29]	2.2	2.1	36.6

N_{90} for data I. Fig. 9.12 shows the N_{P2} for each SRN model as well as the N_{90} for data II. Fig. 9.13 shows the N_{PT} for each SRN model as well as the N_{90} for all data. None of the SRN models can be excluded by this study. In order to test the SRN models, for example, the constant SN rate model, we need to improve at least a factor of 2 signal-to-noise ratio.

Table 9.7 The flux for each SRN model in neutrino energy of 9.3-31.3 MeV (F_{M2}), the predicted number of the SRN events in 22.5 kton-year with a neutrino energy range of 9.3~31.3 MeV (N_{P2}), upper limit of $\bar{\nu}_e$ flux at 90% C.L. (F_{90}) ($\text{cm}^{-2} \text{s}^{-1}$) in 9.3-31.3 MeV. The upper limit of integral number at 90% C.L. is $N_{90}=18.5$ events/22.5kton/year 9.3-31.3 MeV for data II.

SRN model	F_{M2}	N_{P2}	F_{90} in 9.3-31.3 MeV
LMA ^[26]	8.3	6.1	25.2
Constant SN rate ^[21]	17.8	14.3	23.0
Cosmic gas ^[23]	1.5	1.0	27.8
Chemical evolution ^[24]	2.9	2.2	24.4
Heavy metal ^[20,25]	9.3	6.8	25.3
Population synthesis ^[22]	2.6	1.9	25.3
HBD 6 MeV ^[27]	7.6	6.0	23.4
Star formation rate ^[28]	4.0	2.7	27.4
Failed SN ^[29]	3.3	2.5	24.4

Table 9.8 The flux for each SRN model in neutrino energy of 9.3-31.3 MeV (F_{M2}), the total predicted number of the SRN events (N_{PT}), the total predicted number of the SRN events after efficiency correction (T_{PT}) and the combined upper limit of $\bar{\nu}_e$ flux at 90% C.L. (F_{90}) ($\text{cm}^{-2} \text{s}^{-1}$) in 9.3-31.3 MeV. The upper limit of integral number at 90% C.L. is $N_{90}=100.4$ events for combined data.

SRN model	F_{M2}	N_{PT}	T_{PT}	F_{90} in 9.3-31.3 MeV
LMA ^[26]	8.3	29.4	2.7	28.3
Constant SN rate ^[21]	17.8	70.1	6.5	25.5
Cosmic gas ^[23]	1.5	4.9	0.5	30.7
Chemical evolution ^[24]	2.9	10.5	1.0	27.7
Heavy metal ^[20,25]	9.3	32.6	3.0	28.6
Population synthesis ^[22]	2.6	9.1	0.8	28.7
HBD 6 MeV ^[27]	7.6	29.3	2.7	26.0
Star formation rate ^[28]	4.0	13.0	1.2	30.9
Failed SN ^[29]	3.3	11.9	1.1	27.8

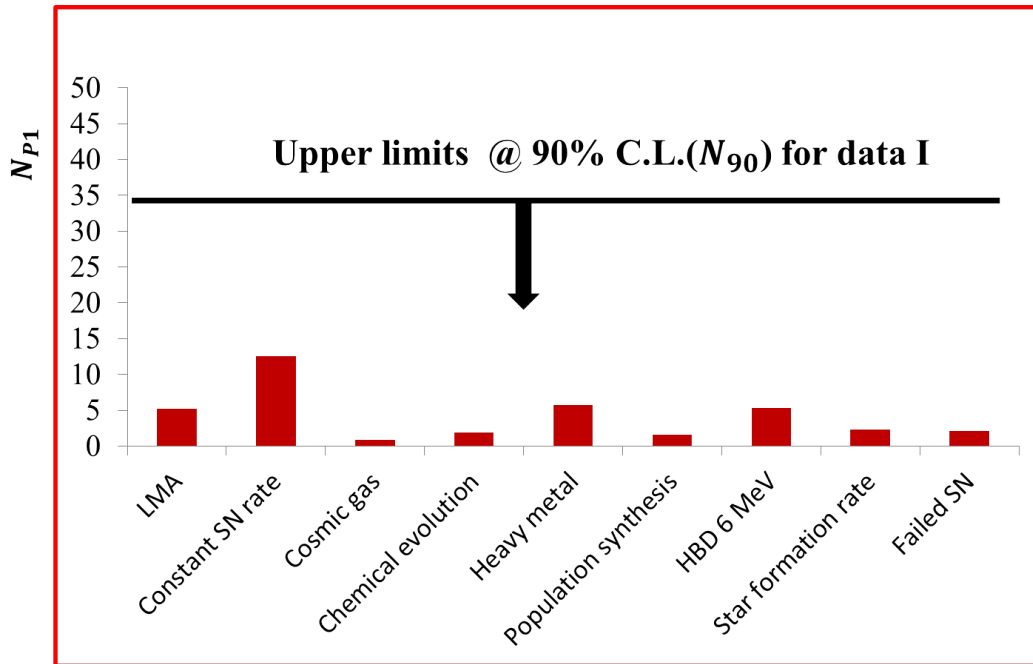


Figure 9.11 The N_{p1} events/22.5kton/year for each SRN model as well as the N_{90} observed events for data I.

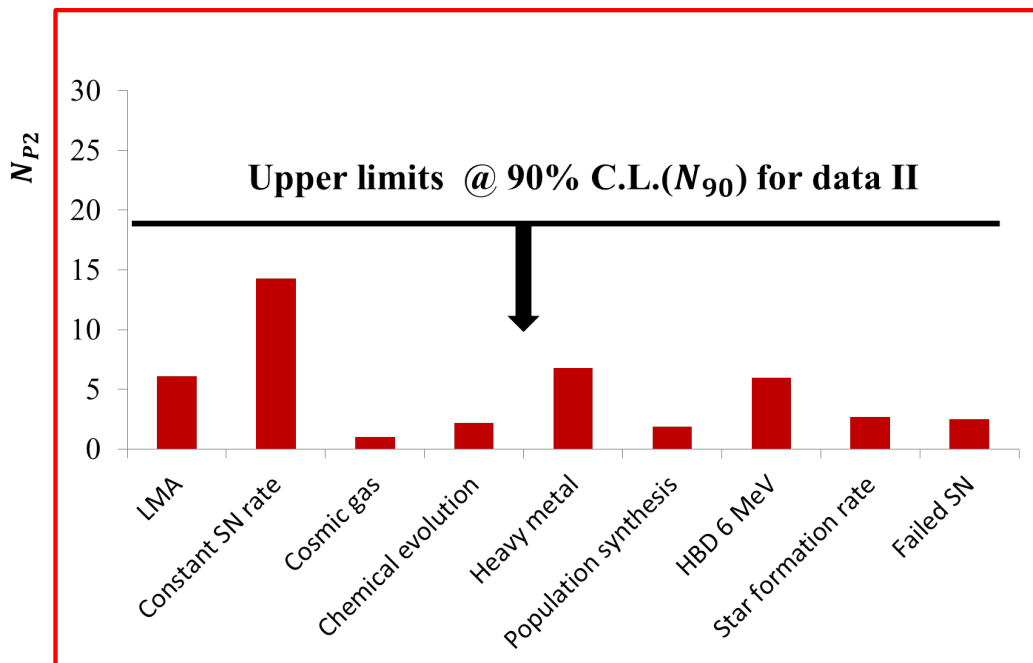


Figure 9.12 The N_{p2} events/22.5kton/year for each SRN model as well as the N_{90} observed events for data II.

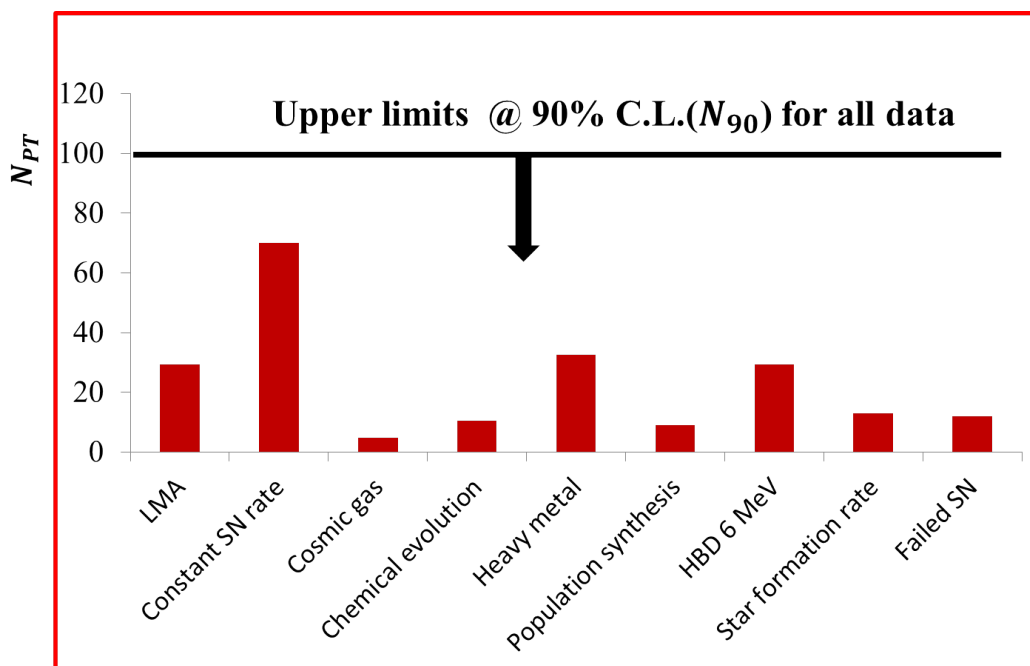


Figure 9.13 The N_{PT} events for each SRN model as well as the N_{90} observed events for combined data.

Chapter 10 Summary and Outlook

10.1 Summary

The detection of SRN is of crucial importance for studying the evolution of the universe, the formation of stars, the mechanism of supernova bursts and the related neutrino physics. However, SRN have never been observed yet. In the so-called golden neutrino energy window of 10-30 MeV for the SRN search at SK, the dominant background is the cosmic-ray muon spallation induced radioactive isotopes. To remove this background, we better tune the spallation cuts around 8 MeV electron energy according to optimization of the signal-to-noise ratio. Furthermore, we enhance the neutron tagging method with the efficiency of $(10.3 \pm 1.0)\%$ and the accidental background level of $(0.065 \pm 0.015)\%/500 \mu\text{s}$. This neutron tagging has been applied to the SRN search for $E_{\bar{\nu}_e} < 14.3$ MeV where there are huge spallation background. While for $E_{\bar{\nu}_e} > 14.3$ MeV, the neutron tagging efficiency of $(18.1 \pm 0.4)\%$ with the accidental background level of $(0.32 \pm 0.03)\%/500 \mu\text{s}$ is applied due to the less spallation background in this energy region. Compared with the previous neutron tagging ($\sim 20\%$ efficiency with the $\sim 1\%/500 \mu\text{s}$ accidental background level), the signal-to-noise ratio of the improved one is increased by a factor of ~ 2 .

The yields of the major radioactive isotopes induced by cosmic-ray muon spallation are first measured on distribution of time after a muon using the low energy data above 6.5 MeV. The results are listed in Table 7.5. The results from theoretical prediction^[34] are also listed in Table 7.5 for comparison. Furthermore, we improve the measurement on ${}^9\text{Li}$ yield to be $(0.56 \pm 0.07 \pm 0.13) \mu^{-1} \text{g}^{-1} \text{cm}^2$ by tagging delayed neutrons using 500 μs forced trigger data (See Table 7.5). The measurement is of crucial importance for the present and future low-energy astrophysical neutrino experiments using the water Cherenkov technique, such as SK, the future GADZOOKS! and Hyper-Kamiokande projects. The measurement could also help to improve simulations based on FLUKA and GEANT4.

By using the improved neutron tagging method, we search for the SRN in the neutrino energy between 9.3 and 31.3 MeV at SK. This is the first time we cover the whole golden energy window for the SRN search. The number of 18 observed candidates

is consistent with that of (18.0 ± 3.0) expected background events. No signal is found. Therefore, the upper limits of differential flux are calculated, together with those on the integral fluxes which are summarized in Table 9.8. All the integral fluxes are in the range of $25\text{-}31 \text{ cm}^{-2}\text{s}^{-1}$ at 90% C.L.. These limits are approaching to the flux predicted by the constant supernova rate model, however, they are still an order of magnitude larger than those for the other models.

10.2 Outlook

In future, increasing statistics and having a better signal-to-noise ratio of neutron tagging are expected to improve the upper limit of flux to the level that can test the constant SN rate model and even other models.

The spallation background in this analysis can still be suppressed if the neutron tagging can use the vertex information for both the prompt positron and the delayed neutron as already demonstrated in Ref.^[66]. This needs to reconstruct the vertex of 2.2 MeV γ which only fires 8 PMTs on average. A dedicated software is needed for this purpose.

On the other hand, SRN physics could be significantly enhanced if neutron tagging can be applied in a more efficient way in GADZOOKS!^[33]. By adding a 0.2% gadolinium solution into water, the neutron tagging efficiency could be increased up to 66.7% (could be even higher) for a background level down to 2×10^{-4} ^[64]. This is very tantalizing for future SRN searches. However, there are still some technical issues that need to be solved. Now the addition of gadolinium into water is being tested in a prototype to decide whether to go or not on the experiment. Future fulfillment of SRN discovery is expected in GADZOOKS!.

Reference

- [1] W.Pauli Letter sent to the Tubingen conference (December, 1930).
- [2] F. Reines and C. Cowan, *Free anti-neutrino absorption cross-section. I: Measurement of the free anti-neutrino absorption cross-section by protons*, Phys. Rev. 113 (1959) 273.
- [3] J.H..Bahcall, *Neutrino astrophysics*, Cambridge University Press (1989).
- [4] C.Giunti and C. Kim, *Fundamentals of neutrino physics and astrophysics*, Oxford University Press (2007).
- [5] T.Padmanabha, *Theoretical astrophysics, volume ii: Stars and stellar systems*, Cambridge University Press (2001).
- [6] K. Kotake, K. Sato, and K. Takahashi, *Explosion mechanism, neutrino burst, and gravitational wave in core-collapse supernovae*, Rept. Prog. Phys. 69 (2006) 971, arXiv:astro-ph/0509456.
- [7] T. Totani, K. Sato, H. Dalhed, and J. Wilson, *Future detection of supernova neutrino burst and explosion mechanism*, Astrophys. J. 496 (1998) 216, arXiv:astro-ph/9710203.
- [8] K. Takahashi, M. Watanabe, K. Sato, and T. Totani, *Effects of neutrino oscillation on the supernova neutrino spectrum*, Phys. Rev. D64 (2001) 093004, arXiv:hep-ph/0105204.
- [9] Kamiokande-II, K. Hirata *et al.*, *Observation of a Neutrino Burst from the Supernova SN 1987a*, Phys. Rev. Lett. 58 (1987) 1490.
- [10] R. Bionta *et al.*, *Observation of a Neutrino Burst in Coincidence with Supernova SN 1987a in the Large Magellanic Cloud*, Phys. Rev. Lett. 58 (1987) 1494.
- [11] G. Tammann, W. Loeffler, and A. Schroder, *The Galactic supernova rate*, Astrophys. J. Suppl. 92 (1994) 487.
- [12] R. Diehl *et al.*, *Radioactive Al-26 and massive stars in the galaxy*, Nature439 (2006) 45, arXiv:astro-ph/0601015.
- [13] Super-Kamiokande, H. Zhang *et al.*, *Supernova Relic Neutrino Search with Neutron Tagging at Super-Kamiokande-IV*, Astropart. Phys. 60 (2014) 41, arXiv:1311.3738.
- [14] K. Abe *et al.*, *Letter of Intent: The Hyper-Kamiokande Experiment — Detector Design and Physics Potential* —, arXiv:1109.3262.
- [15] A. de Bellefon *et al.*, *MEMPHYS: A Large scale water Cerenkov detector at Frejus*, arXiv:hep-ex/0607026.
- [16] C. K. Jung, *Feasibility of a next generation underground water Cherenkov detector: UNO*, AIP Conf. Proc. 533 (2000) 29, arXiv:hep-ex/0005046.
- [17] W. Zhang *et al.*, *Experimental Limit on the Flux of Relic Anti-neutrinos From Past Supernovae*, Phys. Rev. Lett. 61 (1988) 385.
- [18] J. F. Beacom, *The Diffuse Supernova Neutrino Background*, Ann. Rev. Nucl. Part. Sci. 60 (2010) 439, arXiv:1004.3311.

Reference

- [19] S. Ando and K. Sato, *Relic neutrino background from cosmological supernovae*, New J. Phys. 6 (2004) 170, arXiv:astro-ph/0410061.
- [20] M. Kaplinghat, G. Steigman, and T. Walker, *The Supernova relic neutrino background*, Phys. Rev. D62 (2000) 043001, arXiv:astro-ph/9912391.
- [21] T. Totani and K. Sato, *Spectrum of the relic neutrino background from past supernovae and cosmological models*, Astropart. Phys. 3 (1995) 367, arXiv:astro-ph/9504015.
- [22] T. Totani, K. Sato, and Y. Yoshii, *Spectrum of the supernova relic neutrino background and evolution of galaxies*, Astrophys. J. 460 (1996) 303, arXiv:astro-ph/9509130.
- [23] R. Malaney, *Evolution of the cosmic gas and the relic supernova neutrino background*, Astropart. Phys. 7 (1997) 125, arXiv:astro-ph/9612012.
- [24] D. Hartmann and S. Woosley, *The cosmic supernova neutrino background*, Astropart. Phys. 7 (1997) 137.
- [25] L. E. Strigari, M. Kaplinghat, G. Steigman, and T. P. Walker, *The Supernova relic neutrino backgrounds at KamLAND and Super-Kamiokande*, JCAP0403 (2004) 007, arXiv:astro-ph/0312346.
- [26] S. Ando, K. Sato, and T. Totani, *Detectability of the supernova relic neutrinos and neutrino oscillation*, Astropart. Phys. 18 (2003) 307, arXiv:astro-ph/0202450.
- [27] S. Horiuchi, J. F. Beacom, and E. Dwek, *The Diffuse Supernova Neutrino Background is detectable in Super-Kamiokande*, Phys. Rev. D79 (2009) 083013, arXiv:0812.3157.
- [28] M. Fukugita and M. Kawasaki, *Constraints on the star formation rate from supernova relic neutrino observations*, Mon. Not. Roy. Astron. Soc. 340 (2003) L7, arXiv:astro-ph/0204376.
- [29] C. Lunardini, *Diffuse neutrino flux from failed supernovae*, Phys. Rev. Lett. 102 (2009) 231101, arXiv:0901.0568.
- [30] K. Nakazato, E. Mochida, Y. Niino, and H. Suzuki, *Spectrum of the Supernova Relic Neutrino Background and Metallicity Evolution of Galaxies*, arXiv:1503.0123.
- [31] Super-Kamiokande, M. Malek *et al.*, *Search for supernova relic neutrinos at SUPER-KAMIOKANDE*, Phys. Rev. Lett. 90 (2003) 061101, arXiv:hep-ex/0209028.
- [32] G. Fogli, E. Lisi, A. Mirizzi, and D. Montanino, *Probing supernova shock waves and neutrino flavor transitions in next-generation water-Cherenkov detectors*, JCAP0504 (2005) 002, arXiv:hep-ph/0412046.
- [33] J. F. Beacom and M. R. Vagins, *GADZOOKS! Anti-neutrino spectroscopy with large water Cherenkov detectors*, Phys. Rev. Lett. 93 (2004) 171101, arXiv:hep-ph/0309300.
- [34] S. W. Li and J. F. Beacom, *First calculation of cosmic-ray muon spallation backgrounds for MeV astrophysical neutrino signals in Super-Kamiokande*, Phys. Rev. C89 (2014) 045801, arXiv:1402.4687.
- [35] KamLAND, A. Gando *et al.*, *A study of extraterrestrial antineutrino sources with the KamLAND detector*, Astrophys. J. 745 (2012) 193, arXiv:1105.3516.
- [36] Super-Kamiokande, K. Bays *et al.*, *Supernova Relic Neutrino Search at Super-Kamiokande*, Phys. Rev. D85 (2012) 052007, arXiv:1111.5031.

Reference

- [37] Super-Kamiokande, Y. Fukuda *et al.*, *The Super-Kamiokande detector*, Nucl. Instrum. Meth. A501 (2003) 418.
- [38] A. Suzuki *et al.*, *Improvement of 20-inch diameter photomultiplier tubes*, Nucl. Instrum. Meth. A329 (1993) 299.
- [39] *ATM-3 (ATLAS Muon TDC Version 3) User's Manual*, .
- [40] H. Nishino *et al.*, *High-speed charge-to-time converter ASIC for the Super-Kamiokande detector*, Nucl. Instrum. Meth. A610 (2009) 710, [arXiv:0911.0986](https://arxiv.org/abs/0911.0986).
- [41] Super-Kamiokande, S. Yamada *et al.*, *Commissioning of the new electronics and online system for the Super-Kamiokande experiment*, IEEE Trans. Nucl. Sci. 57 (2010) 428.
- [42] K. Abe *et al.*, *Calibration of the Super-Kamiokande Detector*, Nucl. Instrum. Meth. A737 (2014) 253, [arXiv:1307.0162](https://arxiv.org/abs/1307.0162).
- [43] Super-Kamiokande, M. Nakahata *et al.*, *Calibration of Super-Kamiokande using an electron linac*, Nucl. Instrum. Meth. A421 (1999) 113, [arXiv:hep-ex/9807027](https://arxiv.org/abs/hep-ex/9807027).
- [44] Super-Kamiokande, E. Blaufuss *et al.*, *N-16 as a calibration source for Super-Kamiokande*, Nucl. Instrum. Meth. A458 (2001) 638, [arXiv:hep-ex/0005014](https://arxiv.org/abs/hep-ex/0005014).
- [45] M.Smy, *Low Energy Event Reconstruction and Selection in Super-Kamiokande-III*, Proceedings of the 30th ICRC5 (2007) 1279.
- [46] Z.Conner, *A study of solar neutrinos using the super-kamiokande detector*, PhD thesis, University of Maryland (1997).
- [47] S.Desai, *High energy neutrino astrophysics with super-kamiokande*, PhD thesis, Boston University (2004).
- [48] K.Bays, *Search for the diffuse supernova neutrino background at super-kamiokande*, PhD thesis, University of California, Irvin (2011).
- [49] M.Malek, *A search for supernova relic neutrinos*, PhD thesis, State University of New York at Stony Brook (2003).
- [50] M.Ikeda, *Precise measurement of solar neutrinos with super-kamiokande iii*, PhD thesis, University of Tokyo (2009).
- [51] Y. Hayato, *NEUT*, Nucl. Phys. Proc. Suppl. 112 (2002) 171.
- [52] H.Nishino, *Search for nucleon decay into charged antilepton plus meson in super-kamiokand*, PhD thesis, University of Tokyo (2009).
- [53] G.Mitsuka, *Study of non-standard neutrino interactions with atmospheric neutrinos data in super-kamiokand*, PhD thesis, University of Tokyo (2009).
- [54] F. Ajzenberg-Selove, *Energy levels of light nuclei A = 11-12*, Nucl. Phys. A506 (1990) 1.
- [55] D. Tilley *et al.*, *Energy levels of light nuclei A=8,9,10*, Nucl. Phys. A745 (2004) 155.
- [56] <http://www.tunl.duke.edu/nucldata/GroundStatedecays/> (2015) .
- [57] <http://www.nndc.bnl.gov> (2015) .
- [58] A. Strumia and F. Vissani, *Precise quasielastic neutrino/nucleon cross-section*, Phys. Lett. B564 (2003) 42, [arXiv:astro-ph/0302055](https://arxiv.org/abs/astro-ph/0302055).

Reference

- [59] H. Zhang, *Study of low energy electron anti-neutrinos at super-kamiokande lv*, PhD thesis, Tsinghua University (2012).
- [60] S.-M. Chen and Z. Deng, *A proposal for detecting supernova relic neutrino in Super Kamiokande*, Nucl. Phys. Proc. Suppl. 166 (2007) 252.
- [61] Super-Kamiokande, K. Abe *et al.*, *Solar neutrino results in Super-Kamiokande-III*, Phys. Rev. D83 (2011) 052010, arXiv:1010.0118.
- [62] J. P. Speckmayer, A. Höcker and H. Voss, *The toolkit for multivariate data analysis, TMVA 4*, J. Phys. : Conf. Ser. 219 (2010) 032057.
- [63] <http://root.cern.ch> (2015) .
- [64] Super-Kamiokande, H. Watanabe *et al.*, *First Study of Neutron Tagging with a Water Cherenkov Detector*, Astropart. Phys. 31 (2009) 320, arXiv:0811.0735.
- [65] R. W. Stooksberry and M. F. Crouch, *Neutron-proton capture cross section*, Phys. Rev. 114 (1959) 1561.
- [66] Daya Bay, F. An *et al.*, *Independent measurement of the neutrino mixing angle θ_{13} via neutron capture on hydrogen at Daya Bay*, Phys. Rev. D90 (2014), no. 7 071101, arXiv:1406.6468.
- [67] KamLAND, S. Abe *et al.*, *Production of Radioactive Isotopes through Cosmic Muon Spallation in KamLAND*, Phys. Rev. C81 (2010) 025807, arXiv:0907.0066.
- [68] Borexino, G. Bellini *et al.*, *Cosmogenic Backgrounds in Borexino at 3800 m water-equivalent depth*, JCAP1308 (2013) 049, arXiv:1304.7381.
- [69] Super-Kamiokande, J. Hosaka *et al.*, *Solar neutrino measurements in super-Kamiokande-I*, Phys. Rev. D73 (2006) 112001, arXiv:hep-ex/0508053.
- [70] M. Shiozawa, *Search for proton decay via $p \rightarrow e^+ \pi^0$ in a large water cherenkov detector*, PhD thesis, University of Tokyo (1999).
- [71] Super-Kamiokande, Y. Ashie *et al.*, *A Measurement of atmospheric neutrino oscillation parameters by SUPER-KAMIOKANDE I*, Phys. Rev. D71 (2005) 112005, arXiv:hep-ex/0501064.
- [72] Y. Hayato98, *Search for proton decay into $k^+ \bar{\nu}$* , PhD thesis, Tokyo Institute of Technology (1998).
- [73] G. Cowan, *Statistical data analysis*, Clarendon Press Oxford (1998).
- [74] G. J. Feldman and R. D. Cousins, *A Unified approach to the classical statistical analysis of small signals*, Phys. Rev. D57 (1998) 3873, arXiv:physics/9711021.
- [75] W. A. Rolke, A. M. Lopez, and J. Conrad, *Limits and confidence intervals in the presence of nuisance parameters*, Nucl. Instrum. Meth. A551 (2005) 493, arXiv:physics/0403059.

Acknowledgement

First I would like to offer my gratitude to my supervisor, Professor Shaomin Chen. He led me to the exciting neutrino physics and introduced me to work at Super-Kamiokande. This is where all my graduate career begins. Professor Chen is always supportive and available in my scientific study. In addition, he is also a good friend in daily life. I think he is the best advisor one can imagine.

At Super-Kamiokande, I would like to thank Masayuki Nakahata-san, who gives a lot of discussions and comments on my study by taking time out of his busy schedule. I would like to thank Michael Smy, Yasuo Takeuchi-san, Mark Vagins for many discussions and comments. I am grateful to Yusuke Koshio-san, Yuuki Nakano-san, Lluís Martí Magro, Kai Martens, Motoyasu Ikeda-san, Makoto Miura-san, Yoshinari Hayato-san, Shunichi Mine-san, Stefanie Smith, Edward Kearns, Erin OSullivan, Yoichiro Suzuki-san, Takatomi Yano-san, Luis Labarga for many help.

In Tsinghua, I would like to thank Professor Gao Yuanning for many interesting talks. I would like to thank all the other colleagues for the care and help.

Finally, I would like to thank my family and my girlfriend. Without their continuous support, I can not finish the dissertation successfully.

声 明

本人郑重声明：所呈交的学位论文，是本人在导师指导下，独立进行研究工作所取得的成果。尽我所知，除文中已经注明引用的内容外，本学位论文的研究成果不包含任何他人享有著作权的内容。对本论文所涉及的研究工作做出贡献的其他个人和集体，均已在文中以明确方式标明。

签 名：_____ 日 期：_____

Resume and Publications

个人简历

1987年11月出生浙江省绍兴。

2006年9月考入西安交通大学理学院材料物理专业，2010年7月本科毕业并获得理学学士学位。

2010年9月考入清华大学工程物理系攻读物理学硕士学位。2012年9月，提前攻博进入清华大学工程物理系攻读物理学博士学位至今。

发表的学术论文

- [1] Yang Zhang, for the Super-Kamiokande Collaboration, Search for Supernova Relic Neutrinos with 2.2 MeV gamma tagging at Super-Kamiokande-IV, Physics Procedia 61 (2015) 384-391.
- [2] Super-Kamiokande Collaboration, Supernova Relic Neutrino Search with Neutron tagging at Super-Kamiokande-IV, Astroparticle Physics 60 (2015) 41 (SCI, AR1KS)